Accepted Manuscript

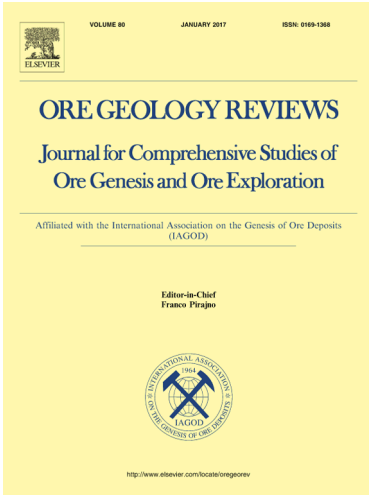

Geology, Mineralization, Stable Isotope, and Fluid Inclusion Characteristics of the Vostok-2 Reduced W-Cu Skarn and Au-W-Bi-As Stockwork Deposit, Sikhote-Alin, Russia

Serguei G. Soloviev, Sergey G. Kryazhev, Svetlana S. Dvurechenskaya

PII: S0169-1368(16)30259-1
DOI: http://dx.doi.org/10.1016/j.oregeorev.2017.02.029
Reference: OREGEO 2131

To appear in: *Ore Geology Reviews*

Received Date: 13 May 2016
Revised Date: 22 February 2017
Accepted Date: 24 February 2017

Please cite this article as: S.G. Soloviev, S.G. Kryazhev, S.S. Dvurechenskaya, Geology, Mineralization, Stable Isotope, and Fluid Inclusion Characteristics of the Vostok-2 Reduced W-Cu Skarn and Au-W-Bi-As Stockwork Deposit, Sikhote-Alin, Russia, *Ore Geology Reviews* (2017), doi: http://dx.doi.org/10.1016/j.oregeorev.2017.02.029

Geology, Mineralization, Stable Isotope, and Fluid Inclusion Characteristics of the Vostok-2 Reduced W-Cu Skarn and Au-W-Bi-As Stockwork Deposit, Sikhote-Alin, Russia

Serguei G. Soloviev*, Sergey. G. Kryazhev, and Svetlana S. Dvurechenskaya****

**Int'l GeoSol Consulting Inc.*
189 – Scripps Landing N.W. Calgary, AB Canada T3L 1W1

***Russian Central Geological Prospecting Institute (TsNIGRI)*
129-B - Warshawskoe Chaussee, Moscow, Russia 113545

E-mail: serguei07@hotmail.com

Abstract

The large (>180 Kt WO_3 and at least 10-15 t Au) Vostok-2 deposit is situated in a metallogenic belt of W, Sn-W, Au, and Au-W deposits formed in late to post-collisional tectonic environment after cessation of active subduction. The deposit is related to an ilmenite-series high-K calc-alkaline plutonic suite that, by its petrologic signatures, is transitional between those at W-dominant and, on the other hand, Au-dominant reduced intrusion-related deposits. Consistently, besides large W-Cu skarns of the reduced type, the deposit incorporates quartz stockworks with significant Au-W-Bi mineralization also formed in a reduced environment. The hydrothermal stages include prograde and retrograde essentially pyroxene skarns, hydrosilicate (amphibole, chlorite, quartz) alteration, and phyllic (quartz, sericite, albite, apatite, and carbonate) alteration assemblages. These assemblages contain abundant scheelite associated with pyrrhotite, chalcopyrite and, at the phyllic stage, also with Bi minerals, As-Bi-Sb-Te-Pb-Zn sulfides and sulfosalts, as well as with Au mineralization. The fluid evolution included hot, high-pressure (420-460^{o}C, 1.1-1.2 kbar), low-salinity (5.4-6.0 wt.% NaCl-equiv.) aqueous fluids at the retrograde skarn stage, followed by lower temperature cyclic releases of high-carbonic, low salinity to non-carbonic moderate-salinity aqueous fluids. At the hydrosilicate stage, a high-carbonic, CH_4-dominated, hot (350-380^{o}C) low salinity fluid was followed by cooler (300-350^{o}C) non-carbonic moderate-salinity (5.7-14.9 wt.% NaCl-equiv.) fluid. At the phyllic stage, a high-carbonic, CO_2-dominated, moderately-hot (330-355^{o}C, 0.9 kbar) low salinity fluid was followed by cooler (230-265^{o}C) non-carbonic moderate-salinity (6.6-12.0 wt.% NaCl-equiv.) fluid. A homogenized magmatic source of water ($\delta^{18}O_{H2O}$ = +8.3 to +8.7 ‰), and a sedimentary source of sulfur ($\delta^{34}S$ = -6.9 to -6.2 ‰) and carbon ($\delta^{13}C_{fluid}$ = -20.1 to -14.9 ‰) at the hydrosilicate stage are suggested. A magmatic source of water ($\delta^{18}O$ = +8.6 to +9.2‰) and a sedimentary source of sulfur ($\delta^{34}S$ = -9.3 to -4.1‰) but a magmatic (mantle- to crustal-derived) source of carbon ($\delta^{13}C_{fluid}$ = -6.9 to -5.2‰) are envisaged for fluids formed the early mineral assemblage of the phyllic stage. Then, the role of sedimentary carbon again increased toward the intermediate ($\delta^{13}C_{fluid}$ = -16.4 to -14.5 ‰) and late ($\delta^{13}C_{fluid}$ = -16.3 to -14.7 ‰) phyllic mineral assemblages. The magmatic differentiation was responsible for the fluid enrichment in W, whereas Au and Bi could also have been sourced from mafic magma. The decreasing temperatures, together with elevated Ca content in non-boiling fluids, promoted scheelite deposition at the early hydrothermal stages. The most intense scheelite deposition at the phyllic stage was caused by CO_2 removal due to boiling of CO_2-rich fluids; further cooling of non-boiling fluids favoured joint deposition of scheelite, Bi and Au.

Keywords: reduced skarn; intrusion-related gold; tungsten; fluid inclusions; Sikhote-Alin; Russia

1. Introduction

Reduced intrusion-related Au deposits have been identified as a distinct class of mineral deposits associated with reduced (ilmenite-series, after Ishihara (1981)) plutonic suites and represented by a broad spectrum of mineralization styles (auriferous veins, stockworks, hydrothermal breccias, replacement zones, etc.) formed under reduced conditions at mostly moderate to shallow depths (e.g., Thompson et al., 1999; Lang and Baker, 2001; Hart, 2007). These Au deposits occur within Sn-W metallogenic belts and locally contain W mineralization (Thompson et al., 1999; Maloof et al., 2001; Mair et al., 2006). In many such belts, large W skarn deposits of the reduced type (Einaudi et al., 1981; Kwak and White, 1982) are also present (e.g., the MacTung and CanTung W skarn deposits in the Tintina-Tombstone Gold Belt of Yukon-Alaska; Dick and Hodgson, 1982; Rasmussen et al., 2011). This suggests the reduced W skarn deposits are genetically related to the Au deposits in broader Au-W magmatic-hydrothermal systems. However, deposits with large (and even economic) resources of both W and Au are rather rare that constitutes an apparent gap in reduced intrusion-related Au-W deposit model. Thus studying such combined W-Au deposits can contribute to establishing a continuum between reduced W skarn deposits and reduced intrusion-related Au deposits.

The Vostok-2 deposit situated in the Primorie region of the Russian Far East bears significant W, base metal (Cu, Bi), and Au mineralization. It is part of an emerging belt of reduced intrusion-related Au deposits coincident with the long-known Sn-W metallogenic belt extending along the Western Pacific coast. The deposit was discovered in 1961, and since 1969 is mined first by an open pit, and then by underground operations. The deposit initially contained in excess of 180 Kt WO_3 and at least 10-15 t Au, with the ores averaging 1.7% WO_3 and 0.64% Cu; Au grades vary from fractions of g/t to 5-7 g/t (Gvozdev, 2006; Soloviev and Krivoschekov, 2011). During 1969-1999, no less than 43.5 Kt Cu, 2.3 Kt Bi, 23 t Ag, and 8.5 t Au have also been recovered from the deposit (Gvozdev, 2006). In 2010 (after over 40 years of mining), the remaining reserves at deep levels were reported at about 36 Kt WO_3 averaging 1.84% WO_3, 0.70% Cu, 0.04% Bi, 6.1 g/t Ag, and 1.9 g/t Au (Belyansky et al., 2011).

2. Regional Tectonic and Metallogenic Setting

The Vostok-2 deposit is situated in the central part of the Mesozoic Sikhote-Alin orogenic system that extends for over 1200 km north-south along the Western Pacific coast and includes a series of terrains accreted to the eastern Asian continental margin during the Paleozoic and Mesozoic (Fig. 1) (e.g., Khanchuk et al., 1997, 2016; Khanchuk,

2000). Following the Triassic-Late Jurassic subduction, with a west-dipping subduction zone, the Mesozoic collisional processes occurred in the environment of the plate sliding along large fault zones and defining a transform tectonic regime of the Californian type, with the development of turbidite basins in the Late Jurassic-Early Cretaceous and further cessation of convergent plate movements (Khanchuk et al., 1997). Consistently, from west to east, terrains of the Jurassic accretionary prism and Early Cretaceous turbidite terrains are distinguished, the latter reflecting the evolution from subduction to sliding of the oceanic plate along the continental margin.

The main collision stage (Berriasian-Barremian) was dominated by a transform tectonic environment comprised of strike-slip movements along the Central Sikhote-Alin fault accompanied by intense thrust-faulting and folding, and the emplacement of granitic intrusions at 140-125 Ma. During the later (Aptian-Cenomanian) collisional, possibly late to post-collisional stage, the movement along the Central Sikhote-Alin fault was accompanied by development of local pull-apart sedimentary basins (Kruk et al., 2014) and the most intense granitic magmatism at 110-95 Ma occurring both in the amalgamated Late Jurassic terrains and in the Late Jurassic-Early Cretaceous turbidite basins. At this final stage of the transform continental margin development, collision of Mesozoic terrains with the Asian continent was complete, with the Aptian-Cenomanian deformations getting younger from west to east. Overall, the Middle Jurassic-Cenomanian collisional processes have caused tectonic piling of terrains, with corresponding development of granitic continental crust some 30-40 km thick. The subduction-related processes re-commenced in the Late Cretaceous-Paleogene causing the formation of the Eastern Sikhote-Alin volcanic belt (Khanchuk et al., 1997, 2016; Khanchuk, 2000).

The Sikhote-Alin metallogenic province includes numerous granite-related W deposits, which differ in composition and style of mineralization (skarn, stockwork, greisen) (Fig. 1). In particular, the W-base metal deposits (Vostok-2, Lermontovskoe, Skrytoe etc.) are associated with the Early-Late Cretaceous (~111-112 to 101 Ma) high-K calc-alkaline monzodiorite-granodiorite-granite suites emplaced into the amalgamated Late Jurassic terrains (e.g., Rub et al., 1982; Kovalenko et al., 1988). Contemporaneous postcollisional monzonitic (shoshonitic) suites (locally with coeval picrite-trachybasalt-trachyandesite volcanics; Kovalenko et al., 1988; Khanchuk et al., 1997) occur in the Late Jurassic-Early Cretaceous turbidite basins and are accompanied by Cu-Au porphyry mineralization (Khanchuk, 2000). The Late Cretaceous (114-95 Ma) granodiorite-granite plutons are associated with W-Sn mineralization, and the Late Cretaceous-Paleogene (73-53 Ma) Li-F leucogranitic suites are accompanied by W-Sn-Be-Ta mineralization (e.g., Tigrinoe, Zabytoe deposits; Rub et al., 1982) (Fig. 1). In total, these W deposits reflect the evolution of W-bearing orogenic granitic magmatism of the Central Sikhote-Alin (Soloviev, 2008). The re-commenced Late

Cretaceous-Paleogene subduction in the Eastern Sikhote-Alin belt was accompanied by formation of Sn-base metal deposits resembling the Bolivian Sn deposits (Gonevchuk et al., 2010).

The Vostok-2 and other W-base metal deposits containing Au mineralization are also part of the recently established Au metallogenic belt in the Central Sikhote-Alin (Fig. 1). The latter incorporates a number of Au deposits, with the Glukhoe, Blagodatnoe, and especially Malinovskoe Au deposits being the most significant; some of them are found in close proximity with skarn and stockwork scheelite deposits such as Kordonnoe, Skrytoe etc. These Au deposits are characterized by common scheelite, arsenopyrite, pyrrhotite in Au-bearing zones of silicification and sericitization, intense quartz veining and stockwork associated with uneroded or weakly eroded Early-Late Cretaceous granitic plutons, and by their signatures correspond to reduced intrusion-related Au deposits.

3. District Geology

The deposit is situated within a collage of terrains accreted to the eastern boundary of the Asian craton (Fig. 1) and composed of tectonically piled and locally overthrusted sheets (slices) of fine-grained Jurassic turbidites alternating with tectonic melange units, units of oceanic formations, and units with gradual transition from oceanic cherts to turbidites. The turbidites, locally with signatures of slumps and graded bedding possibly formed on a slope of submarine trough, also contains inclusions of oceanic crust fragments, such as Devonian ophiolites, Upper Paleozoic and Triassic cherts, Upper Paleozoic limestones and basalts (Izosov et al., 1988; Khanchuk, 2000). Thrusting of Middle Jurassic tectonic-sedimentary units over Upper Jurassic units was locally reported (Khanchuk, 2000). A series of NE-trending faults divide the terrain into elongated domains extending as narrow lenses in the NW and north direction; to the east, the terrain is bordered by an Early Cretaceous turbidite terrain. The rocks form asymmetric overturned folds, with axial planes striking north-east and dipping south-east. Locally, strongly carbonaceous units are present, with the distribution of graphitic material apparently controlled by fault zones.

In the deposit area, this tectonized sedimentary sequence was intruded by Cretaceous plutons, with the largest of them being elongated in the northeastern direction and splaying of the Central Sikhote-Alin fault, including the large Early Cretaceous (from 128±16 Ma to 103±1 Ma by whole-rock isochron Rb-Sr method) Dalnensky pluton and the Early-Late Cretaceous (98±15 Ma by whole-rock isochron Rb-Sr method) Biserny and Kayalinsky plutons (Fig. 2) (Rub et al., 1982; Kovalenko et al., 1988; Krymsky et al., 1998). The Dalnensky pluton is composed of peraluminous to meta-aluminous biotite-amphibole diorite, monzodiorite and granodiorite, whereas the Biserny and Kayalinsky plutons comprise mostly peraluminous granites (Table 1). The granitic rocks of the large plutons were

formed due to mantle magma-induced melting of crustal sources composed of terrigenous sedimentary and metamorphosed mafic igneous rocks, the latter being enriched in radiogenic Nd (possibly oceanic basalts of the MORB and OIB types), with further mixing of mafic and granitic magmas (Krymsky et al., 1998; Kruk et al., 2014; Jahn et al., 2015). These large granitic plutons are accompanied by weak W to Sn-W mineralization, heavy concentrate anomalies of cassiterite, wolframite, and scheelite, and geochemical Sn and W anomalies. Small stocks and dikes of mafic, intermediate, and granitic rocks are arranged along a NNW-trend marking the concealed NNW-trending fault that is transverse to the strike of sedimentary rock units, large plutons, and NE-striking tectonic zones (Fig. 2). The Vostok-2 deposit is associated with a small (2.5 km^2) granodiorite stock ("the Central stock") localized at an intersection of this concealed NNW-trending fault and NE-striking tectonic zone, apparently a splay of the Central Sikhote-Alin fault. This NE-striking tectonic zone coincident with a NE-striking limestone lens controls mineralized zones of the Vostok-2 deposit.

4. Deposit Geology

The deposit is found in an extended linear NE-trending tectonic zone occurring within a thick olistostrome sequence and steeply (60°-80°) dipping to the northwest (Izosov et al., 1988). The zone is approximately 1 km wide and is roughly conformable to the orientation of alternating steep-dipping lenses and sheets of chert (quartzite), carbonate rocks and mafic volcanic rocks hosted by turbidites (Fig. 3). One elongated (lenticular) lens of carbonate rock ranging from 60 m to 110 m (averaging 70-85 m) in thickness, extending northeast for some 5 km was partially replaced by skarn, whereas adjacent turbidite was converted into biotite hornfels, so that the skarn is surrounded (enveloped) by a halo of biotite hornfels (Fig. 4), with the skarn-hornfels zone extending northwest for a total of 2.5 to 3.0 km. The skarn-hornfels package is intruded by the Central stock and a series of smaller intrusives. The skarn is partially overprinted by linear zones of hydrosilicate (amphibole-dominated) and phyllic (quartz-sericite-carbonate-albite) alteration replacing skarn and occurring also outside skarns in the host hornfels, to a lesser extent, in chert and in the Central stock. Superposition of retrograde-altered skarn and overprinting mineralized zones of hydrosilicate and phyllic alteration defines the main W-sulfide orebodies.

The largest skarn body is divided by the Central stock but mineralized phyllic alteration zones overprint the stock at higher levels thus "sealing" the disconnected skarns into a large single continuous orebody. This large tabular (sheet- to lens-shaped) steep-dipping orebody attains 50 m in thickness and extends for 800 m along strike, and for 700-800 m downdip, where it splits into several smaller parallel mineralized lenses (Fig. 3). A series of nearly

parallel small mineralized zones (orebodies) are also localized in the hanging wall of the main orebody. Small relict lenses of limestone, biotite hornfels, quartzite, and unaltered skarn remain within the orebodies. Outside the skarn, zones of phyllic alteration form an external halo of quartz-sericite-carbonate-albite-sulfide veins and stockworks. These veins are controlled by several fracture systems, with dominant NE-striking (30°-60°NE), shallow (15°-40°) SE- and steeper (50°-80°) NW-dipping fractures, together with NW-striking (330°-345°), steep (60°-90°) NE- and SW-dipping fractures. Scheelite is abundant in retrograde-altered skarn, hydrosilicate and phyllic alteration assemblages, with the highest WO_3 grades occurring in zones of superimposed alteration types. Most of sulfide mineralization associated with hydrosilicate (propylitic) alteration of skarn is focussed within the inner parts of the main orebody, whereas Au mineralization is associated with phyllic alteration and occurs thorough the main orebody and in the adjacent host rocks including the altered Central stock.

5. Analytical Methods

The analyses of igneous rocks were performed in the Russian Analytical Centre (VIMS) Laboratories, Moscow. SiO_2, TiO_2, Al_2O_3, $Fe_2O_{3\ total}$, MnO, MgO, CaO, K_2O, and P_2O_5, as well as Sr, Nb and Zr, were determined by X-ray fluorescence method using a multi-channel X-ray spectrometer. Supplementary determinations by wet chemical methods included FeO (volumetric method), Na_2O (flame photometry), F (ion chromatography), CO_2 (acidometry), S_{total} (iodometry), H_2O-+ (gravimetry). In addition, Li, Rb, and $\Sigma REE_2O_3+Y_2O_3$, were also determined by flame photometric method. Powdered samples were digested in four acids, and ICP-ES method was used for determination of Ni, Co, V, Be, Sn, Mo, Y, B, Cu, Zn, and Pb. Also, X-ray radiometric method was used for determination of Ba, and neutron activation method – for determination of W. Detection limits: SiO_2 – 0.50 wt.%, TiO_2 – 0.02 wt.%, Fe_2O_3 and FeO – 0.25 wt.%, MgO, CaO, Na_2O, K_2O and CO_2 – 0.20 wt.%, P_2O_5 – 0.04 wt.%, H_2O and $S_{tot.}$ – 0.10 wt.%, MnO and F - 0.02 wt.%, Ba, Sr, Zr – 20 ppm, Co, V, Nb, Sn, Y and Rb – 5 ppm, Li, B, Cu, Zn, Pb, and Ni – 1 ppm, Be, Mo, and W – 0.1 ppm. Analytical errors are 0.5-5% for major elements and 1-10% for trace elements, depending on the concentrations. The analyses of igneous rocks for REE and some rare elements was performed in the Russian Institute of Experimental Mineralogy (IEM RAN), Chernogolovka, by neutron activation method. 100-mg samples were irradiated together with a standard by a thermal neutron flux of 1.2×10^{13} n/cm^2 × s during 20 hr. REE fractions were separated by radiochemical method. Gamma-spectrometry determination of REE was done with a coaxial Ge(Li)-detector. The accuracy of the analyses for individual elements is: ±3%-5% for La, Sm, Eu, Yb, and Lu, ±5%-7% for Ce, Tb, and ±10% for Nd.

The analyses of silicate minerals were performed by Cameca SX50 microprobe in the Moscow State University, Russia, and the analyses of sulfide minerals, as well as native Au and Bi - by Cameca SX50 microprobe in the GEOKHI Institute of the Russian Science Academy (RAN), Moscow, under operating conditions of 15 kV accelerating voltage, 30 nA beam current, with a beam

diameter ~3 μm. The accuracy of element measurements was ±2% rel. for concentrations >10 wt.%, ±5% rel. for concentrations of 5-10 wt.%, ±10% rel. for concentrations of 1-5 wt.%, and ±15% rel. for concentrations of 0.1-1.0 wt.%.

For fluid inclusion study, fifty-eight doubly polished sections of 0.3 to 0.5 mm thick were prepared from 26 individual samples for fluid inclusion petrography and microthermometry. Microthermometric analyses were made using the UMTK-3 freezing–heating stage designed by VIMS Institute and modified by TsNIGRI Institute, Russian Geological Survey to allow low-temperature experiments. Cooling is by liquid N_2 flow. The stage employs a chromel–alumel thermocouple and is capable of attaining temperatures ranging from below −180 to over +650 °C. The stage was periodically calibrated using the boiling temperature of pure N_2 (−196 °C), triple point for pure CO_2 (−56.6 °C), temperatures of ice melting in standard NaCl solutions (from −18° to −1°C), melting temperatures of $AgNO_3$ (210°C), K_2CrO_7 (398°C), and NaI (651°C). Final ice-melting temperatures were accurate to ±0.2°C, clathrate melting temperatures to ±0.5°C, eutectic temperatures to ±1.5°C, and homogenization temperatures to ±5°C. Heating rate (at above 30°C) was 5°C/min up to a heating limit at 650°C.

The fluid inclusion study was focused on fluid inclusion assemblages (FIA), i.e., closely associated groups or trails of fluid inclusions with visually similar phase ratios and similar shape (Goldstein and Reynolds, 1994). The sequence of entrapment can be inferred from observations of crosscutting trails of FIA along individual fractures or rare primary inclusions distributed randomly within the core of crystals or pseudosecondary trails that are associated with healed microfractures terminated by crystal growth zones (Roedder, 1984). This also enables linking groups of fluid inclusions to various mineralizing stages on the basis of their absence in younger mineral assemblages (Masterman et al., 2005). Distinguishing of FIA can minimize the effect of homogenization temperature variability of individual inclusions trapped simultaneously, as well as the effect of post-entrapment modifications (Goldstein and Reynolds, 1994).

For the gas chromatography analysis, the analyzed 1-gram quartz and scheelite separates were prepared by magnetic separation and handpicking under a binocular microscope from monomineralic samples crushed in an agate mortar to 0.25-0.5 mm; this was followed by sample cleaning in a HNO_3 aqueous (1:1) solution (e.g., Bottrell et al., 1988) and then by water-flow electrolytic cleaning in ultrasound bath for 3 hours. Following this procedure, the samples were dried and put into a quartz glass reactor vacuumed at 110°C and filled with helium. The opening of fluid inclusions was conducted by heating to 500°C and keeping under this temperature for 15 minutes. The gases extracted were introduced into a gas chromatograph equipped by a gas flow divider to allow simultaneous determination of H_2O, CO_2, and CH_4. Then, the heated samples were leached with de-ionized water in the ultrasound bath for 15 minutes. The leachate solution was separated by centrifuging and then analyzed by ICP-MS (Elan-6100) for the cations (Na, K etc.) and by ion chromatography for the anions (Cl, F, SO_4 etc.). Concentration of HCO_3^- was calculated using the cation/anion balance. The concentrations obtained were normalized to the water content.

Minerals for the isotopic study were extracted by a dental drill and/or by the hand picking of chips. Oxygen was obtained from quartz, pyroxene, and scheelite powder by reaction with BrF_5 using the conventional method of Clayton and Mayeda

(1963), carbon dioxide - from calcite powder by reaction with H_3PO_4 at 75°C using the method of McCrea (1950). Carbon was obtained by heating of quartz and scheelite (preliminary boiled in 1:1 HCl for removal of carbonate impurities) in O_2 media at 750°C for 15 min, with further CO_2 cryogenic purification. Sulfide powders were analyzed by conventional methods using the techniques of Robinson and Kusakabe (1975), with decomposition of sulfides by reaction with CuO at 750°C, with further isotopic analysis of SO_2. The isotope measurements were performed using a MI-1201 mass spectrometer. An analytical uncertainty of ±0.2 per mil (2 σ) for $\delta^{13}C$ and $\delta^{18}O$ was estimated from the international KH-2 ($\delta^{13}C_{PDB}$ = +1.97‰, $\delta^{18}O_{SMOW}$ = +27.8‰) and REF-1 ($\delta^{13}C_{PDB}$ = -31.6‰) standards. An analytical uncertainty of ±0.2 per mil (2 σ) for $\delta^{34}S$ was estimated from internal standards of homogenous pyrite from the Gaiskoe deposit in the southern Urals ($\delta^{34}S_{CDT}$=+0.7‰).

6. Igneous Rocks of the Central Stock

As compare to the large granitic plutons, an intermediate (~111-112±4 Ma to 101±1 Ma) Rb-Sr isotopic age, similar to the whole-rock Rb-Sr age (100-102±1 Ma) of phyllic alteration assemblages at the Vostok-2 deposit, was obtained for the Central stock granodiorite (Rub et al., 1982; Krymsky et al., 1998; Khetchikov et al., 1999). The granodiorite has an initial $^{87}Sr/^{86}Sr$ ratio of 0.70675 (Rub et al., 1982), transitional between those of the Dalninsky (0.7056-0.7071) and Biserny (0.7095-0.7202) plutons (Gerasimov et al., 1994). The granodiorite is most depleted in radiogenic Nd (ε_{Nd} = -3.1 to -5.0), as compared to the rocks of the Byserny and Kayalinsky plutons (ε_{Nd} = 0 to -1) and the Dalnensky pluton (ε_{Nd} = +0.04) (Gvozdev, 2007; Kruk et al., 2014). Consistently, a greater role of sedimentary rock melting was suggested for the Central stock rocks, with a fraction of mantle material approximating 70-80% in the Dalnensky pluton melts, and ~50% in the melts producing the Central stock rocks (Krymsky et al., 1998).

Correspondingly, the Central stock may belong to a relatively separate suite of small porphyry intrusions, possibly satellitic to the large Early Cretaceous plutons, which were productive for W-Au mineralization (Soloviev and Krivoschekov, 2011). This small irregularly-shaped intrusive body, with steep-dipping contacts complicated by apophyses, is composed mostly of granodiorite (monzogranite by modal mineral composition; Le Maitre et al., 2002), which is porphyritic in its upper part, and equigranular in deeper parts of the stock (Table 1). In the south-eastern part of the stock, i.e., toward the mineralized zone, granodiorite grades into “plagiogranite” with higher quartz and plagioclase contents and plagioclase becoming less calcic (Table 1). It cannot be ruled out that the “plagiogranite” is actually an altered granodiorite; on the other hand, distinct zoning of plagioclase does not support such an interpretation. According to Kovalenko et al. (1988), biotite in granodiorite has high Mg (up to 12 wt.%) and Ti (up to 4.5 wt.%) contents. A small (up to 50 m across), funnel-like body of intrusive breccia occurs in the center of the

Central stock and pinches out at a depth of 90-110 m from the surface. Fragments in the breccia include biotite hornfels, quartzite, and skarn, and are cemented by granodiorite. *S*mall (up to several tens of meters across) zoned stocks and dikes of monzogranite- to granite-porphyry found in vicinity to the Central stock crosscut granodiorite. Late mafic dikes include monzodiorite-porphyry and diorite-porphyry (Table 1); these dikes crosscut all granitic rocks in the area, whereas the diorite-porphyry dikes crosscut the monzodiorite-porphyry dikes (Rub et al., 1982).

On the total alkalis vs. SiO_2 diagram (Table 2, Fig. 4A), the Central stock rocks form an array from ~62 to 74 wt.% SiO_2 in the upper part of the calc-alkaline field, marginal to the line dividing the moderate alkaline and calc-alkaline fields, as defined by Middlemost (1997). Granodiorite and monzogranite- to granite-porphyry as well as monzodiorite-porphyry, due to their elevated K content, belong to high-K calc-alkaline series (Fig. 4B). The rocks have also elevated Mg, Ti, P, F, Cr, Co, Ni, V, Ba, and Sr contents, with moderate Rb and low Li, Be, Nb, Mo, and Sn contents. In contrast, the "plagiogranite" has higher CaO and Na_2O ($Na_2O/K_2O > 1$) contents. All rocks of the Central stock are peraluminous (Fig. 4C), and are characterized by a sharp to weak predominance of FeO over Fe_2O_3; the latter, together with the constant presence of ilmenite among accessory minerals, indicate their reduced (ilmenite-series, after Ishihara, 1981) to weakly-oxidized type. The granodiorite and "plagiogranite" have strong LREE-enrichment (La_N/Yb_N = 11-17) and lack of Eu anomaly; a weak negative Eu anomaly occurs in the granite-porphyry (Table 3). On the Rb vs. Y+Nb diagram, the granitic rocks correspond to post-collisional granites (Fig. 4D).

7. Hydrothermal Assemblages and Ore Mineralization

7.1. Early (district-scale) potassic and propylitic-style alteration

These alteration assemblages overprint the sedimentary volcanic-terrigenous sequence and comprise biotite, amphibole, chlorite, quartz, calcite, K-feldspar, plagioclase, with accessory titanite, ilmenite and trace pyrrhotite (Fig. 5). Biotite predominates, with the rock grading into quartz-feldspar-biotite rock with hornfels texture, referred to as biotite hornfels, although no direct link to any specific intrusive contact is established, at least at the surface. Altered volcanic rocks contain more amphibole and chlorite, locally with epidote. These alteration assemblages occur as steeply dipping bands along lithological contacts of the host sequence splitting along strike into series of elongated lenses and zones. The area of their development exceeds the deposit area and might be related to a larger pluton at depth; however, their most intense development is observed in the NE-trending tectonic zone hosting the deposit. The zones composed of these assemblages are cut by the Central stock granodiorite and are locally overprinted by calcic skarn and post-skarn mineral assemblages.

7.2. Prograde calcic skarn

Several varieties of prograde skarn are distinguished. First, there is zoned (locally thin-banded conformably to lithological contacts) plagioclase-pyroxene and pyroxene-garnet skarn that forms typically narrow (up to a few meters thick) bedding-concordant bodies in the units of alternating aluminosilicate and carbonate metasedimentary rocks (biotite hornfels, chert, marble). On a marble-hornfels contact, the following zonation is developed: biotite hornfels (biotite, quartz, plagioclase, locally amphibole) – pyroxene-plagioclase – pyroxene – pyroxene-garnet (locally with vesuvianite) – marble (calcite) (Fig. 6A). Pyroxene dominates over other minerals. Second, thin (up to 5 cm) branching skarn veinlets crosscutting the host metasedimentary rocks are present; they consist mainly of pyroxene or pyroxene+calcite, locally with wollastonite in marble (Fig. 6B). Third, massive skarn forms large bodies representing the majority of the deposit skarns; it contains relicts of marble indicating that at least part of it was formed after carbonate rocks. The primary zoning of the largest prograde skarn body is almost completely obliterated by retrograde skarn and post-skarn mineral assemblages. The prograde skarn relicts preserved from later alteration are composed of fine-grained pyroxene containing 65-72 mol.% hedenbergite (Table 4). Garnet is rare (< 2 vol.%), also fine-grained, and dominantly contains grossular, with 31-44 mol.% andradite.

7.3. Retrograde skarn

The retrograde skarn assemblages are typically confined to the limits of prograde skarn bodies. They include that composed of pyroxene-quartz (Fig. 6C) with subordinated amphibole, plagioclase, garnet, and sulfides (mostly pyrrhotite, minor chalcopyrite) replacing prograde pyroxene skarn, and those composed of plagioclase-quartz or amphibole-quartz-plagioclase replacing prograde plagioclase and plagioclase-pyroxene skarn. The alteration starts with introduction of ubiquitous quartz corroding prograde skarn minerals, with their further pervasive to patchy replacement and/or re-crystallization of pyroxene (and garnet, where present) into euhedral and larger crystals, locally their coarse-grained aggregates. The newly-formed pyroxene contains 85-90% mol.% hedenbergite and 7-11 mol.% johannsenite; rare garnet contains 9-21 mol.% andradite, 8-9 mol.% spessartine, and 9-21 mol.% almandine (Table 4). The retrograde character of this skarn is also supported by minor but ubiquitous amphibole (ferroactinolite; Table 5) and chlorite. Plagioclase is oligoclase to andesine. Scheelite is consistently present, although in subordinate amounts (Figs. 6C, 7A); it has pale yellow luminescence and a low Mo content (0.05-0.5 wt.% MoO_3) (Soloviev and Krivoschekov, 2011). The retrograde skarn typically contains less than 0.5 wt.% WO_3. The Central stock granodiorite

crosscuts prograde and retrograde skarns; skarn fragments are cemented by granodiorite of the intrusive breccia (Fig. 6D-E).

7.4. Hydrosilicate ("inner propylitic") alteration

Hydrosilicate alteration assemblages overprint and replace prograde and retrograde skarns and locally exceed the contours of skarns spreading into the host rocks. They include quartz-amphibole, locally biotite-amphibole-quartz, and amphibole-chlorite-quartz assemblages (Figs. 7B-C). Pyrrhotite, scheelite and chalcopyrite are abundant, locally forming massive sulfide and sulfide-scheelite aggregates (Figs. 6F-G). Minor minerals include calcite, oligoclase-albite, epidote-zoisite, and titanite. Amphibole is especially abundant in the outer zones of hydrosilicate alteration of skarns, locally with minor chlorite (ripidolite; Table 5), whereas the inner zones are typically composed of pyrrhotite and quartz, locally with chalcopyrite. Amphibole is represented by a low-Fe variety (actinolite to tremolite; Table 5). Biotite and/or phlogopite are present in the outermost alteration zones, especially if the alteration exceeds the skarn limits and overprints the host hornfels, and are coarser-grained and more ferrous than that from biotite hornfels (Table 5). Scheelite has white luminescence and a very low Mo content (0.01–0.05 wt.% MoO_3), is enriched in LREE and contains no anomalous Eu (Soloviev and Krivoschekov, 2011). Retrograde skarn overprinted by hydrosilicate alteration typically contains 1-2 wt.% WO_3. Pyrrhotite locally occupies up to 80-90 vol.% and belongs to monoclinic modification. Molybdenite is very locally present in the biotite-rich assemblage. Aluminosilicate rocks (granodiorite, etc.) adjacent to hydrosilicate alteration zones are replaced by fine- to medium-grained oligoclase-quartz (with minor amphibole and chlorite) aggregate, which also contains scheelite.

7.5. Quartz-sericite±carbonate±albite (phyllic) alteration

This alteration assemblage overprints granodiorite of the Central stock and almost entirely replaces its uppermost part including intrusive breccia with granodiorite cement and adjoining metasedimentary rocks. It also overprints monzogranite- to granite-porphyry dikes, but is cut by the monzodiorite-porphyry and diorite-porphyry dikes. This assemblage forms a series of veins, veinlets, larger stockworks, zones of sheeted veins, and zones of pervasive replacement, and locally hydrothermal breccia (Fig. 6H-L). The alteration starts with the development of plagioclase (albite An_{5-10}) associated with chlorite (picnochlorite; Table 5), with subordinate quartz, adularia, carbonate, and muscovite-sericite, and evolves through the assemblage of carbonate, muscovite-sericite, and quartz, to that dominated by muscovite-sericite and quartz (Figs. 7D-E). The feldspar-rich and quartz-micaceous

assemblages are expressed most in the Central stock granodiorite, whereas the quartz-carbonate-micaceous assemblages – in the altered skarns and metasedimentary rocks. The WO_3 grade in the skarn overprinted by phyllic alteration is high (locally >10 wt.%). Sulfide content is typically low (<5-10 vol.%), but locally increases in the assemblages overprinting altered skarns with abundant sulfides.

Scheelite occurs in association with carbonate, albite, and most typically with apatite, the latter being locally abundant (up to 15-20 vol.%) (Figs. 6L, 7E-G). At least two generations of scheelite are distinguished. The early scheelite occurs in quartz-arsenopyrite assemblage locally attaining 10-15 vol.%: it contains only minor Mo (0.005-0.01 wt.% MoO_3) and has white-blue luminescence. The late scheelite occurs in assemblages with other sulfides; it contains no Mo, has blue luminescence, and is characterized by excess of Eu (Soloviev and Krivoschekov, 2011). The scheelite-arsenopyrite assemblage occurs mostly close to or within the Central stock, whereas scheelite-pyrrhotite-chalcopyrite and scheelite-chalcopyrite assemblages are more distal. Pyrrhotite from the phyllic assemblages belongs to both monocline and hexagonal modifications. Sphalerite (marmatite) replaces pyrrhotite, early arsenopyrite, and chalcopyrite but also contains pyrrhotite, chalcopyrite, and stannite emulsions. Rare wolframite (ferberite) forms small crystals in chalcopyrite.

The phyllic alteration assemblages contain significant Bi and Au mineralization closely associated with scheelite and sulfides (Fig. 7G-R, Table 6). Bismuth minerals include the most abundant native Bi, bismuthinite, various Bi tellurides and sulfosalts, with bismuthinite-native Bi assemblage associated with chalcopyrite and scheelite, and sulfotelluride-Pb-Sb-Bi-sulfosalt assemblage associated with galena and other late sulfides. The larger Au-bearing intervals (1-3 g/t Au over 10-30 m) are in phyllic alteration zones with high or moderate sulfide content. Gold mineralization is represented by fine (<0.1 mm) to coarser (up to 0.4 mm) grains of native Au and electrum (Table 6) in sulfides, scheelite, and quartz, as well as by Au finely dispersed in sulfides. According to Stepanov and Gvozdev (1987) and Gvozdev and Tsepin (2005), low fineness native Au and electrum (48 wt.% Ag) are associated with native Bi; medium fineness native Au - with Pb-Sb-Bi sulfosalts and hedleyite, and high fineness (16 wt.% Ag) native Au occurs as microinclusions in chalcopyrite.

8. Fluid Inclusion Analysis

The present study was focused on fluid inclusions in hydrothermal mineral assemblages using the mineral paragenesis described above (Fig. 5). In prograde skarn minerals, we identified no fluid inclusions confidently regarded to as primary ones and without post-entrapment modifications. Consistently, fluid inclusions were studied in

minerals from the retrograde skarn, hydrosilicate and phyllic alteration assemblages (Table 7). The samples for this study were taken from the open pit (<30 m depth) and from underground adits at elevations 800 m and 720 m.

8.1. Fluid inclusions in retrograde skarn minerals

Primary fluid inclusions were observed and measured in pyroxene, quartz, and scheelite from the retrograde skarn. They are represented by multiphase (multisolid) inclusions (type 1) that are rare and typically occur as isolated individuals (Table 7; Fig. 8A-B). Some of these inclusions, besides containing a vapor bubble (~20-25 vol.%) and liquid phase, contain up to 4 solid phases with unstable volume ratios (from <5 vol.% to 50 vol.%), with all of them being strongly to weakly anisotropic and colorless (to semi-transparent white).

On heating, the type 1 inclusions with minimal (<5 vol.%) volume of solid phases exhibit disappearance of a gas bubble at 340-360°C (Table 7; Fig. 9A). Heating to higher temperatures caused decrepitation of these inclusions at 530-550°C, with no even partial dissolution of the solid phases. Initial ice melting temperatures on freezing/warming were not confidently obtained; however, the final ice melting temperature at -3.7 to -3.3°C was consistently observed. In the pure NaCl-H_2O system, this corresponds to a salinity of 5.4 to 6.0 wt.% NaCl-equiv. (Bodnar and Vityk, 1995) (Table 7).

8.2. Fluid inclusions in hydrosilicate (propylitic) alteration minerals

Fluid inclusions were observed and measured in quartz and scheelite from the hydrosilicate alteration assemblages overprinting retrograde skarn. They are represented by gaseous-liquid to aqueous liquid-gaseous inclusions (type 2 inclusions) (Table 7). They are typically small to medium sized (5-25 μm), irregular to negatively crystalline in shape, and they occur mostly as isolated individuals, in clusters, and also in short trails (Fig. 8C-F). Two varieties of the type 2 fluid inclusions are distinguished (Table 7). The type 2A inclusions contain nearly equal amounts of liquid and gaseous phases (40-50 vol.% gas) and are homogenized into liquid phase at 350-380°C (Fig. 9A). These inclusions contain a carbonic phase including significant methane that is evidenced by clathrate final melting temperatures in the range of +10.5 to +16.5°C (Burruss, 1981). In contrast, the type 2B inclusions (locally forming short trails suggesting they are pseudosecondary and thus slightly younger than the type 2A inclusions) are liquid-gaseous (25-40 vol.% gas) and homogenize to liquid at 300-350°C. Locally, the type 2B inclusions contain an anisotropic short-prismatic to bipyramidal colorless or semitransparent white solid phase, and also a very small

opaque solid phase (Fig. 8E). The type 2B inclusions contain little or no carbon. On freezing/warming, the type 2A and 2B inclusions exhibit eutectic first melting temperatures of −29.0±0.5°C and −31.5±0.5°C, respectively, suggesting the presence of NaCl, as well as Mg and Ca chlorides in solution (Crawford et al., 1981). Salinity estimates in the NaCl-H_2O system, based on the final ice melting temperatures (from −3.5 to −10.9°C) of the type 2A and 2B inclusions, indicate salinity of 5.7 to 7.2 and 9.6 to 14.9 wt% NaCl-equiv., respectively (Bodnar and Vityk, 1995; Table 7).

8.3. Fluid inclusions in phyllic alteration minerals

Primary and pseudosecondary fluid inclusions found in the quartz and scheelite from phyllic alteration zones are represented by at least two types (Table 7; Fig. 8G-K), which correspond to the early quartz-arsenopyrite and intermediate quartz-scheelite-arsenopyrite assemblages (type 3 inclusions) and to the late quartz-sulfide-bismuth-gold assemblages (type 4 inclusions), respectively. These inclusions are gaseous-liquid to liquid-gaseous (type 3) or liquid-gaseous (type 4) and, in contrast to the type 2 inclusions, contain only minor methane, and abundant CO_2. These inclusions are secondary in minerals of earlier retrograde skarn and hydrosilicate alteration assemblages.

The type 3 inclusions typically occur in variably-sized clusters, locally in core and growth zones of quartz crystals, and also in short trails, have variable size (from 5 to 40 μm) and shape (from negative crystals to irregular). They vary from liquid-gaseous to gaseous-liquid and contain a relatively large gas bubble occupying either some 40-60 vol.%, or >95 vol.% (Fig. 8G-J). Consistently, two varieties of the type 3 fluid inclusions are distinguished (Table 7). The type 3A inclusions contain an abundant carbonic phase (>95 vol.%) and, on warming after freezing, exhibit CO_2 melting temperature at -64.0 to -61.5°C indicating methane is also present, with CH_4 mole fractions estimated to range from 0.40 to 0.25 (Fig. 9B) (Thiery et al., 1994). In contrast, the type 3B inclusions contain nearly equal amounts of carbonic and aqueous phases (40-60 vol.%). On warming after freezing, they exhibit CO_2 melting temperature at -62.5 to -59.3°C, with CH_4 mole fractions estimated to range from 0.25 to 0.10 (Fig. 9B) (Thiery et al., 1994). The clathrate melting temperatures up to +11.7°C support the presence of methane in the type 3B inclusions; salinity estimate in the NaCl-CO_2-H_2O system, based on the final clathrate melting temperatures of +9.0 to +11.7°C, indicates low salinity of the fluids in the range of 1 to 2 wt.% NaCl-equiv. (Darling, 1991), although this may be affected by presence of methane. The type 3B inclusions are fully homogenized at 330-355°C by dissolution of CO_2 in water near the two-phase equilibrium line.

The presence of the carbonic type 3A inclusions and aqueous-carbonic type 3B inclusions in the same clusters and trails provides additional evidence for considering them as trapped contemporaneously in the two-phase immiscible field. If so, the trapping pressures for these fluid inclusions can be established using trapping temperatures (330-355^{o}C) for the high-density type 3B fluid inclusions and densities for the low-density type 3A fluid inclusions (e.g., Roedder, 1984). The densities for the type 3A inclusions containing various fractions of methane in addition to CO_2 can be determined using the diagrams from Thiery et al. (1994) (Fig. 9B). Using the computing programs of Bakker (2003), the trapping pressure is estimated at 890-910 bar. This pressure corresponds to a depth of 3.3-3.6 km assuming purely lithostatic conditions, and to a depth of ~9 km assuming purely hydrostatic conditions (Fournier, 1999). Whereas the depth of ~9 km appears to be too great, the depth of ~3.5 km is consistent with the porphyry features of the Central stock and presence of intrusive and hydrothermal breccias. The magmatic fluid could have been exsolved at a greater depth (at higher pressure), whereas the fluid boiling could have been caused by a pressure drop from higher values to ~900 bars that would be coincident with the change from lithostatic to hydrostatic conditions. The pressure drop may be related to intense fracturing, whereas the overpressurized fluid could also contribute to hydrothermal breccia formation. Due to the fluid boiling, no pressure correction is necessary for the homogenization temperature of 330-355^{o}C.

The type 4 inclusions are the most abundant and also occur in clusters and variously-oriented trails. These inclusions are distinctly younger than fluid inclusions of the other types: their trails intersect trails and clusters formed by the other fluid inclusion types. The type 4 inclusions have variable size (from <5 to 40 μm) and shape (from negative crystals to irregular). They are liquid-rich and contain a relatively small gas bubble typically occupying 15-30 vol.% (Fig. 8K). Salinity estimate in the NaCl-H_2O system, based on the final ice melting temperatures (from −4.1 to −8.3°C), yields salinity of 6.6 to 12.0 wt.% NaCl-equiv. (Bodnar and Vityk, 1995; Table 7). On freezing/warming, these inclusions exhibit eutectic temperatures of −24.5±1.0°C, indicating the presence of predominating Na chloride in solution (Crawford et al., 1981). The inclusions are fully homogenized into liquid phase at 230-265°C (Fig. 9A); this temperature is consistent with the presence of native bismuth ($T_{melting}$ = 271.4^{o}C) in this mineral assemblage. Small droplet-like native Bi aggregations are locally observed suggesting a possible presence of melted native Bi in the fluids (e.g., Tooth et al., 2008); this may further suggest that the actual temperature of the fluid was slightly higher.

8.4. Bulk fluid geochemistry

The results obtained by the bulk gas chromatography method are affected by the presence of secondary inclusions and must be taken with caution. Nevertheless, these results (Table 8) show the strong predominance of Na among cations in fluids at all hydrothermal stages studied. A higher K content was recorded for fluids forming the retrograde skarn, and a higher Fe, Mg, and Ca content – for fluids forming the hydrosilicate assemblage. Calcium content is elevated in fluids extracted from scheelite of the hydrosilicate assemblage, whereas Ca is absent in fluids extracted from scheelite essentially formed during the phyllic stage. Methane, together with CO_2, are important in the fluids forming the hydrosilicate assemblage, but the amount of CO_2 sharply increases in the phyllic stage fluids that is also consistent with microscopic observations. Consistently, the fluids trapped during formation of the hydrosilicate stage minerals are characterized by a low CO_2/CH_4 ratio indicating reduced conditions. The fluids conserved in the phyllic stage minerals are characterized by a higher CO_2/CH_4 ratio indicating a higher oxidation state (Table 8).

9. **Stable Isotope Analysis**

9.1. Oxygen and carbon isotopes

Oxygen isotopes were studied in quartz and pyroxene from the retrograde skarn, quartz, and scheelite from the hydrosilicate alteration assemblages, and in quartz, scheelite and calcite from the phyllic alteration assemblages (Table 9). The oxygen isotope data indicate quite uniform $\delta^{18}O_{H2O}$ values (+7.3 to +9.3 ‰) for the retrograde skarn, hydrosilicate, and phyllic stages (Fig. 10A). The oxygen isotope distribution in jointly crystallized pairs of minerals (e.g., quartz-pyroxene, quartz-scheelite) was used to calculate the temperatures of the isotopic equilibria (Faure, 1986; Wesolowski and Ohmoto, 1986). Notably the isotopic equilibrium temperatures (450-470^{o}C) calculated for quartz and pyroxene from the retrograde skarn are consistent with the typical hedenbergite stability temperatures (>450^{o}C; Gustafson, 1974) and are significantly (for ~110^{o}C) higher than the respective fluid inclusion homogenization temperatures. This difference likely corresponds to the "pressure correction" to the homogenization temperatures (340-360^{o}C) in turn allowing estimating the respective fluid entrapment pressure at the retrograde skarn stage, the latter in the H_2O-NaCl system being in the order of 1.2 kbar (Roedder, 1984) or 1.1 kbar (Potter, 1977) (Fig. 9C). The pressure of 1.1-1.2 kbar occurs at a depth of 4.5-5 km under lithostatic conditions (Fournier, 1999).

Carbon isotopes were studied in the fluids extracted from quartz and scheelite of the hydrosilicate and phyllic assemblages (Fig. 10B), with the early phyllic assemblage yielding the highest values ($\delta^{13}C_{fluid}$ = -6.9 to -5.2‰),

whereas much lower values are typical for the hydrosilicate assemblage ($\delta^{13}C_{fluid}$ = -20.1 to -14.9‰) and the intermediate assemblage of the phyllic stage ($\delta^{13}C_{fluid}$ = -16.4 to -14.5‰). The latter values are similar to those determined for calcite from the late assemblage of the phyllic stage ($\delta^{13}C_{fluid}$ = -16.4 to -14.7‰).

9.2. Sulfur isotopes

Sulfur isotopes were studied and $\delta^{34}S$ values determined in sulfides from the hydrosilicate and phyllic alteration assemblages (Table 10). The data indicate strong light sulfur isotope enrichment for all these sulfides. Of note is a quite uniform distribution of the $\delta^{34}S$ values for sulfides from the hydrosilicate assemblage ($\delta^{34}S$ = --6.9 to -6.2 ‰), and less uniform distribution of the $\delta^{34}S$ values ($\delta^{34}S$ = -9.3 to -4.1‰) for sulfides from the phyllic alteration assemblages (Table 10; Fig. 10C).

10. Discussion

The Vostok-2 deposit is of special interest because (1) it represents a large and high-grade W skarn deposit of reduced type (Einaudi et al., 1981; Kwak and White, 1982), and (2) it is an example of reduced W skarn and Au-W stockwork mineralization combined in a complex but single magmatic-hydrothermal system, thus filling in an apparent gap between mostly W and mostly Au deposits formed in reduced intrusion-related environment. This emphasizes their genetic links, thus complementing reduced intrusion-related Au±W deposit model (e.g., Lang and Baker, 2001; Thompson et al., 1999; Hart, 2007).

The Vostok-2 deposit is associated with ilmenite-series, high-K igneous suite and is situated in the W-Sn-Au metallogenic belt, which formed under the late- to post-collisional tectonic regime that occurred after cessation of active subduction. At this stage, possible asthenosphere uplift through a slab window formed in the subducted slab, or asthenosphere mantle ascent caused by lithosphere delamination (Khanchuk, 2000), has resulted in widespread melting of crustal rocks and emplacement of contemporaneous peraluminous granitic suites in the Early-Late Cretaceous (Kruk et al., 2014). Consistently, the Early Cretaceous plutonic rocks of the Central Sikhote-Alin (including the rocks at the Vostok-2 and other W-Au deposits) were formed by mantle-induced melting of crustal sources, and/or due to partial melting of sources with significant proportions of mantle-derived material that intercalated with older continental crust components in the lower part of the Sikhote-Alin basement (Jahn et al., 2015). This explains the mantle-related petrologic affinity of the Early Cretaceous granitic rocks, including those of

the Central stock, such as elevated Mg, Ti, P, F, Co, Ni, V, Ba, and Sr contents, lack of Eu-anomaly, strong LREE-enrichment, presence of high-Mg accessory garnet, and the high-Ti, high-Mg biotite compositions.

The intrusions associated with reduced intrusion-related Au deposits are highly variable mantle-crustal mixtures, with volatile-rich, lithosphere-derived lamprophyric melts interacted and eventually mixed with fractionating and ascending melts from the lower crust (Hart 2007; Mair et al. 2006, 2011). The role of lamprophyric magma interacting with granitic melts was also suggested at the reduced-type Cantung W skarn deposit (Rasmussen at al. 2011). In well-developed accretionary terranes corresponding to the late- to post-collisional environment, ilmenite-series high-K calc-alkaline to shoshonitic igneous suites (generally of granodiorite composition) can be generated by mingling of ascending mafic and felsic magmas, the latter originating from the accretionary complex (Ishihara, 2004; Mair et al., 2006, 2011). Such high-K, ilmenite-series igneous suites include those parental for Sn-base metal (e.g., Mlynarczyk and Williams-Jones, 2005), reduced Au±W intrusion-related (cf. Mair et al., 2011) and some other deposits formed in the late- and post-collisional orogens. Together with subduction-related and late- to post-collisional magnetite-series high-K igneous suites associated with Cu-Au±Mo mineralization, they constitute a diversity of high-K calc-alkaline to shoshonitic suites occurred in different tectonic environments (Ishihara, 2004; Ishihara et al., 2008; Soloviev, 2014; Muller and Groves, 2016). Overall, this highlights the respective difference of W deposits in the late- to post-collisional W-Sn-Au metallogenic belts, as compared to those in subduction-related W-Mo, W-Mo-Cu, W-Mo-Cu-Au metallogenic belts, where W (±Mo, Cu, Au) skarn deposits of oxidized type (Einaudi et al., 1981; Kwak and White, 1982) are related to magnetite-series igneous suites and are locally proximal to Cu-porphyry deposits (e.g., Meinert, 1995).

In this regard, Hronsky et al. (2012) linked Au enrichment of reduced igneous suites to paleo-subduction fertilization of ancient continental lithospheric mantle, whereas Kendrick et al. (2011) suggested a global link between reduced Au deposits and methane-dominated mantle degassing caused either by serpentinization of ultramafic rocks in the upper mantle or by release of CH_4-rich fluids from a deeper mantle source. Taking into account close geochemical association of Au and W at reduced intrusion-related deposits, it can be suggested that the mantle source (including that in subduction-modified subcontinental mantle) was fertilized in W together with Au (cf. Chiaradia, 2003). These processes may lead to generation of the W-Au-fertile reduced magma source region in the metasomatized upper mantle, and remobilization of these sources during subsequent orogenic events that could produce Au-W-fertile ilmenite-series potassic magma.

During magmatic differentiation, the ilmenite-series igneous rocks of the Early Cretaceous plutonic suite, including granodiorite of the Central stock, evolve toward more fractionated varieties (monzogranite to granite-porphyry) with a higher Fe_2O_3/FeO ratio (Fig. 11). As noted by Smith et al. (2012), fractional crystallization during ascent or emplacement oxidizes magmas, as many liquidus minerals partition more ferrous than ferric iron; degassing of reduced volatile species (i.e., H_2, H_2S, and CH_4) can also increase oxidation state. This is consistent with the diversity of oxidation state of plutons at reduced intrusion-related Au and W deposits and the respective reduced to weakly oxidized parental plutonic suites (e.g., Hart et al. 2004; Mair et al. 2006, 2011; Yang et al. 2008). Advanced magmatic differentiation promoted enrichment of residual melt in W (Newberry and Swanson, 1986; Newberry, 1998; Rasmussen et al., 2011) and W+Au, the latter corresponding to most fractionated granite, with Au concentration in the residual felsic melt promoted by the low content of accessory oxides and sulfides and by elevated volatile content (cf. Mustard et al., 2006).

Notably, by the K, Na and Al_2O_3 contents, together with fO_2 variations, the Central stock is transitional between igneous rocks found at W-dominant and, on the other hand, Au-dominant reduced intrusion-related deposits (Fig. 11). In particular, the large reduced W-skarn (with no Au) deposits in Yukon-NWT are related to potassic peraluminous, ilmenite-dominant granitic rocks of the Tungsten Plutonic Suite (Maloof et al., 2001; Hart et al., 2004; Mair et al., 2006, 2011; Rasmussen et al., 2011). In contrast, the features of the Central stock such as elevated Na content, higher Fe_2O_3/(FeO+Fe_2O_3) ratio and lower Al_2O_3 content are similar to those of less potassic meta-aluminous to weakly peraluminous, moderately reduced titanite-dominant plutonic suites, which are parental for reduced intrusion-related Au deposits (e.g., the Mayo Plutonic Suite in Yukon; McCoy et al., 1997; Maloof et al., 2001; Hart et al., 2004; Hart, 2007; Mair et al., 2006, 2011). It appears that in plutonic suites causative for reduced W and Au deposits, a stronger enrichment in K is characteristic for dominantly W($\pm$Au) deposits, whereas more sodic rocks predominate at essentially Au ($\pm$W) deposits (e.g., Maloof et al., 2001; Mair et al., 2011).

The Vostok-2 deposit was formed during several hydrothermal stages beginning with prograde and retrograde skarns and followed by hydrosilicate and phyllic alteration assemblages. Petrologic features of the skarn and post-skarn assemblages are consistent with reduced W skarn deposits (Einaudi et al., 1981; Kwak and White, 1982) thus reflecting the features of the parental ilmenite-series plutonic suite. In particular, pyroxene absolutely predominates over garnet in prograde and retrograde skarn (Fig. 12A), and is represented by ferrous (hedenbergitic) varieties. The very minor garnet belongs to low-andraditic, essentially grossular (with elevated almandine-spessartine content) variety. Pyrrhotite is abundant in the skarn and postskarn assemblages, whereas magnetite is absent (Fig. 12A-B).

The rarity of molybdenite and low Mo content in scheelite are also consistent with reduced conditions. As noted by Candela and Bouton (1990) and Menganson et al. (2011), low fO_2 in the ilmenite-series magma generally favors high W/Mo ratio in related magmatic-hydrothermal systems, due to enhanced Mo partitioning into crystalline phases.

The hydrothermal stages were alternating with successive intrusion phases, the latter composing the Central stock and smaller stocks and dikes in its vicinity (Fig. 5). In particular, the skarns at Vostok-2 were formed before emplacement of the Central stock granodiorite and related intrusive breccia. This may be due to presence of an older and unexposed intrusive bodies (phases) possibly supplying fluids for the skarn formation. Formation of wollastonite in the prograde skarn at Vostok-2 requires presence of water-rich, very low-carbonic fluids (X_{CO2}=~0.005, or 0.5 mol.% CO_2) at temperatures 650-550°C and pressures exceeding 400 bar (Lentz and Suzuki, 2000). The temperature and pressure increase, as well as the addition of NaCl, shifts the stability of wollastonite to yet lower X_{CO2} (Heinrich, 1993). Exsolution of the aqueous NaCl-dominated magmatic-hydrothermal fluid at high temperature (~470-450°C) and pressure (1.1-1.2 kbar) continued also at the retrograde skarn stage, as indicated by the type 1 fluid inclusions and the stable isotope data (Fig. 13). The pressure at the retrograde skarn stage appears to be lower than the minimum pressures estimated at some other reduced W skarn deposits ranging from 1.7-2.0 kbar to 1.4-2.5 kbar (e.g., Sato, 1980; Guy et al., 1988; Gerstner et al., 1989). This may reflect shallower (~4.5-5 km) conditions of the retrograde skarn formation at Vostok-2 and is consistent with the porphyry features of the Central stock. This lower pressure, nevertheless, was sufficient to preclude phase separation in the high-temperature fluid released from the magma.

In contrast, the type 2A fluid inclusions in the hydrosilicate assemblage minerals formed after the emplacement of the Central stock granodiorite (~63-70 wt.% SiO_2) demonstrate the involvement of low-salinity highly-reduced, methane-dominated moderate-temperature (~350-380°C) fluids (Table 7). These fluids were followed by the lower temperature (300-350°C) non-carbonic but higher salinity (5.7-14.9 wt.% NaCl-equiv.) fluids (the type 2B fluid inclusions; Fig. 13), thus showing a typical pattern of fluid exsolution from crystallizing felsic magma, with a carbonic phase being released first due to its lower solubility than H_2O and Cl (e.g., Lowenstern, 2001; Baker, 2002). The lack of contemporaneous gaseous inclusions may indicate direct separation of these fluids from a crystallizing magma (e.g., Bodnar, 1995), and, similar to the retrograde skarn stage, once the fluid was released from the magma, the high pressure precluded phase separation.

Similar low-salinity, non-boiling methane-rich fluids were identified for hydrosilicate stage with massive scheelite deposition at some other reduced W skarn deposits (e.g., Mathieson and Clark, 1984; Gerstner et al., 1989). This is in contrast to the oxidized W-Mo and W-Mo-Cu skarn deposits with typical boiling of saline fluids producing

lower (moderate-grade) scheelite concentrations (e.g., Kwak, 1986). Thus, cooling of non-boiling low-salinity aqueous fluids reducing W-solubility combined with dissociation of Ca-bearing complexes liberating Ca (Rafal'sky et al., 1984) may have a generally predominating importance for intense scheelite deposition. The enrichment in Ca of the fluids was also recorded at other W skarn deposits (e.g., Kwak and Tan, 1981; Santarelli, 1988), and a magmatic source of Ca (cf. Soloviev, 2015) possibly reflecting the plutonic rock evolution toward those with less calcic plagioclase can be considered.

The phyllic stage fluids corresponded to more differentiated magmatic evolution evidenced by more felsic (~70-74 wt.% SiO_2) monzogranite- to granite-porphyry intrusions thus indicating W accumulation in evolving and crystallizing magma at reduced W deposits can occur at different stages of magmatic differentiation (cf. Rasmussen et al., 2011). During this stage, a generally similar (to the hydrosilicate stage) pattern of fluid evolution occurred, again with carbonic phase being released first. Consistently, the moderate-temperature (330-355^{o}C) carbonic type 3 inclusions are followed by the lower temperature (230-265^{o}C) more saline (6.6-12.0 wt.% NaCl-equiv.) non-carbonic aqueous type 4 inclusions (Fig. 13). The enrichment in CO_2 is a typical feature of the fluids at reduced intrusion-related Au deposits (e.g., McCoy et al., 1997; Baker, 2002; Baker and Lang, 2003) and of late fluids at reduced W skarn deposits (Fonteilles et al., 1989; Gerstner et al., 1989; Soloviev and Kryazhev, 2017). Notably the pressure of ~0.9 kbar at the phyllic stage is also similar to that of reduced intrusion-related Au deposits (e.g., McCoy et al., 1997; Baker, 2002). Together with the pressure of the retrograde skarn formation (~1.1-1.2 kbar), the latter being also lower than that at many reduced W skarn deposits, this may constitute a distinct feature of the Vostok-2 deposit formation, consistent with presence of both W skarns and Au mineralization related to a porphyry-style intrusive accompanied by intrusive and hydrothermal breccias.

The cooling and especially increasing pH due to boiling and related CO_2 removal (cf. Drummond and Ohmoto, 1985) were affecting W solubility at the phyllic stage that, together with dissociation of Ca-bearing complexes liberating Ca, promoted massive scheelite deposition (Rafal'sky et al., 1984; Wood and Samson, 2000). Notably no W chloride, fluoride, carbonate complexes, i.e., species commonly associated with high-salinity fluids, are required to form scheelite concentrations, as the role of hydrous W species dominates (Wood and Vlassopoulos, 1989; Wood and Samson, 2000). Probably, a strong role in W transport was also played by phosphate complexes (Manning and Henderson, 1984) evident by the association of scheelite and apatite. In contrast to W, partitioning of Au in magmatic-hydrothermal process is essentially influenced by the behavior of sulfur, with lower redox conditions promoting sulfide saturation in granitic magmas or facilitating sulfide (bearing Au) precipitation from mineralized

fluids (e.g., Lang and Baker, 2001; Yang, 2012). Consequently, various models of Au sequestration by magmatic sulfides in crystallizing late felsic magma, with further Au liberation, transport and deposition by hydrothermal fluids can be considered, as well as triggering of sulfide saturation, together with CO_2 release, due to mixing of felsic and mafic magmas (the latter producing the late mafic dikes) (e.g., Yang, 2012). The fO_2-pH conditions of the fluids evolved from arsenopyrite and pyrrhotite stability fields, and the lower fO_2 part of chalcopyrite stability field, toward the CH_4/CO_2 and native Bi/bismuthinite transitions and pyrite stability field, where Au transport and precipitation are most feasible (Fig. 12C). Notably Au transport at low temperatures corresponding to phyllic stage (typical for reduced intrusion-related Au deposits) occurs mostly in the form of bisulfide rather than chloride complexes (e.g., Gammons and Williams-Jones, 1997). Close association of Au and Bi also supports their joint transport and precipitation as bisulfide complexes due to low fO_2 and low salinity (low chloride content) of the fluids (e.g., Seward, 1991; cf. Baker, 2002), or partial scavenging of Au in Bi melt coexisting with the hydrothermal fluid (e.g., Tooth et al., 2008; Palmer et al., 2013). Gold deposition could have also been favored by a decreasing Au solubility under a pH decrease that occurred after massive scheelite deposition, the latter was favored by fluid boiling and coincident pH increase at the intermediate phyllic stage. Remarkably, the fO_2-fS_2-pH stability field of Mo-free scheelite overlaps that of Au, and scheelite is locally substituted by wolframite at lower pH (Fig. 12C). Cooling of non-boiling fluids favoured joint deposition of scheelite, Bi and Au; this was possible due to the joint availability of these metals in the magmatic-hydrothermal fluids.

The $\delta^{18}O_{H2O}$ values (+8.3 to +8.8 ‰) obtained for the retrograde skarn and hydrosilicate stage hydrothermal fluids closely correspond to those determined by Gvozdev (2007) for the intrusive rocks ($\delta^{18}O$ = +7.9 to +9.5‰), suggesting a magmatic source of water (Taylor, 1979), and the uniformity of the values suggests a homogenized character of the source, with lack of meteoric water incursion at the level of mineralization. These values also indicate a homogenized mixed mantle-crustal oxygen source (Faure, 1986). A sedimentary source of sulfur ($\delta^{34}S$ = -6.9 to -6.2 ‰) can be also suggested (Ohmoto and Goldhaber, 1997; Seal, 2006). The carbon isotope data ($\delta^{13}C_{fluid}$ = -20.1 to -14.9 ‰) suggest a a dominating reduced organic carbon source (i.e., sedimentary or metamorphic rocks, with the mean $\delta^{13}C$ = ~25 ‰; Hoefs, 1997) evolving toward a magmatic (mantle- to crustal-derived, with the mean $\delta^{13}C$ = ~5±2 ‰; Hoefs, 1997; Ohmoto and Rye 1979; Ohmoto and Goldhaber, 1997) source of carbon at the hydrosilicate stage; this is consistent with the proportion of sedimentary/mantle material (~50:50%; Krymsky et al., 1998) in the melts producing the Central stock. Similar to the hydrosilicate stage, the oxygen stable isotope data suggest a

magmatic source of water ($\delta^{18}O$ = +8.6 to +9.2‰) but, in contrast to the hydrosilicate stage, less homogenous sedimentary source of sulfur ($\delta^{34}S$ = -9.3 to -4.1‰), together with more distinctly magmatic (mantle- to crustal-derived) source of carbon ($\delta^{13}C_{fluid}$ = -6.9 to -5.2‰) in fluids formed the early phyllic mineral assemblage. The enrichment in heavy carbon isotope may reflect a partial fluid sourcing from felsic magma that produced monzogranite- to granite-porphyry immediately pre-dating the phyllic stage, or influence of mafic magma reservoir producing late mafic dikes post-dating the phyllic stage (cf. Rasmussen et al., 2011). However, the role of sedimentary carbon has again increased toward the intermediate ($\delta^{13}C_{fluid}$ = -16.4 to -14.5 ‰) and late ($\delta^{13}C_{fluid}$ = -16.3 to -14.7 ‰) phyllic mineral assemblages.

An involvement of typically homogenous but mixed magmatic (mantle- to crust-derived) and sedimentary sources, with a great role of sedimentary sulfur and carbon (e.g., Bowman et al., 1985; Yuvan, 2006; Soloviev and Kryazhev, 2017), appears to be a distinct feature of reduced W skarn deposits. Similarly, a homogenized mantle-crust magmatic source is typical for fluid species such as sulfur ($\delta^{34}S$ = 0±5 ‰; Fornadel, 2010) at reduced intrusion-related Au deposits, with local fluctuations likely related to an involvement of sedimentary sulfur (Goldfarb et al., 2004; Nutt and Hofstra, 2007) and other interaction with the host rocks (e.g., Marsh et al.,2003; Mair et al., 2006). In contrast, the role of mantle-derived fluid species is more consistent at oxidized W-Mo-Cu+Au deposits and related magnetite-series granitoids (e.g., Zaw and Singoyi, 2000; Ishihara and Sasaki, 1989, 2002). This may in part reflect a greater mantle-crust interaction in the late- to post-collisional tectonic environment, with the development of larger, longer crystallizing crustal intermediate to felsic magma chambers. This favors a greater involvement and homogenization of the crustal (including sedimentary) material, with protracted magmatic evolution advancing magmatic differentiation, the latter in turn facilitating more complete partitioning of W (and Au) into magmatic-hydrothermal fluid and producing typically larger reduced W±Au deposits. Alternatively, whereas W mineralization at Vostok-2 was related to a mixed mantle-crustal magmatic source, the Au-Bi-bearing fluids could have been sourced from a more distinctly mantle-related magmatic reservoir (e.g., Keith et al., 1997; Halter et al., 2005).

Conclusions

The Vostok-2 deposit is situated in a metallogenic belt of W, Sn-W, Au, and Au-W deposits formed in a collisional tectonic environment after cessation of active subduction. The deposit is associated with a mantle-related ilmenite-series plutonic suite and, besides large W-Cu skarns of the reduced type, incorporates quartz stockworks with significant reduced Au (+W, Bi, As) mineralization thus complementing the class of reduced intrusion-related

Au±W deposits. The deposit is related to a high-K calc-alkaline, peraluminous plutonic suite that, by its petrological features, is transitional between those producing reduced W skarn deposits, and those producing reduced Au deposits. Intense mantle-crust interaction, with the development of crustal felsic magmatic chambers and further magmatic differentiation, was accompanied by magmatic intrusions in the upper crust levels and the respective releases of magmatic-hydrothermal fluids from crystallizing magma. This caused alternation of magmatic intrusions and hydrothermal stages. The retrograde skarn formation occurred at lower pressure (1.1-1.2 kbar) than that at many reduced W skarn deposits; on the other hand, this pressure, as well as the phyllic stage pressure (~0.9 kbar), is comparable to that at reduced intrusion-related Au deposits. Thus, these transitional pressure (i.e. formation depth) conditions, together with transitional petrologic features (i.e. magmatic source region) of the productive plutonic suite, may have contributed to the superposition of W and Au mineralization. The respective hydrothermal fluid evolution included an early release of hot moderately-saline aqueous fluids of the skarn stage, followed by lower-temperature cyclic releases of high-carbonic to low- and moderate-salinity aqueous fluids, with the cycles following progressively more felsic magmatic intrusions and corresponding to the hydrosilicate (with CH_4 dominating among carbonic species) and phyllic (CO_2-dominated) alteration stages. The stable isotope data support a magmatic source of oxygen ($\delta^{18}O_{H2O}$ = +9.3 to +7.2 ‰) and a dominantly crustal source of sulfur ($\delta^{34}S$ = -9.5 to -4.1 ‰) in the hydrothermal fluids, with varying sedimentary to magmatic (mantle- to crustal-derived) source of carbon ($\delta^{13}C_{fluid}$ = -20.1 - -14.9 ‰ to -6.9 - -5.2 ‰). Magmatic differentiation toward more felsic compositions was responsible for the fluid enrichment in W (±Au), although Au and Bi could also have been sourced from mafic magma. Decreasing temperatures, together with elevated Ca content in the non-boiling fluids, promoted scheelite deposition at the early hydrothermal stages. The most intense scheelite deposition at the phyllic stage was caused by CO_2 removal due to boiling of CO_2-rich fluids; further cooling of the non-boiling fluids favoured joint deposition of scheelite, Bi and Au, the latter occurred under the joint availability of W and Au in the magmatic-hydrothermal fluid.

Acknowledgments

This paper represents part of the authors' work on research and assessment of W, Au and other deposits in the CIS countries. We thank V.S. Kudrin, T.I. Getmanskaya, V.M. Borodanov, A.M. Materikova, and V.I.Gvozdev for fruitful discussions. Reviews by David Lentz and Tim Baker significantly improved the initial version of the manuscript. Editorial reviews by Franco Pirajno and an anonymous OGR reviewer significantly improved the paper.

REFERENCES

Atkinson, A.B., 2002, A model for the PTX properties of H_2O-NaCl: M.Sc.Thesis, Virginia Tech. Institute and State University, 126 p.

Baker, T., 2002, Emplacement depth and carbon dioxide-rich fluid inclusions in intrusion-related gold deposits: Economic Geology, v. 97, p. 1111–1117.

Baker, T., and Lang, J.R., 2003, Reconciling fluid inclusion types, fluid processes, and fluid sources in skarns: an example from the Bismarck deposit, Mexico: Mineralium Deposita, v. 38, p. 474-495.

Baker T., Pollard P.J., Mustard R., Mark G., and Graham J.L., 2005, A comparison of granite-related tin, tungsten, and gold-bismuth deposits: implications for exploration: SEG Newsletter, v. 61, p. 5-17.

Bakker, R. J., 2003, Package FLUIDS 1. Computer programs for analysis of fluid inclusions data and for modeling bulk fluid properties: Chemical Geology, v. 194, p. 3-23.

Becker, S.P., Fall, A., and Bodnar, R.J., 2008, Synthetic fluid inclusions. XVII. PVTX properties of high-salinity H_2O-NaCl solutions (>30 wt.% NaCl): applications to fluid inclusions that homogenize by halite disappearance from porphyry copper and other hydrothermal ore deposits: Economic Geology, v. 103, p. 539-544.

Belyansky, G.S., Rybalko, V.I., Syasko, A.A., Bazhanov, V.A., Uglova, N.I., Abramova, V.A., Oleinikov, A.B., Kovalenko, S.V., Kashtaev, B.I., Alenicheva, A.A., and Gonokhova, N.G., 2011, Explanatory notes to the geological map of Russia, L-52/53, and K-52/53 map sheets, 1:1,000,000 scale, 3rd generation. VSEGEI, St-Petersburg. 699 p. (in Russian)

Benning, L.G., and Seward, T.M., 1996, Hydrosulfide complexing of Au(I) in hydrothermal solutions from 150-400°C and 500-1500 bar: Geochimica et Cosmochimica Acta., v. 60, p. 1849–1871.

Bodnar, R.J., 1995, Fluid inclusion evidence for a magmatic source for metals in porphyry copper deposits: in Thompson, J.F.H., ed.: Magmas, fluids, and ore deposits. Min. Assoc. Canada Short Course Series, v. 23, p. 139-152.

Bodnar, R.J., and Vityk, M.O., 1995, Interpretation of microthermometric data for H_2O-NaCl fluid inclusions: in De Vivo, B., and Frezzotti, M.L., eds, Fluid inclusions in minerals, methods and applications, Blacksburg, Virginia Tech, p. 117-130.

Bottrell, S.H., Yardley, B.D.W., and Buckley, F., 1988, A modified crush-leach method for the analysis of fluid inclusion electrolytes: Bulletin de Minéralogie, v. 111, p. 279-290.

Bowman, J.R., Covert, J.J., Clark, A.H., and Mathieson, G.A., 1985, The Cantung E-Zone scheelite skarn orebody, Tungsten, Northwestern Territories: oxygen, hydrogen and carbon isotope studies: Economic Geology, v. 80, p. 1872-1895.

Burruss, R.C., 1981, Analysis of phase equilibria in C-O-H-S fluid inclusions: in Hollister, L.S., and Crawford, M.L., eds., Fluid inclusions: Application to Petrology: Miner. Assoc. of Canada Short Course Handbook: v. 6, p. 39-74.

Candela, P.A., 1997, A review of shallow, ore-related granites: textures, volatiles, and ore metals: Jour. Petrol., v. 38, p. 1619-1633.

Candela, P.A., and Boulton, S.L., 1990, The influence of oxygen fugacity on tungsten and molybdenum partitioning between silicate melts and ilmenite: Economic Geology, v. 85, p. 633-640.

Chiaradia, M., 2003, The evolution of tungsten sources in crustal mineralization from Archaean to Tertiary inferred from lead isotopes: Economic Geology, v. 98, p. 1039-1045.

Clayton, R.N., and Mayeda, T.K., 1963, The use of bromine pentafluoride in the extraction of oxygen from oxides and silicates for isotopic analysis: Geochem. Cosmochim. Acta, v. 27, p. 43-52.

Crawford, M.L., 1981, Phase equilibria in aqueous fluid inclusions: in Hollister, L.S., and Crawford, M.L., eds., Fluid inclusions: Application to Petrology: Miner. Assoc. of Canada Short Course Handbook: v. 6, p. 75-100.

Darling, R.S., 1991, An extended equation to calculate NaCl contents from final clathrate melting temperatures in H_2O-CO_2-NaCl fluid inclusions: implications for PT-isochors location: Geochim. Cosmochim. Acta, v. 55, p. 3869-3871.

Dick, L.A., and Hodgson, C.J., 1982, The MacTung W-Cu(Zn) contact metasomatic and related deposits of the North-eastern Canadian Cordillera: Economic Geology, v. 77, p. 845-867.

Drabek, M., 1984, The influence of the fugacity of oxygen and sulfur on the stability of some geologically significant phases and associations of the Fe-Mo-W-S-O system: Bulletin of the Geol. Survey, Prague, v. 59 (4), p. 193-200.

Drummond, S.E., and Ohmoto, H., 1985, Chemical evolution and mineral deposition in boiling hydrothermal systems: Economic Geology, v. 80, p. 126-147.

Einaudi, M.T., Meinert, L.D., and Newberry, R.J., 1981, Skarn deposits: Economic Geology, 75th Anniv.Vol., p. 317-391.

Faure, G., 1986, Principles of Isotope Geology. 2nd edn. John Wiley & Sons Inc., New York. 608 p.

Fonteilles M., Soler P., Demange M., Derre, C., Krier-Schellen, A.D., Verkaeren, J., Guy, B., and Zahm, A., 1989, The scheelite skarn deposit of Salau (Ariege, French Pyrenees): Economic Geology, v. 84, p. 1172-1209.

Fornadel, A.P., 2010, Mineralogical, petrological, stable isotope, and fluid inclusion studies of the Palea Kavala reduced intrusion-related and the transitional Fakos porphyry Cu-Mo to epithermal Au-Te ore systems: M.Sc.Thesis, Iowa State University, 181 p.

Fournier, R.O., 1999, Hydrothermal process related to movement of fluid from plastic into brittle rock in the magmatic-epithermal environment: Economic Geology, v. 94, p. 1193-1212.

Gammons, C.H., and Williams-Jones, A.E., 1997, Chemical mobility of gold in the porphyry-epithermal environment: Economic Geology, v. 92, p. 45-59.

Gerasimov, N.S., Khetchikov, L.N., Govorov, I.N., and Gvozdev, V.I., 1994, Rubidium-strontium isochrones for granitoids of the Dalnensky suite of the Central Sikhote-Alin and their petrogenetic interpretation: Proceedings of the Russian Science Academy, Earth Sciences, v. 334 (4), p. 473-475. (in Russian)

Gerstner, M.R., Bowman, J.R., and Pasteris, J.D., 1989, Skarn formation at the McMillan Pass tungsten deposit (MacTung), Yukon and Northwest territories. 1. P-T-X-V characterization of the methane-bearing, skarn-forming fluids: Can. Mineralogist, v. 27, p. 545-563.

Goldfarb, R.J., Ayuso, R., Miller, M.L., Ebert, S.W., Marsh, E. E., Petsel, S. A., Miller, L.D., Bradley, D., Johnson, C., and McClelland, W., 2004, The Late Cretaceous Donlin Creek gold deposit, Southwestern Alaska: controls on epizonal ore formation: Economic Geology, v. 99, p. 643-671.

Goldstein, R. H., and Reynolds, T. J., 1994, Systematics of fluid inclusions in diagenetic minerals: Society for Sedimentary Geology Short Course 31, 199 p.

Gonevchuk, V.G., Gonevchuk, G.A., Korostelev, P.G., Semenyak, B.I., and Seltmann, R., 2010, Tin deposits of the Sikhote-Alin and adjacent areas (Russian Far East) and their magmatic association: Austral. J. Earth Sciences, v. 57, p. 777-802.

Gustafson, W.I., 1974, The stability of andradite, hedenbergite, and related minerals in the system Ca-Fe-Si-O-H: Journal of Petrology, v. 15, p. 455-496.

Guy B., Faure N., Le Loch G., and Varenne J.-L., 1988, Etude microtermometrique des inclusions fluids des skarns a tungstene de Costabonne (Pyrenees, France): quelques resultants: C.R. Acad. Sci., Serie II, t. 307, p. 33-38.

Gvozdev, V.I., 2006, The Vostok-2 and Lermontovskoe deposits: in The Large and Superlarge Ore Deposits. Moscow: IGEM RAN Publishing, v. 3, p. 627-667. (in Russian)

Gvozdev, V.I., 2007, Ore-magmatic systems of scheelite-sulfide skarn deposits in the East of Russia: Sci. D. Thesis, Vladivostok: Far East Geol. Inst., 54 p. (in Russian)

Gvozdev, V.I. and Tsepin, A.I., 2005, Bismuth mineralization in the ores of the Vostok-2 deposit (Primorye Region, Russia): Geology of Ore Deposits, v. 47, p. 132-145.

Halter, W.E., Heinrich, C.E., and Pettke, T., 2005, Magma evolution and the formation of porphyry Cu–Au ore fluids: evidence from silicate and sulfide melt inclusions: Mineralium Deposita, v. 39, p. 845-863.

Hart, C.J.R., 2007, Reduced intrusion-related gold systems: in Goodfellow, W.D., ed., Mineral Deposits of Canada: A Synthesis of Major Deposit Types, District Metallogeny, the Evolution of Geological Provinces, and Exploration Methods: Geological Association of Canada, Mineral Deposits Division, Special Publication no. 5, p. 95-112.

Hart, C.J.R., Mair, J.L., Goldfarb, R.J., and Groves, D.I., 2004, Source and redox controls on metallogenic variations in intrusion-related ore systems, Tombstone Tungsten Belt, Yukon Territory, Canada: Trans Roy. Soc. Edinburgh, Earth Sciences, v. 95, p. 339-356.

Hedenquist, J.W., Arribas, A., and Reynolds, T.J., 1998, Evolution of an intrusion-centered hydrothermal system: Far Southeast-Lepanto porphyry and epithermal Cu-Au deposits, Philippines: Economic Geology, v. 93, p. 373-404.

Heinrich, W., 1993, Fluid infiltration through metachert layers at the contact aureole of the Bufa del Diente intrusion, northeast Mexico: implications for wollastonite formation and fluid immiscibility: Amer. Miner., v. 78, p. 804-818.

Henley, R.W., 1984, Solubility of gold in hydrothermal chloride solutions: Chem. Geol., v. 11, p. 73-87.

Hoefs, J., 1997, Stable isotope geochemistry. 4th edn. Springer-Verlag, Berlin-Heidelberg-New York, 201 p.

Hronsky, J.M.A., Groves, D.I., Loucks, R.R., and Begg, G.C., 2012, A unified model for gold mineralisation in accretionary orogens and implications for regional-scale exploration targeting methods: Mineralium Deposita, v. 47, p. 339-358.

Ishihara, S., 1981, The granitoid series and mineralization, Economic Geology, v. 75, p. 458-484.

Ishihara, S., 2004, The redox state of granitoids relative to tectonic setting and earth history: the magnetite-ilmenite series 30 years after: GSA Spec. Paper, v.389, p23-33.

Ishihara, S., Hua, R., Hoshino, M. and Murakami, H., 2008, REE abundance and REE minerals in granitic rocks in the Nanling Range, Jiangxi Province, southern China, and generation of the REE-rich weathered crust deposits: Resource Geology, v. 58(4), p. 355-372.

Ishihara, S., and Sasaki, A., 1989, Sulfur isotopic ratios of the magnetite-series and ilmenite-series granitoids of the Sierra Nevada batholith - a reconnaissance study: Geology, v. 17, p. 788-791.

Ishihara, S., and Sasaki, A., 2002, Paired sulfur isotopic belts: Late Cretaceous-Paleogene ore deposits of Southwest Japan: Bull. Geol. Surv. Japan, v. 53(5/6), p. 461-477.

Izosov, L.A., Vasilenko, N.G., Mel'nikov, N.G., and Petrishchevsky, A.M., 1988, Tungsten-bearing olistostrome of the Central Sikhote-Alin: Geotektonika, v. 22, p. 76-87. (in Russian)

Jahn, B.M., Valui, G., Kruk, N., Gonevchuk, V., Masako, U., and Wu, J.T.J., 2015, Emplacement ages, geochemical, and Sr-Nd-Hf isotopic characterization of Mesozoic to Early Cenozoic granitoids of the Sikhote-Alin orogenic belt, Russian Far East: crustal growth and regional tectonic evolution: Journal of Asian Earth Sciences, v. 111, p. 872-918.

Johnson, J.W., Oelkers, E.H., and Helgeson, H.C., 1992, SUPCRT-92: software package for calculating the standard molar thermodynamic properties of minerals, gases, aqueous species and reactions from 1 to 5000 bars and 0 to 1000^{o}C: Computer and Geosciences, v. 18, p. 1-65.

Keith, J.D., Whitney, J.A., Hattori, K., Ballantyne, G.H., Christiansen, E.H., Barr, D.L., Cannan, T.M., and Hook, C.J., 1997, The role of magmatic sulfides and mafic alkaline magmas in the Bingham and Tintic mining districts, Utah: Journal of Petrology, v. 38, p. 1679-1690.

Kendrick, M.A., Honda, M., Walshe, J., and Petersen, K., 2011, Fluid sources and the role of abiogenic-CH_4 in Archean gold mineralization: constraints from noble gases and halogens: Precambrian Research, v. 189, p. 313-327.

Khanchuk, A.I., 2000, Paleogeodynamic analysis of the formation of ore deposits in the Russian Far East: in Ore Deposits of Continental Margins, Vladivostok: Dal'nauka Publishing, p. 5-34. (in Russian)

Khanchuk, A.I., Golozubov, V.V., Martinov, Yu.A., and Simanenko, V.P., 1997, The Early Cretaceous and Paleogene transform continental margins (Californian type) of the Russian Far East: in Tectonics of Asia, Moscow, GEOS Publishing, p. 240-243. (in Russian)

Khanchuk, A.I., Kemkin, I.V., and Kruk, N.N., 2016, The Sikhote-Alin orogenic belt, Russian South East: terranes and the formation of continental lithosphere based on geological and isotopic data. Jour. Asian Earth Sciences, v.120, p.117-138.

Khetchikov, L.N., Pakhomova, V.A., Gvozdev, V.I., and Zhuravlev, D.Z., 1999, Age of mineralization and some genetic features of the Vostok-2 scheelite-sulfide skarn deposit in the Central Sikhote-Alin: Ores and Metals, no. 2, p. 30-36. (in Russian)

Kovalenko, V.I., Rub, M.G., Osipov, M.A., Gladkov, N.G., Efremova, S.V., Koval., P.V., Rub, A.K., Ryazantseva, M.D., Sherkhan, O., Yakimov, V.M., and Yarmolyuk, V.V., 1988, The Ore Potential of Igneous Associations, Moscow: Nauka Publishing, 231 p. (in Russian)

Kruk, N.N., Simanenko, V.P., Gvozdev, V.I., Golozubov, V.V., Kovach, V.P., Serov, P.A., Moskalenko, E.Yu., and Kuibida, M.L., 2014, Geochemical characteristics and sources of the melts of the Early Cretaceous granitoids in the Samarga terrain (Sikhote-Alin): Russian Geology and Geophysics, no. 2, p. 276-302.

Krymsky, P.Sh., Pavlov, V.A., Rub, M.G., Belyatsky, B.V., and Levsky, L.K., 1998, The Rb-Sr and Sm-Nd isotopic characteristics of granitoids and ores at the Vostok-2 scheelite deposit, Primorie: Petrology, no.6, p.3-15.

Kudrin, A.V., 1986, The solubility of tugarinovite MoO_2 in aqueous solutions at elevated temperatures: Geochem. Internat., v. 23, p. 126-138.

Kudrin, A.V., 1989, Behavior of Mo in aqueous NaCl and KCl solutions at 300-450°C: Geochem. Internat., v. 26, p. 87-99.

Kudrin, V.S., Kudrina, M.A., Silaev, A.E., and Borodanov, V.M., 1979, Assessment of the new skarn scheelite occurrences adjacent to the Vostok-2 and Lermontovskoe deposits, and mineral composition of ores at deep levels of the Vostok-2 deposit: Unpubl. Prof. Report. Moscow, VIMS. 453 p. (in Russian)

Kwak, T.A.P., 1986, Fluid inclusions in skarns (carbonate replacement deposits): Jour. Metamorphic Geology, v. 4, p. 363-368.

Kwak, T.A.P., and White, A.J.R., 1982, Contrasting W-Cu-Mo and W-Sn-F skarn types and related granitoids: Mining Geology, v. 32, p. 339-351.

Lang J.R., and Baker T., 2001, Intrusion-related gold systems: the present level of understanding: Mineralium Deposita, v. 36, p. 477-489.

Lentz, D.R., and Suzuki, K., 2000, A low F pegmatite-related skarn from the southwestern Grenville Province, Ontario, Canada: phase equilibria and petrogenetic implications: Economic Geology, v. 95, p. 1319-1337.

Le Maitre, R.W., Streckeisen, A., Zanettin, B., Le Bas, M.J., Bonin, B., Bateman, P., Bellieni, G., Dudek, A., Efremova, S., Keller, J., Lameyre, J., Sabine, P.A., Schmid, R., Sorensen, H., and Woolley, A.R., 2002, Igneous Rocks: A Classification and Glossary of Terms (2nd ed.): Cambridge University Press, 236 p.

Lowenstern, J.B., 2001, Carbon dioxide in magmas and implications for hydrothermal systems: Mineralium Deposita, v. 36, p. 490-502.

Mair, J.L, Goldfarb, R.J., Johnson, C.A., Hart, C.J.R., and Marsh, E.E., 2006, Geochemical constraints on the genesis of the Scheelite Dome intrusion-related gold deposit, Tombstone gold belt, Yukon, Canada: Economic Geology, v. 101, p. 523-553.

Mair J.L., Farmer G.L., Groves D.I., Hart C.J.R., and Goldfarb R.J., 2011, Petrogenesis of mid-Cretaceous post-collisional magmatism at Scheelite Dome, Yukon, Canada: evidence for a lithospheric mantle source for intrusion-related gold systems: Economic Geology, v. 106, p. 451-480.

Maloof, T.L., Baker, T., and Thompson, J.F.N., 2001, The Dublin Gulch intrusion-related gold deposit, Tombstone Plutonic Suite, Yukon Territory, Canada: Miner. Deposita, v. 36, p. 583-593.

Maniar, P.D., and Piccoli, P.M., 1989, Tectonic discrimination of granitoids: Geol. Soc. America Bulletin, v. 101, p. 635-643.

Manning, D.A.C., and Henderson, P., 1984, The behavior of tungsten in granitic melt-vapor systems: Contrib. Mineral. Petrol., v. 86, p. 286-293.

Marsh, E. E., Goldfarb, R.J., Hart, C.J.R., and Johnson, C.A., 2003, Geology and geochemistry of the Clear Creek reduced intrusion-related gold occurrences, Tintina Gold Province, Yukon, Canada: Canadian Journal of Earth Science, v. 40, p. 681-699.

Masterman, G.J., Cooke, D.R., Berry, R.F., Walshe, J.L., Lee, A.W., and Clark, A.H., 2005, Fluid chemistry, structural setting, and emplacement history of the Rosario Cu-Mo porphyry and Cu-Ag-Au epithermal veins, Collahuasi District, Northern Chile: Economic Geology, v. 100, p. 835-862.

Mathieson, G.A., and Clark, A.H., 1984, The CanTung E-Zone scheelite skarn orebody, Tungsten, Northwest Territories: a revised genetic model: Economic Geology, v. 79, p. 883-901.

McCoy, D., Newberry, R.J., Layer, P., DiMarchi, J.J., Bakke, A., Masterman, J.S., and Minehane, D.L., 1997, Plutonic-related gold deposits of Interior Alaska: Economic Geology Monograph 9, p.191-241.

McCrea, J.M., 1950, On the isotopic chemistry of carbonates and a paleotemperature scale: J. Chem. Phys., v. 18, p. 849-857.

Menganson, M.J., Candela, P.A., and Piccoli, P.M., 2011, Molybdenum, tungsten and manganese partitioning in the system pyrrhotite-Fe-S-O melt-rhyolite melt: impact of sulfide segregation on arc magma evolution: Geochim. Cosmochim. Acta, v. 75, p. 7018-7030.

Meinert, L.D., 1995, Compositional variations of igneous rocks associated with skarn deposits – chemical evidence for a genetic connection between petrogenesis and mineralization: in Thompson, J.F.H., ed.: Magmas, fluids, and ore deposits. Min. Assoc. Canada Short Course Series, v. 23, p. 401-418.

Meinert, L.D., Hedenquist, J.W., Saton, H., and Matsuhisa, Y., 2003, Formation of anhydrous and hydrous skarns in Cu-Au ore deposits by magmatic fluids: Economic Geology, v. 98, p. 147-156.

Middlemost, E.A.K., 1997, Magmas, Rocks and Planetary Development. Longman, Harlow, 299 p.

Mlynarczyk, M.S.J., and Williams-Jones, A.E., 2005, The role of collisional tectonics in the metallogeny of the Central Andean tin belt: Earth Planet. Sci. Letters, v. 240, p. 656-667.

Muller, D., and Groves, D.I., 2016, Potassic igneous rocks and associated gold-copper mineralization: Heidelberg-New York-Dordrecht-London, Springer Publishing, 4th ed., 311 p.

Mustard, R., Ulrich, T., Kamenetsky, V.S., and Mernagh, T., 2006, Gold and metal enrichment in natural granitic melts during fractional crystallization: Geology, v. 34, p. 85-88.

Naumov, G.B., Ryzhenko, B.N., and Khodakovskiy, I.L., 1971, Handbook of thermodynamic data: Moscow, Atomizdat, 326 p. (in Russian)

Newberry R.J., 1998, W- and Sn-skarn deposits: a 1998 status report: in Lentz, D.R., ed., Mineralized intrusion-related skarn systems. Miner. Assoc. Can. Short Course Series, p. 289-335.

Newberry R.J., and Swanson S.E., 1986, Scheelite skarn granitoids: an evaluation of the roles of magmatic source and process: Ore Geology Review, v. 1, p. 57-81.

Nutt, C.J., and Hofstra, A.H., 2007, Bald Mountain gold mining district, Nevada: A Jurassic reduced intrusion-related gold system: Economic Geology, v. 102, p. 1129-1155.

Ohmoto, H., and Goldhaber, M.B., 1997, Sulfur and carbon isotopes: in Barnes, H.L., ed., Geochemistry of Hydrothermal Ore Deposits, 3rd ed. John Wiley and Sons, New York, p. 517-611.

Ohmoto, H., and Rye, R.O., 1979, Isotopes of sulfur and carbon: in Barnes, H.L., ed., Geochemistry of Hydrothermal Ore Deposits, 2nd ed. Wiley, New York, p. 509-567.

Palmer, E.M., McFarlane, C.R.M., Lentz, D.R., and Falck, H., 2013, Gold in the Cantung W-skarn deposit, Northwest Territories: distribution, mineralogy, and paragenesis: Atlantic Geology, v.49, p.174-175.

Pearce, J., 1996, Sources and settings of granitic rocks: Episodes, v. 19, p. 120-125.

Potter, R.W., 1977, Pressure corrections for fluid-inclusion homogenization temperatures based on volumetric properties of the system NaCl-H_2O: U.S. Geol. Survey Journal of Research, v. 5, p. 603-607.

Rafal'sky, R.P., Bryzgalin, O.V., and Fedorov, P.L., 1984, Tungsten migration and scheelite deposition under hydrothermal conditions: Geochem. International, v. 21, p. 1-13.

Rasmussen, K.L., Lentz, D.R., Falck, H., and Pattison, D.R.M., 2011, Felsic magmatic phases and the role of late-stage aplitic dikes in the formation of the world-class CanTung tungsten skarn deposit, Northwest Territories, Canada: Ore Geology Reviews, v.41, p.75-111.

Robinson, B.W., and Kusakabe, M., 1975, Quantitative preparation of sulfur dioxide, for $^{34}S/^{32}S$ analyses, from sulfides by combustion with cuprous oxide: Anal. Chem., v. 47, p. 1179-1181.

Roedder, E., 1984, Fluid inclusions in minerals: Reviews in Mineralogy, v. 12, 644 p.

Rub, M.G., Pavlov, V.A., Gladkov, N.G., and Yashukhin, O.I., 1982, Tin- and tungsten-bearing granitoids in some regions of the USSR. Moscow: Nauka Publishing, 261 p. (in Russian)

Santarelli, F., Alderton, D., and Guy, B., 1998, Etude des fluids des skarns a tungstene de Costabonne (Pyrenees); analyses chemiques, mineraux fils: quelques resultats: C.R. Acad. Sci., Serie II, v. 307, p. 1231-1236.

Sato, K., 1980, Tungsten skarn deposit of the Fujigatani mine, Southwest Japan: Economic Geology, v. 75, p. 1066-1082.

Schmidt, C., and Bodnar, R.J., 2000, Synthetic fluid inclusions: XVI. PVTX properties in the system H_2O-NaCl-CO_2 at elevated temperatures, pressures, and salinities: Geochim. Cosmochim. Acta, v. 64, p. 3853-3869.

Seal, R.R., 2006, Sulfur isotope geochemistry of sulfide minerals: Review Mineral. Geochem., v.61, p.633-677.

Selby, D., Nesbitt, B.E., and Muehlenbachs, K., 2000, Hydrothermal alteration and fluid chemistry of the Endako porphyry molybdenum deposit, British Columbia: Economic Geology, v. 95, p. 183-202

Seward, T.M., 1991, The hydrothermal geochemistry of gold: in Foster, R.P., ed., Gold Metallogeny and Exploration: Glasgow, Blackies, p. 165-209.

Smith, S.M., Canil, D., Rowins, S.M., and Friedman, R., 2012, Reduced granitic magmas in an arc setting: The Catface porphyry Cu–Mo deposit of the Paleogene Cascade Arc: Lithos, v. 154, p. 361-373.

Soloviev, S.G., 2008, Metallogeny of Phanerozoic tungsten skarn deposits: Scientific World Publishing, Moscow, 368 p. (in Russian)

Soloviev, S.G., 2014, The metallogeny of shoshonitic magmatism. Moscow: Scientific World Publishing. V. 1. 528 p. V. 2. 472 p. (in Russian)

Soloviev, S.G., 2015, Geology, mineralization, and fluid inclusion characteristics of the Kumbel oxidized W-Cu-Mo skarn and Au-W stockwork deposit, Tien-Shan, Kyrgyzstan: Mineralium Deposita, v. 50, p.187-220.

Soloviev, S.G., and Krivoschekov, N.N., 2011, The Vostok-2 gold-base metal-tungsten skarn deposit, Central Sikhote-Alin, Russia: Geology of Ore Deposits, no. 6, p. 543-568.

Soloviev, S.G., and Kryazhev, S.G., 2017, Geology, mineralization, and fluid inclusion characteristics of the Skrytoe reduced-type W skarn and stockwork deposit, Sikhote-Alin, Russia. Mineralium Deposita, v. 52 doi 10.1007/s00126-016-0705-1

Stepanov, G.N., 1977, Mineralogy, petrography and genesis of scheelite-sulfide skarn deposits. Moscow: Nauka Publishing, 178 p. (in Russian)

Stepanov, G.N., and Gvozdev, V.I., 1987, Mineralogy and geochemistry of minor components in the ores from scheelite skarn deposits in the Far East: in New Data on Mineralogy of the Far East, Vladivostok, p. 49-55. (in Russian)

Taylor, H.P., 1979, Oxygen and hydrogen isotopes in hydrothermal ore deposits. In: Barnes, H.L. (ed.) Geochemistry of hydrothermal ore deposits, 2nd edn. Wiley, New York, pp. 236-277.

Thiery, R., Kerkhof, A.M, and Dubessy, J., 1994, vX properties of CH_4-CO_2 and CO_2-N_2 fluid inclusions: modeling for T < 31 ºC and P < 400 bars: Europ. J. Mineral., no. 6, p. 753-771.

Thompson, J.F.H., Sillitoe, R.H., Baker, T., Lang, J.R., and Mortensen, J.K., 1999, Intrusion-related gold deposits associated with tungsten-tin provinces: Mineralium Deposita, v. 34, p. 323-334.

Tooth, B., Brugger, J., Ciobanu, C., and Liu, W., 2008, Modeling of gold scavenging by bismuth melts coexisting with hydrothermal fluids: Geology, v. 36, p. 815-818.

Wesolowski, D., Drummond, S. E., Mesmer, R. E., and Ohmoto, H., 1984, Hydrolysis equilibria of tungsten(VI) in aqueous sodium chloride solutions to 300°C: Inorganic Chemistry, v. 23(8), p. 1120-1132.

Wesolowski, D., and Ohmoto, H., 1986, Calculated oxygen isotope fractionation factors between water and the minerals scheelite and powellite: Economic Geology, v. 81, p. 471-477.

Wood, S.A., 1992, Experimental determination of the solubility of tungstate(s) and the thermodynamic properties of H_2WO_4(aq) in the range 300-600°C at 1 kbar: calculation of scheelite solubility: Geochim. Cosmochim. Acta, v. 56(5), p. 1827-1836.

Wood, S.A., and Samson, I.M., 2000, The hydrothermal geochemistry of tungsten in granitoids environments: I. Relative solubilities of ferberite and scheelite as a function of T, P, pH, and mNaCl: Economic Geology, v. 95, p. 143-182.

Wood, S.A., and Vlassopoulos, D., 1989, Experimental determination of the hydrothermal solubility and speciation of tungsten at 500°C and 1 kbar: Geochim. Cosmochim. Acta, v. 53, p. 303-312.

Yang, X.-M., 2012, Sulfur solubility in felsic magmas: implications for genesis of intrusion-related gold mineralization: Geoscience Canada, v. 39, p. 17-32.

Yuvan, J., 2006, Fluid inclusion and oxygen isotope studies of high-grade quartz-scheelite veins, CanTung mine, Northwest Territories, Canada: products of late-stage magmatic-hydrothermal event. M.Sc. Thesis, University of Missouri-Columbia, 60 p.

Zaw, K., and Singoyi, B., 2000, Formation of magnetite-scheelite skarn mineralization at Kara, Northwestern Tasmania: evidence from mineral chemistry and stable isotopes: Economic Geology, v. 95, p. 1215-1230.

FIGURE CAPTIONS

To the paper of S.G.Soloviev et al. "Geology, mineralization, stable isotope, and fluid inclusion characteristics of the Vostok-2 reduced W-Cu skarn and Au-W-Bi-As stockwork deposit, Sikhote-Alin, Russia"

FIG. 1. Regional tectonic setting of the Vostok-2 and other W and Au deposits of the Central Sikhote-Alin (Central Sikhote-Alin Gold-Tungsten Belt) (geology after Khanchuk et al., 1997; Khanchuk, 2000).

FIG. 2. Geological setting of the Vostok-2 deposit area in relation to the large granitoid intrusions (modified after Kudrin et al., 1979; Rub et al., 1982; Kovalenko et al., 1988; Belyansky et al., 2011; Soloviev and Krivoschekov, 2011).

FIG. 3. Surface geological plan (A) and cross-section (B) of the mineralized zones of the Vostok-2 deposit (compiled using the data of the Vostok-2 mine Geological Department).

FIG. 4. Plots illustrating the chemistry of igneous rocks from the Central stock, Dalnensky and Biserny plutons. (A) Classification SiO_2 vs. (K_2O+Na_2O) diagram for chemical compositions of igneous rocks (field boundaries are after Middlemost, 1997). (B) SiO_2 vs. K_2O diagram (field boundaries are after Le Maitre et al., 2002). (C) – Al/(Na+K) vs. Al/(Ca+Na+K) diagram defining the alkaline, meta-aluminous and peraluminous igneous rocks (field boundaries are after Maniar and Piccoli, 1989). (D) – Rb vs. (Y+Nb) diagram showing compositional fields of granitic rocks formed in syncollisional (syn-COLG), post-collisional (post-COLG), volcanic arc (VAG), within-plate (WPG), and oceanic ridge (ORG) tectonic environments (after Pearce, 1996). Numbers (1-20) of the compositions shown are the same as in Table 2. Other rock compositions (numbers 21-34) are from Gvozdev (2006, 2008), Rub et al. (1982), Kovalenko et al. (1988), Stepanov (1977), and Kudrin et al. (1979).

FIG. 5. Paragenesis of alteration assemblages showing sequence of mineralization at the Vostok-2 deposit in alternation with the intrusion phases.

FIG. 6. Photographs showing some typical features of hydrothermal alteration assemblages at the Vostok-2 deposit. A. prograde pyroxene (with minor garnet (G)) skarn (PS) replacing limestone (marble) lens (M) in biotite

hornfels (BH); B – prograde pyroxene (PS)-wollastonite (W) skarn veinlet in limestone (marble) (M); note the lack of garnet zone; C – quartz-pyroxene-amphibole retrograde skarn with scheelite (Sch); D-E – intrusive breccia in the Central stock: fragments of biotite hornfels (BH), prograde and retrograde (pyroxene and quartz-pyroxene-amphibole) skarns (PS, QPS) are cemented by granodiorite, and granodiorite is overprinted by amphibole-chlorite (hydrosilicate) assemblage; F-G – hydrosilicate alteration assemblage: F – massive pyrrhotite with quartz-amphibole aggregate, G – abundant scheelite with pyrrhotite and chalcopyrite; H-L – phyllic alteration: H – sheeted quartz (±sericite) veinlets in the Central stock granodiorite, I – quartz-arsenopyrite (±sericite) veinlets evolving into quartz breccia in the Central stock granodiorite, J – coarse-grained arsenopyrite in quartz (±sericite) veinlet (early association of the phyllic assemblage) (larger view of the previous sample, K – gradual replacement of hydrosilicate-altered pyroxene skarn (PS) and adjacent biotite hornfels (BH) by quartz-rich (±sericite) phyllic assemblage (QS), with “dilution” of the hydrosilicate stage sulfides, and quartz-scheelite-sulfide veinlets in the innermost part of the phyllic alteration zone, L – larger view of the quartz-scheelite-sulfide veinlets from the previous sample (the late association of the phyllic assemblage; yellow crystals – scheelite (Sch)).

FIG. 7. Photomicrographs of thin and polished sections showing relationships of minerals in hydrothermal alteration assemblages at the Vostok-2 deposit. A-E – thin sections (D-E – nicols crossed): A – retrograde skarn, with prograde skarn pyroxene corroded and partially replaced by retrograde skarn pyroxene (more euhedral), quartz, pyrrhotite, and scheelite; B – hydrosilicate alteration, with amphibole, quartz, sulfides (pyrrhotite, chalcopyrite), and scheelite; C – hydrosilicate alteration hydrosilicate alteration with chlorite-carbonate replacement of skarn, with scheelite and sulfides; D-E – phyllic alteration: D – quartz-sericite (muscovite) veinlet with quartz-scheelite central zone and sericite-carbonate-feldspar-quartz outer zone; E – phyllic alteration overprinting sulfide-rich hydrosilicate alteration assemblages, with development of apatite and scheelite; F-R – polished sections, phyllic alteration assemblages: F – euhedral scheelite and apatite intergrowing chalcopyrite and pyrrhotite; G - native bismuth grain and small native gold grain with chalcopyrite, pyrrhotite (small greyish-pink grains) and apatite; H - large native bismuth grain and small native gold grain with chalcopyrite and pyrrhotite (small greyish-pink grains); I - inclusion of pyrrhotite (greyish-pink) and native gold (bright yellow) in chalcopyrite; J - inclusion of native bismuth and native gold in scheelite; K - inclusion of pyrrhotite (greyish-pink), native gold (bright yellow) and laitakarite (Lt; light-grey) in chalcopyrite; L - chalcopyrite and native bismuth in a large scheelite grain; M - inclusion of joseite-B (Jo) and native bismuth in scheelite; N - inclusion of native bismuth, bismuthinite (Bmt), pyrrhotite and chalcopyrite in scheelite; O –

series of droplet-like grains of native bismuth in quartz (polished thin plate); P - chalcopyrite and native bismuth cementing corroded quartz and scheelite) and overgrown by euhedral arsenopyrire-2, with a native gold) grain in native bismuth remaining in arsenopyrite, and a chain of droplet-like grains of native bismuth; Q – native bismuth and chalcopyrite in galena; R – Sb-bursaite (Br) in sphalerite with pyrrhotite emulsion and crystalline grains; all in quartz. Abbreviations: Cpx – pyroxene, Amp – amphibole, Qz – quartz, Ap – apatite, Cal – calcite, Ccp – chalcopyrite, Chl – chlorite, Po – pyrrhotite, Sch – scheelite, Apy – arsenopyrite, Au – native gold, Bi – native bismuth, Gl – galena, Sph - sphalerite.

FIG. 8. Types of fluid inclusions in minerals from various hydrothermal alteration assemblages from the Vostok-2 deposit. A – primary type 1 multisolid fluid inclusion in pyroxene (hedenbergite) of retrograde quartz-pyroxene, B – larger view of the type 1 multisolid inclusion, C – cluster of the type 2A methane-bearing gaseous-liquid fluid inclusions in quartz of hydrosilicate assemblage, D – primary type 2A gaseous-liquid fluid inclusion and trail of pseudosecondary type 2B liquid-gaseous fluid inclusions in quartz of hydrosilicate stage, E – larger view of the type 2B fluid inclusion containing a small anisotropic solid phase, F and G – type 2A fluid inclusions in scheelite of hydrosilicate stage, H – type 3A and 3B fluid inclusions in quartz of the early association (quartz-arsenopyrite) of phyllic assemblage, I – larger view of the type 3B fluid inclusions frozen to -10^{o}C, with liquid and gaseous CO_2 phases; J - type 3A and 3B fluid inclusions forming cluster in the core of quartz crystal of the early (quartz-arsenopyrite) association of phyllic assemblage, K - type 3A and 3B fluid inclusions in scheelite of phyllic assemblage (numerous secondary type 4 inclusions are also present), L - a larger view of a small cluster of the type 3A and 3B inclusions, M – pseudosecondary (?) type 4 fluid inclusions in quartz of the late (quartz-sulfide) association of phyllic assemblage.

FIG. 9. Fluid inclusion data for the retrograde skarn, hydrosilicate and phyllic alteration assemblages of the Vostok-2 deposit. (A) Frequency histograms of final homogenization temperatures for various fluid inclusion types. (B) Plot of homogenization temperature of the carbonic phase (Th_{carb}) versus temperatures of final melting of the carbonic phase (Tm_{carb}) for H_2O-CO_2-(CH_4) fluid inclusions in minerals from the hydrosilicate (type 2A fluid inclusions) and phyllic (type 3A fluid inclusions) alteration assemblages. Contours of X_{CH4} and V_{car} are derived from figures in Thiery et al. (1994). (C) Minimum pressure estimates for the type 1 fluid inclusions in the retrograde skarn minerals, using the type 1 fluid inclusion homogenization temperatures (Table 7) and the temperatures estimated using the stable isotope

data for the host minerals (Table 9). The critical curves and isochors (corresponding to various salinities, wt.% NaCl) are from Roedder (1984).

FIG. 10. Stable isotope data for the retrograde skarn, hydrosilicate and phyllic alteration assemblages of the Vostok-2 deposit. (A) Frequency histograms of the oxygen stable isotope data, (B) Frequency histograms of the sulfur stable isotope data, (C) Frequency histograms of the carbon stable isotope data.

FIG. 11. Compositions of the igneous rock from the Central stock shown on the schematic plot of degree of fractionation (Rb/Sr ratio) versus the oxidation state (Fe_2O_3/FeO) for intrusive rocks associated with Cu-Au, W-Mo, Au-(Bi) and Sn mineralization (Thompson et al., 1999; Baker et al., 2005). Note the rock composition plot in the field of the reduced Au and W deposits. Numbers (1-20) of the compositions shown are the same as in Table 2.

FIG. 12. Log fO_2-pH-log fS_2 diagrams showing stability fields for Fe oxides and sulfides, carbonic and sulfur species, together with parts of the Fe-Ca-W-O-S and Ca-Mo-O-S systems (bold lines) showing stability fields for scheelite ($CaWO_4$), ferberite ($FeWO_4$), powellite ($CaMoO_4$), molybdenite (MoS_2) and molybdoscheelite ($Ca(W,Mo)O_4$), calculated for 500°C (A), 350°C (B) and 250°C (C) corresponding to retrograde skarn, hydrosilicate and phyllic alteration assemblages, respectively, at the Vostok-2 deposit. Dotted lines – values of fS_2. Andradite+quartz = hedenbergite+calcite equilibrium line (A), annite+orthoclase+quartz = ferroactinolite+ albite+calcite, chlorite-zoizite+calcite equilibrium lines (B), bornite+pyrite=chalcopyrite, native Bi = bismuthinite, arsenopyrite = pyrrhotite+loellingite, and orthoclase-muscovite equilibrium lines (C) are also shown. Diagrams calculated for ΣS=0.1 m, XCO_2=0.1 m, ΣCa=2.5 m, ΣFe=0.5 m, $\Sigma NaCl$=1 m, ΣW=0.0001 m, ΣMo=0.0001 m (A), ΣS=0.01 m, XCO_2=0.01 m, ΣCa=0.25 m, ΣFe=0.5 m, $\Sigma NaCl$=1 m, ΣW=0.0001 m, ΣMo=0.0001 m (B), ΣS=0.001 m, XCO_2=0.001 m, ΣCa=0.1 m, ΣFe=0.2 m, ΣK=0.1 m, $\Sigma NaCl$=1 m, ΣW=0.0001 m, ΣMo=0.0001 m (C). Thermodynamic data for the common species are from Johnson et al. (1992); data for W and Mo species – from Naumov et al. (1971), Drabek (1984), Kudrin (1986, 1989), Wesolowsky et al. (1984), Wood (1992), Wood and Samson (2000). Area and dominating forms of Au transport are also shown (Henley, 1984; Benning and Seward, 1996). Arrows indicate possible evolutional paths for the hydrothermal fluids at each stage. Abbreviations: Sch – scheelite, MoSch – molybdoscheelite, Bn – bornite, Py – pyrite, Ccp – chalcopyrite, Bi – native bismuth, Bmt – bismuthinite, Cal – calcite, Hd – hedenbergite, Ad – andradite, Qz – quartz.

FIG. 13. Estimated pressure and temperature conditions and evolutional paths for different fluid inclusion types (1-4) in hydrothermal assemblages at the Vostok-2 deposit, with composition of different fluid inclusion types as a function of depth and temperature (after Hedenquist et al., 1998; Fournier, 1999; Meinert et al., 2003; Baker and Lang, 2003). Vapor-pressure curves for H_2O-NaCl solutions at 0-70 wt.% NaCl-equiv. and the three-phase (L+V+H) curve are shown after Becker et al. (2008), Atkinson (2002). Curved lines labelled 1 and 2 represent the dry solidus of a quartz monzonite and solubility of a granite bearing 2 wt.% fluorine, respectively (Selby et al., 2000). The two-phase (L/L+V) curves (dotted lines) for H_2O-NaCl-CO_2 fluid containing 6 wt.% NaCl and 21.33 mol.% CO_2 (curve I), 10 mol.% CO_2 (curve II), and 4.08 mol.% CO_2 (curve III) (Schmidt and Bodnar, 2000) are shown. PT-fields for the major fluid inclusion types and possible evolutional paths for fluids (shaded arrows) are shown. Due to lack of pressure estimate for the type 2 and 4 inclusions, their fields are shown conditionally.

Soloviev et al. Fig. 1

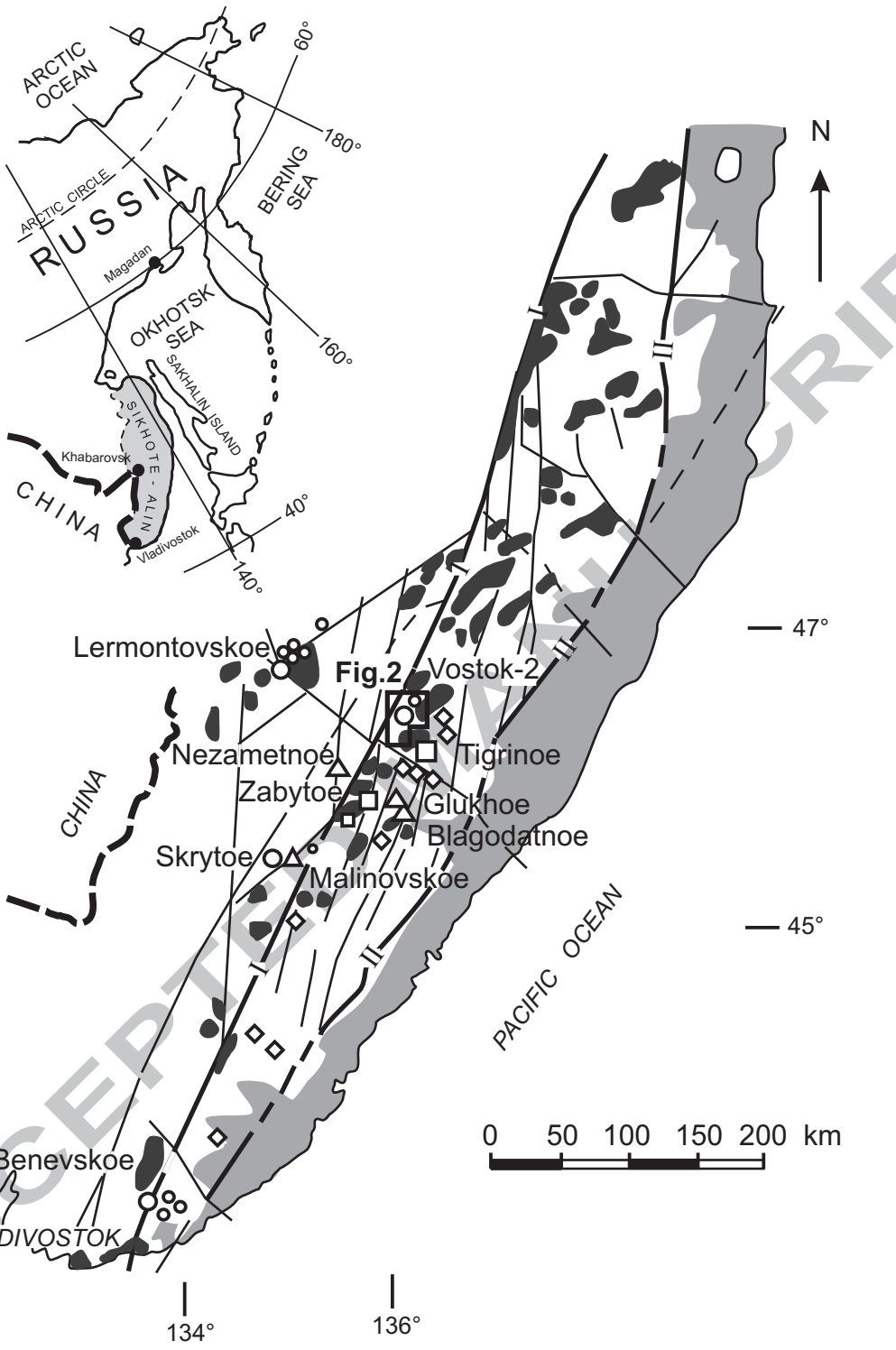

Paleozoic and Mesozoic accreted terrains

Eastern Sikhote-Alin Late Cretaceous-Paleogene volcanic belt

Early-Late Cretaceous granitic intrusions

Faults (I- Central Sikhote-Alin fault, II - Eastern Sikhote-Alin fault)

Tungsten deposits and occurrences

Tin-tungsten occurrences

Tungsten-tin-rare metal deposits and occurrences

Gold deposits and occurrences

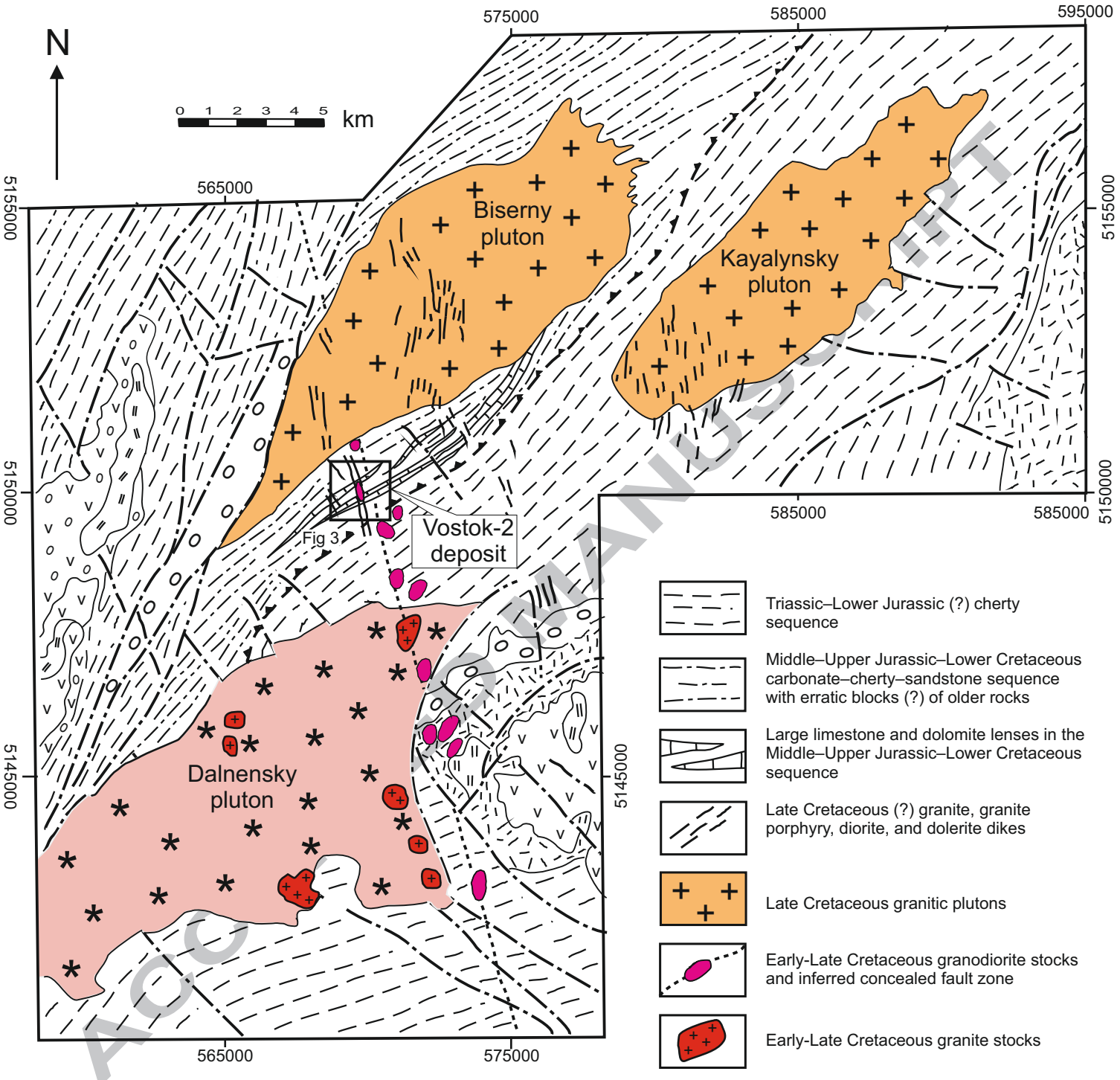

Cretaceous and Paleogene volcanic rocks of the EastStkhote-Alin Volcanic belt:

- Paleogene andesite, basatltic andesite, and basalt
- Upper Cretaceous andesite
- Upper Cretaceous andesitic tuff, lava breccia, and agglomerate
- Lower Cretaceous tuffstone, tuffite, and tuffaceous siltstone
- Lower Cretaceous tuffaceous conglomerate and gravelite
- Triassic–Lower Jurassic (?) cherty sequence
- Middle–Upper Jurassic–Lower Cretaceous carbonate–cherty–sandstone sequence with erratic blocks (?) of older rocks
- Large limestone and dolomite lenses in the Middle–Upper Jurassic–Lower Cretaceous sequence
- Late Cretaceous (?) granite, granite porphyry, diorite, and dolerite dikes
- Late Cretaceous granitic plutons
- Early-Late Cretaceous granodiorite stocks and inferred concealed fault zone
- Early-Late Cretaceous granite stocks
- Early Cretaceous Dalnensky monzonit-granodiorite-granite pluton
- Faults
- Zone of structural unconformity between Triassic–Lower Jurassic (?) and Middle–Upper Jurassic–Lower Cretaceous sequences (Khanchuk, 2000)

Soloviev et al. Fig. 3

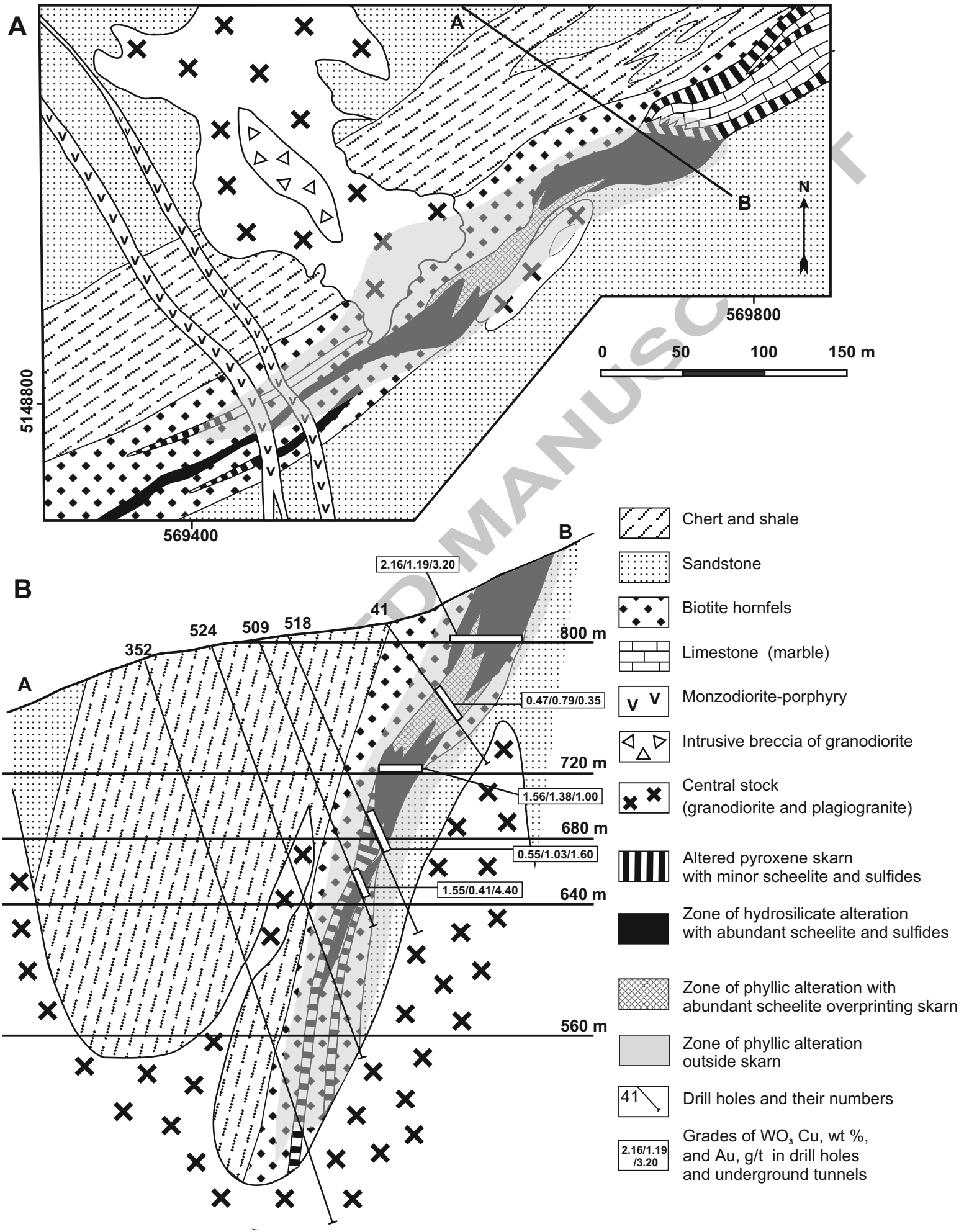

Soloviev et al Fig. 4

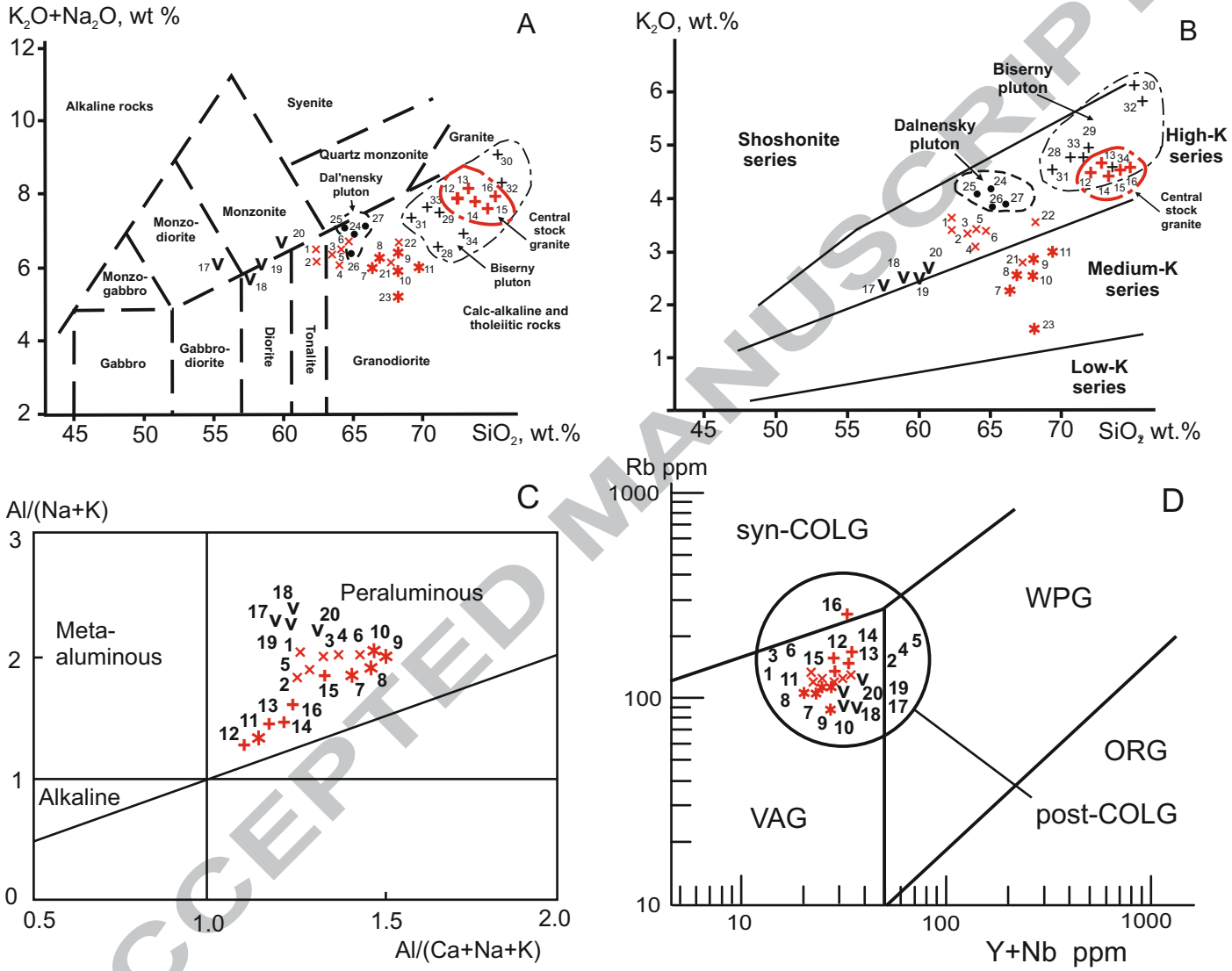

× Granodiorite (Central stock)

✱ "Plagiogranite" (Central stock)

\+ Granite (Central stock)

v Monzodiorite-porphyry

• Granodiorite (Dalnensky pluton)

\+ Granite (Biserny pluton)

Soloviev et al. Fig. 5

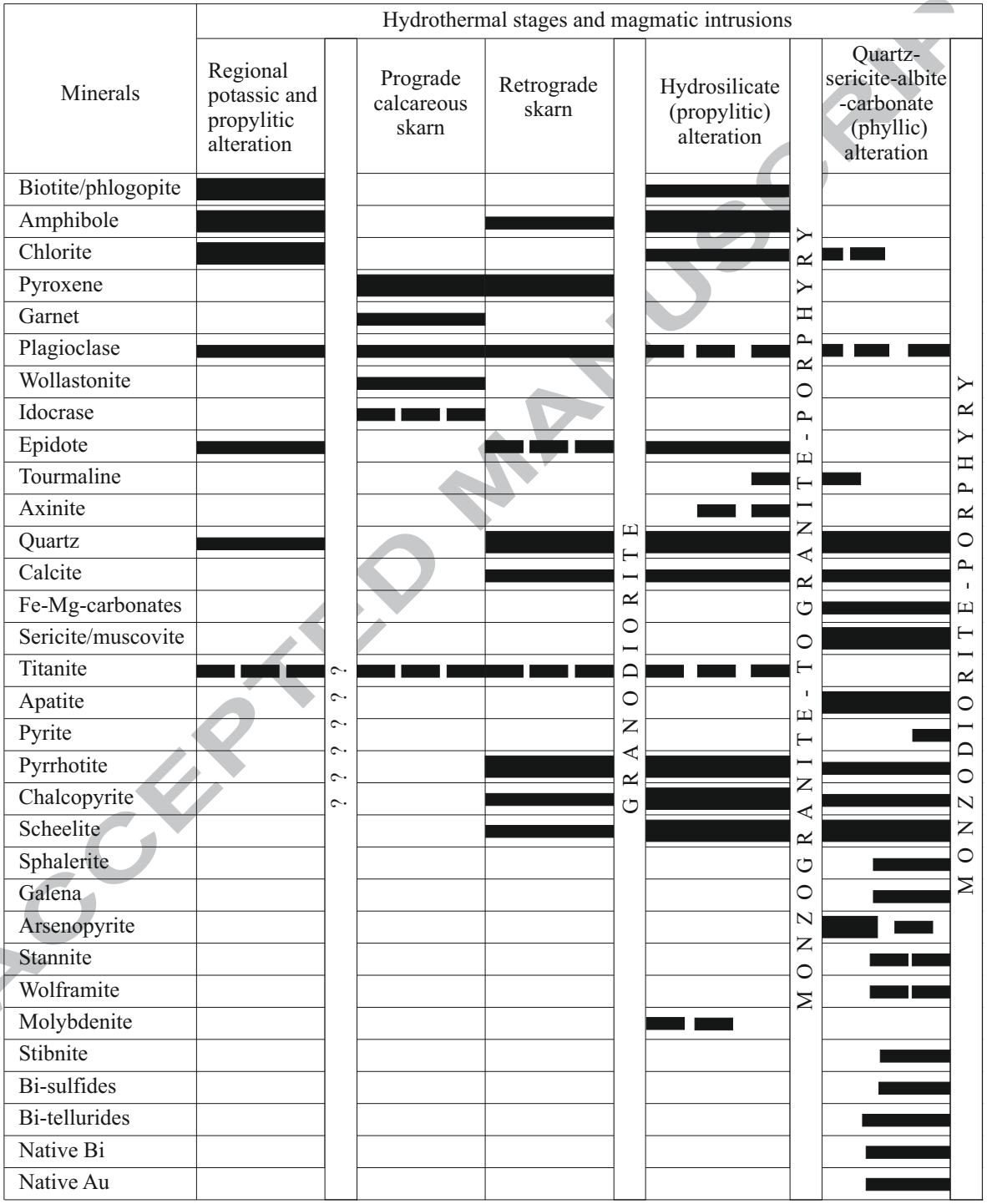

S.G.Soloviev et al. Figure 6

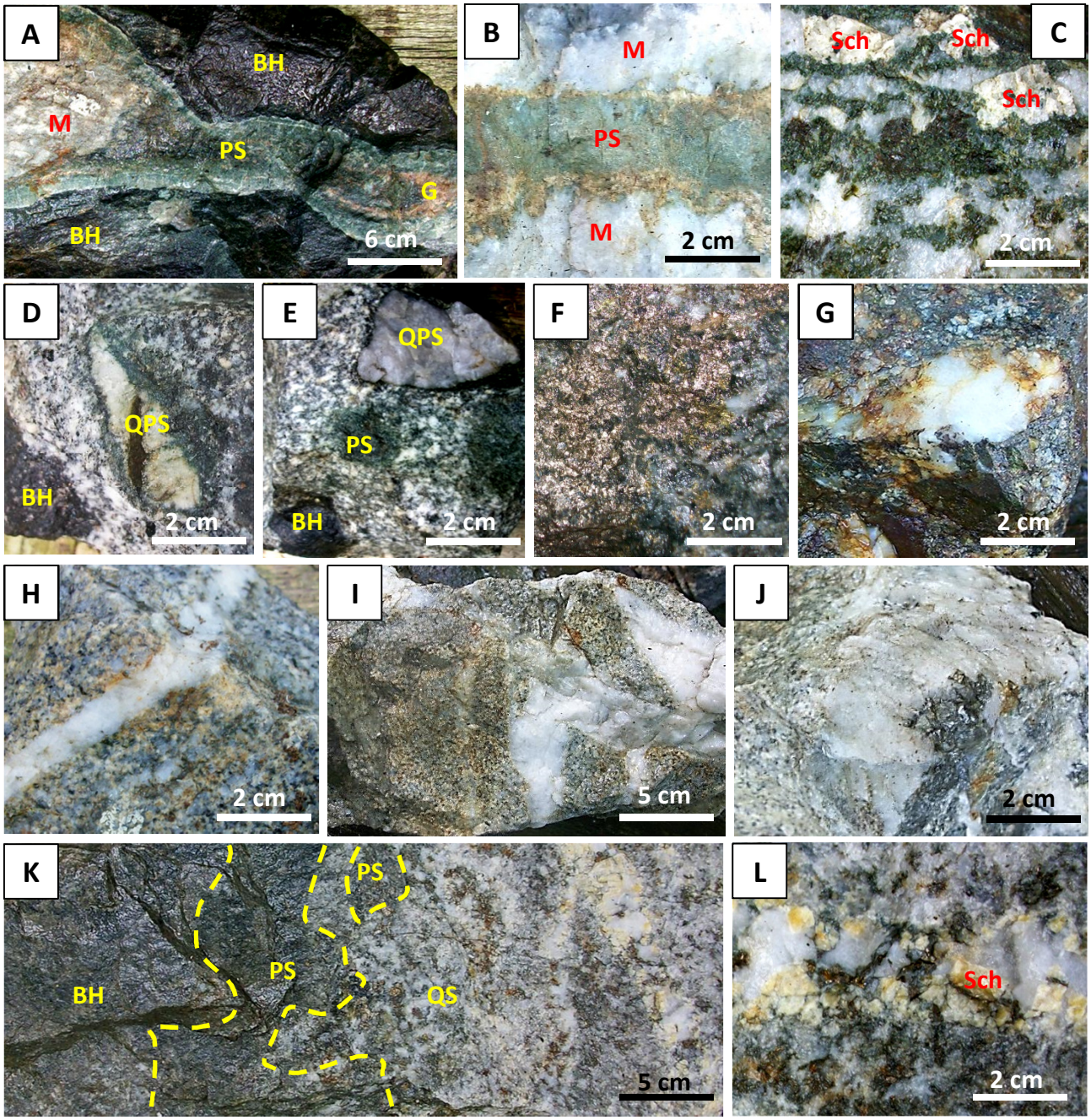

Soloviev et al. Fig. 7

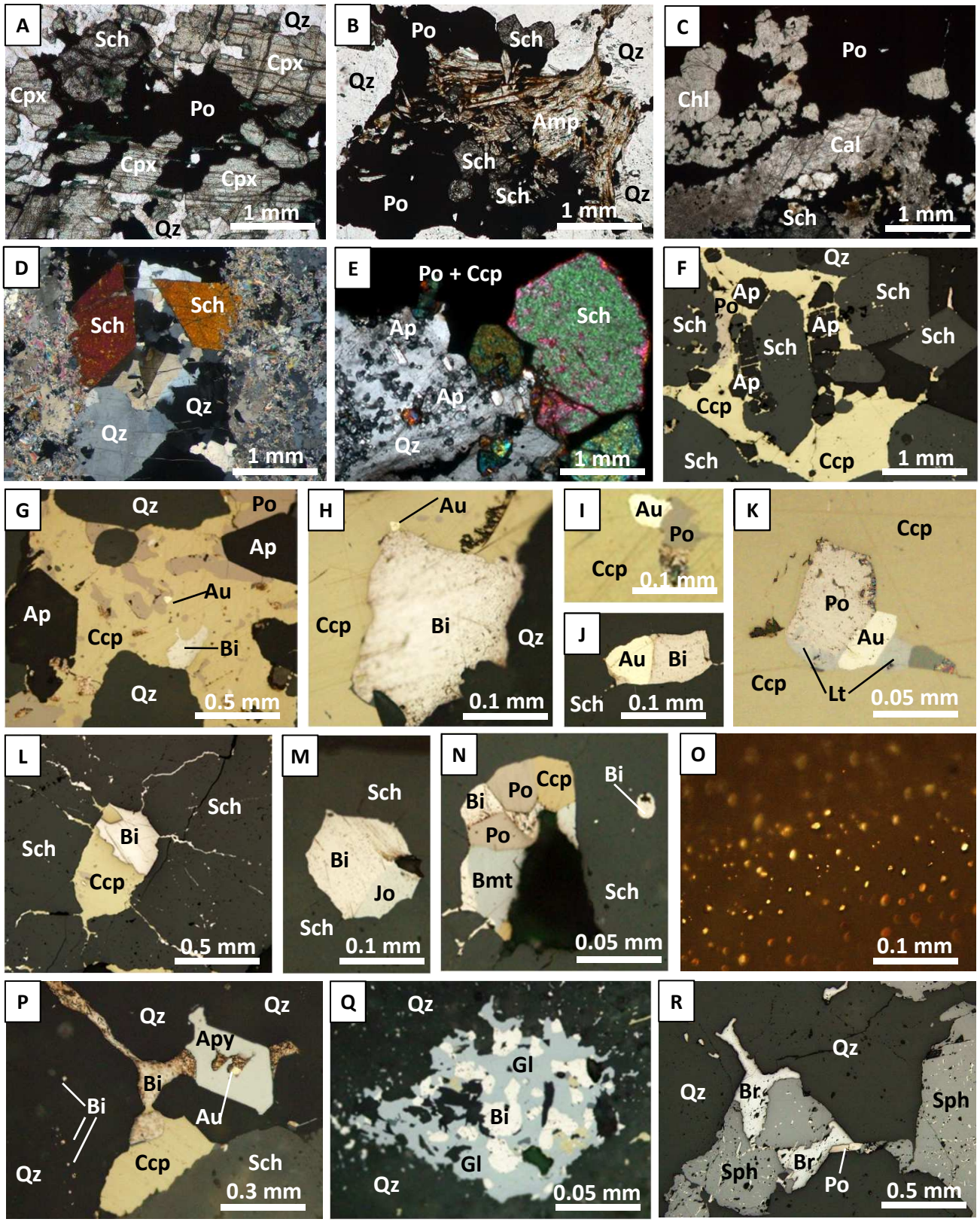

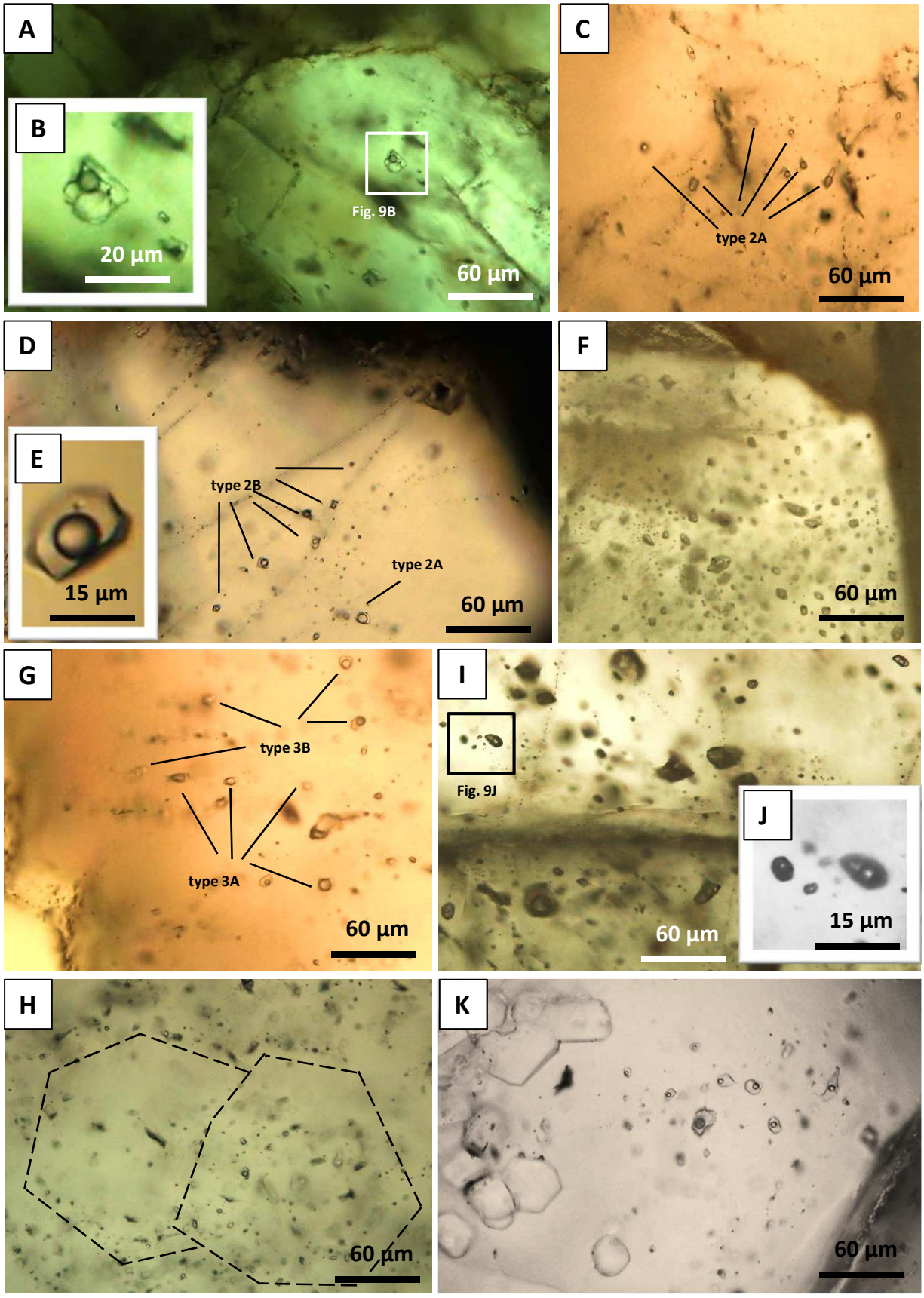

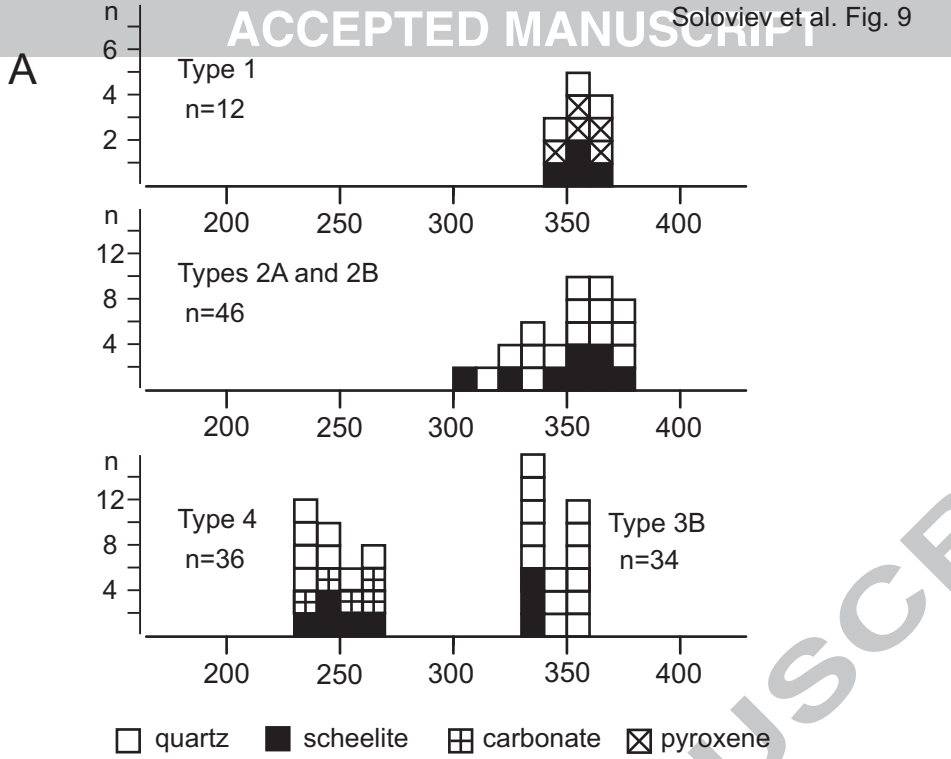

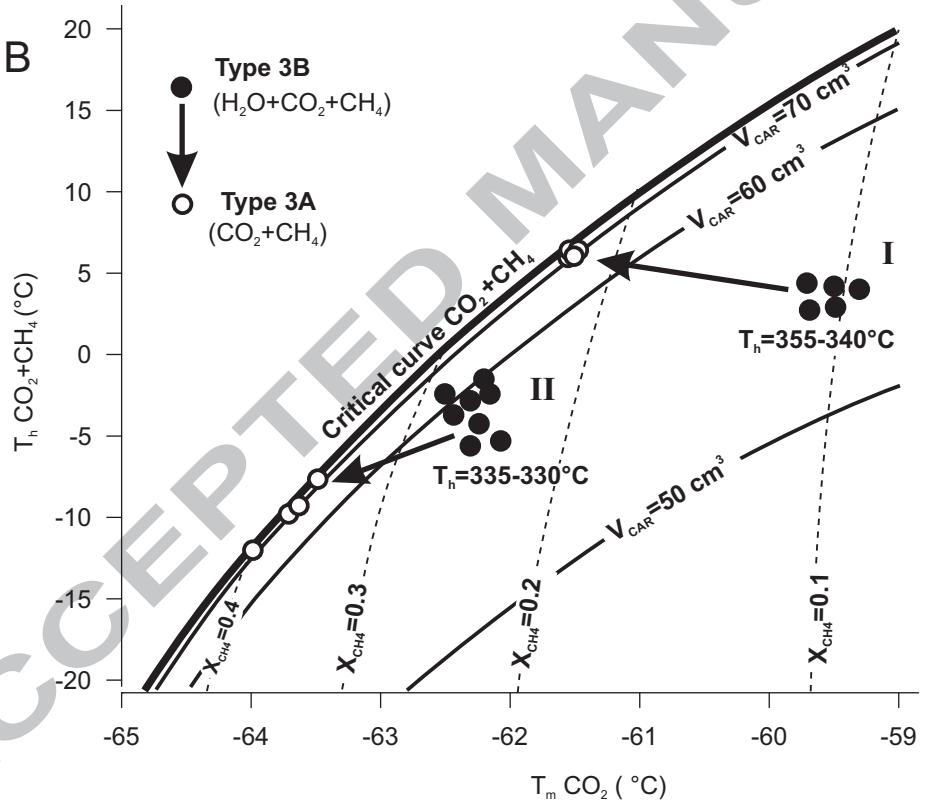

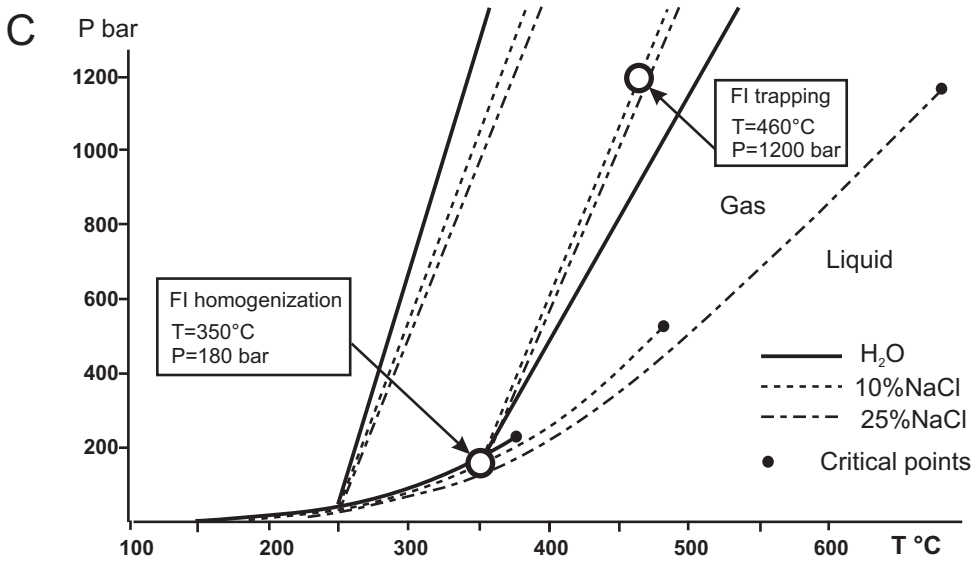

Soloviev et al. Fig.10

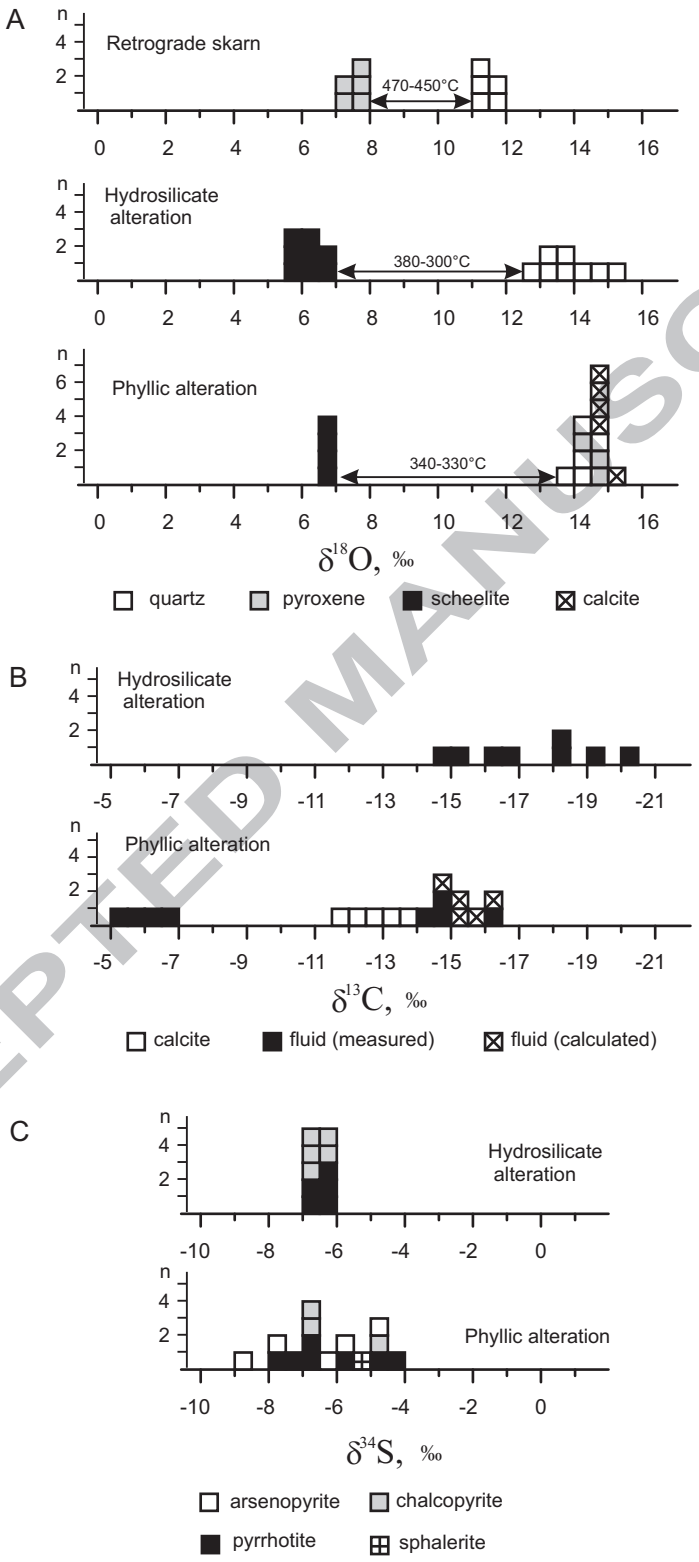

Soloviev et al. Fig. 11

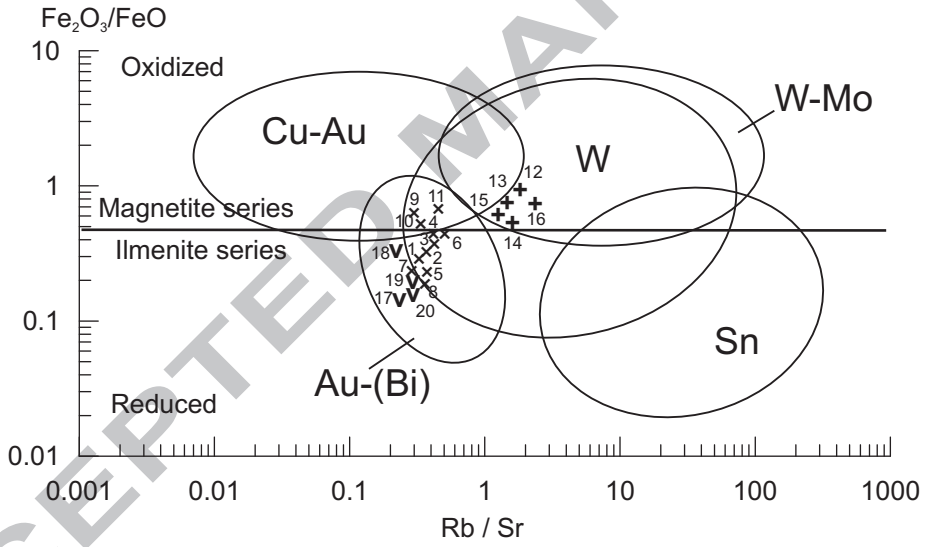

Soloviev et al. Fig. 12

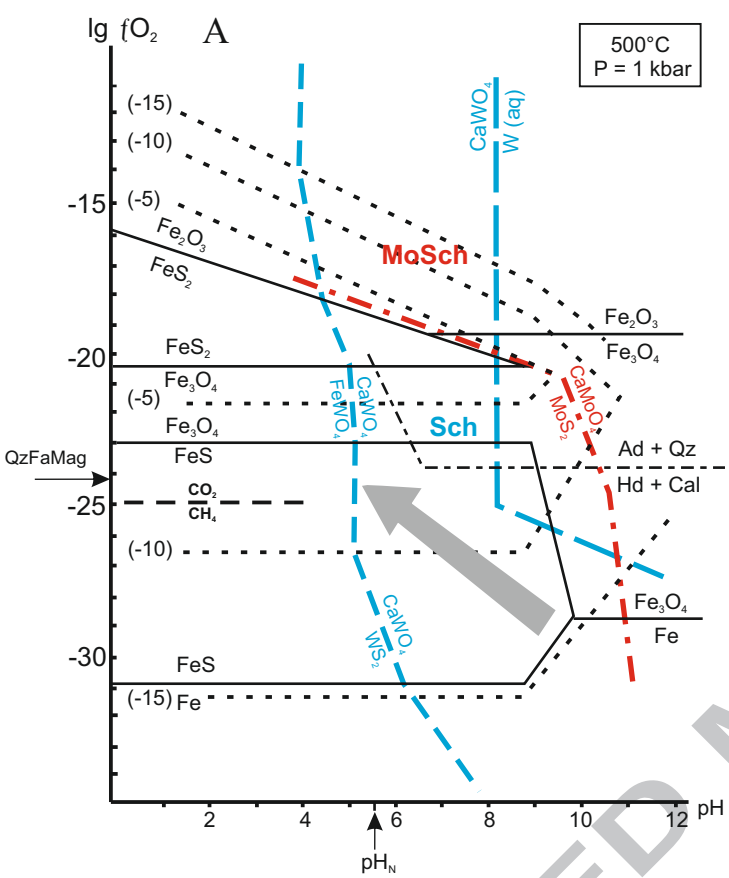

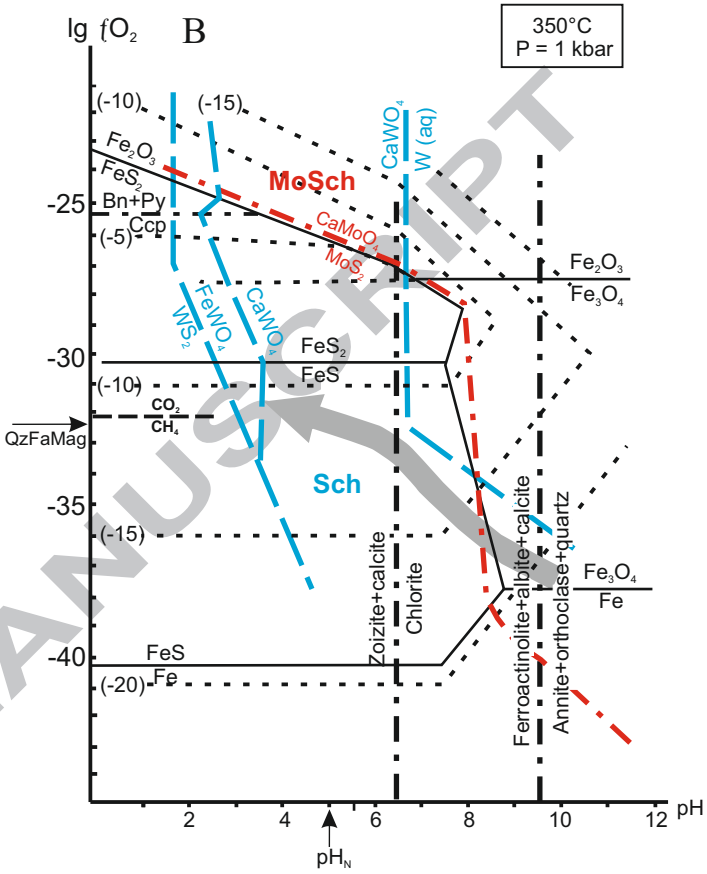

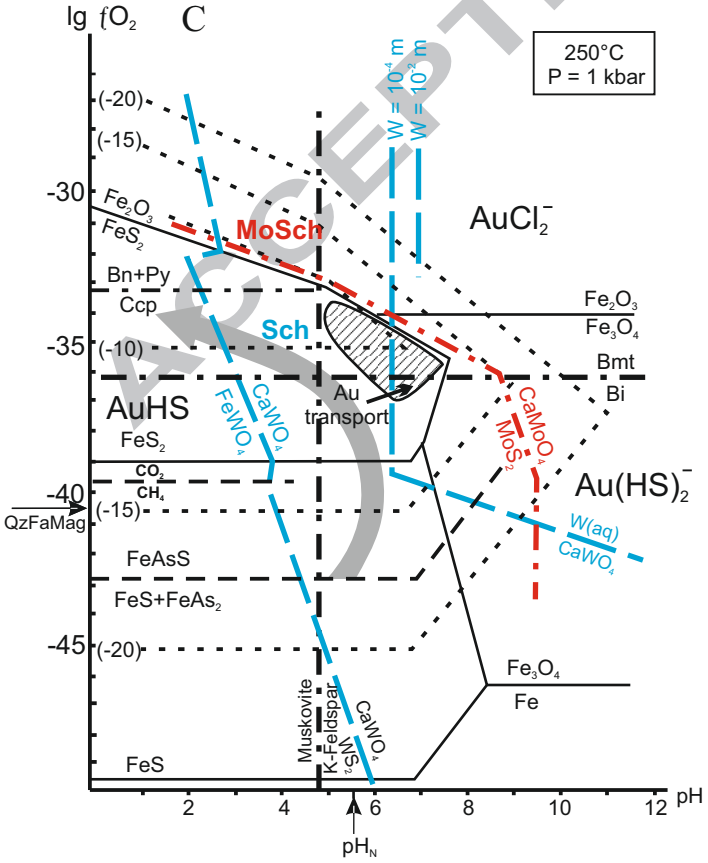

Soloviev et al. Fig. 13

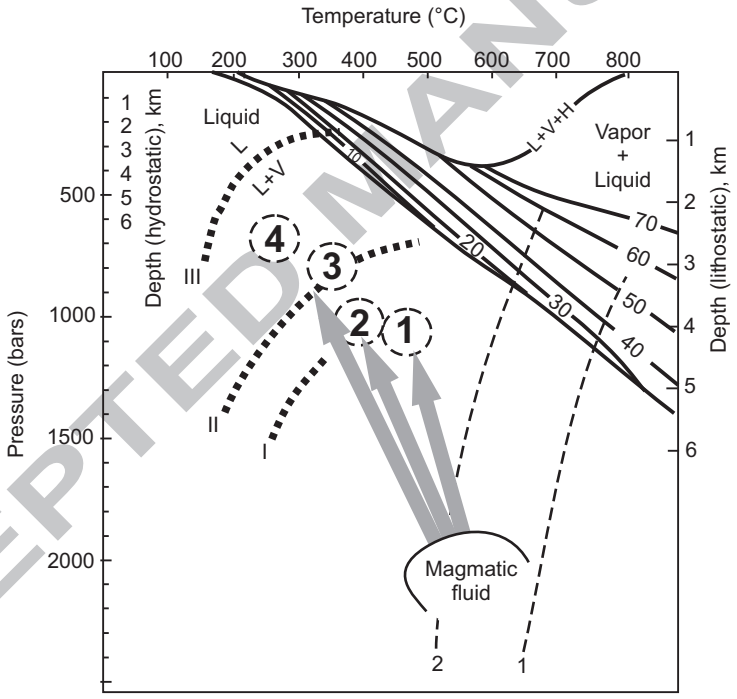

Table 1. Major Petrographic Features of Igneous Rocks from the Plutons in the Vostok-2 Deposit Area

Phase	Rocks	Petrography
		Dalnensky pluton
1	Quartz monzonite to granodiorite	Medium-grained equigranular pinkish-grey rock composed of rare clinopyroxene (<1%), brownish-green amphibole (5-10%), brown to reddish-brown biotite (8-10%), plagioclase (30-40%) – commonly andesine with 36-44% anorthite, locally zoned crystals from labradorite (50-58% anorthite) in the cores to andesine (50-44% anorthite) and oligoclase (36-20% anorthite) in the rims, K-feldspar (orthoclase) (20-30%), and quartz (15-20%). Accessory minerals – apatite, allanite, zircon, monazite, scheelite, titanite, garnet, magnetite, and ilmenite. Enclaves enriched in amphibole and biotite are locally present.
2	Monzogranite to granite	Coarse- to-medium-grained equigranular pinkish-grey rock composed of amphibole (1-2%), biotite (5-6%), plagioclase (30-35%) - commonly oligoclase with 28-30% anorthite, K-feldspar (35-40%), and quartz (25-30%). Accessory minerals – apatite, allanite, zircon, titanite, scheelite, garnet, ilmenite, and magnetite.
3	Granite to leucogranite	Fine-grained equigranular pinkish-grey rock composed of biotite (1-3%), plagioclase (15-20%) - commonly oligoclase with 16-18% anorthite and albite-oligoclase, K-feldspar (45-50%) and quartz (30-35%). Accessory minerals – apatite, allanite, zircon, scheelite, tourmaline, and ilmenite.
		Central stock
1	Granodiorite to “plagiogranite”	Medium-grained porphyry to equigranular grey rock composed of light-green amphibole (1-2%), reddish-brown biotite (10-15%), plagioclase (40-50%) including plagioclase phenocrysts (zoned from labradorite in the cores to andesine and oligoclase in the rims, locally with opposite/reverse zonation) and plagioclase in the groundmass (andesine with 36-38% anorthite to oligoclase with 26-28% anorthite), K-feldspar (orthoclase) (15-20%), and interstitial quartz (15-20%). Accessory minerals – apatite, allanite, zircon, rutile, titanite, garnet, and ilmenite. The “plagiogranite” contains more plagioclase (50-60%), which is less calcic (typically oligoclase), and more quartz (22-35%) but less K-feldspar (10-15%).
2	Monzogranite- to granite-porphyry	Medium- to fine-grained porphyry light-grey rocks composed of quartz, potassic feldspar (orthoclase) and plagioclase (andesine with 28-32% anorthite) phenocrysts (25-40%) and K-feldspar-quartz-plagioclase groundmass, with 45-50% K-feldspar, 30-35% quartz and 12-17% albite-oligoclase. Very minor biotite is present in the groundmass. Plagioclase phenocrysts commonly have zonation from andesine core to oligoclase rim. Accessory minerals – apatite, zircon, allanite, titanite, fluorite, ilmenite, and magnetite. Granite-porphyry contains more plagioclase in phenocrysts and groundmass (40-45%), will lesser K-feldspar25-35%) and quartz (15-20%) contents. Monzogranite-porphyry has a higher-calcic plagioclase in phenocrysts (38-44% anorthite) and groundmass (34-36% anorthite) and contains minor amphibole in both phenocrysts and groundmass.
		Biserny and Kayalinsky plutons
1	Monzogranite to granite	Coarse- to medium-grained equigranular to weakly porphyry pinkish-grey rock composed of biotite (4-6%), plagioclase (35-40%) – commonly oligoclase with 28-30% anorthite, K-feldspar (23-27%), and quartz (29-32%). Accessory minerals - apatite, allanite, zircon, titanite, scheelite, garnet, ilmenite, and magnetite.
		Late mafic dikes
1	Monzodiorite-porphyry	Dark greenish-gray fine-grained porphyry rock composed of plagioclase (andesine-labradorite) (35-45%), greenish- brown amphibole (35-40%), brown biotite (10-15%), K-feldspar (orthoclase) (1-7%), and quartz (1-5%). Plagioclase phenocrysts are long-prismatic, polysynthetic-twinned, and zoned from labradorite (50-58% anorthite) core to andesine rim; plagioclase in the groundmass is represented by andesine (42-50% anorthite). Accessory minerals – apatite, zircon, titanite, ilmenite, and magnetite.
2	Diorite-porphyry	Dark greenish-gray fine-grained rock composed of plagioclase (andesine-labradorite) (35-45%), augite (10-15%), and greenish-brown amphibole (40-55%), and minor K-feldspar (1-3 vol.%). Plagioclase phenocrysts are zoned from bitovnite core to labradorite-andesine rim; plagioclase in the groundmass is represented by andesine (45-50% anorthite). Accessory minerals – apatite, titanite, rutile, ilmenite, and magnetite.

Table 2. Representative Chemical Compositions of Igneous Rocks from the Central Stock (wt.%, ppm)

Sample numbers	1	2	3	4	5	6	7	8	9	10	11	12	13	14	15	16	17	18	19	20
Rocks	Granodiorite						"Plagiogranite"					Monzogranite- to granite-porphyry					Monzodiorite-porphyry (late dikes)			
wt percent																				
SiO_2	62.88	62.96	63.63	63.73	63.83	65.99	66.23	66.50	67.96	68.16	69.58	72.26	73.02	73.23	73.35	74.00	55.61	57.65	58.91	59.21
TiO_2	0.57	0.57	0.54	0.59	0.56	0.41	0.49	0.47	0.41	0.42	0.36	0.13	0.13	0.12	0.13	0.13	0.97	1.01	1.14	0.87
Al_2O_3	15.91	15.51	16.12	15.25	15.75	16.02	16.72	16.43	15.89	15.72	15.12	13.47	13.60	13.63	13.49	13.31	15.49	15.76	16.12	15.88
Fe_2O_3	0.90	1.13	1.19	1.35	0.93	1.11	0.54	0.60	1.09	0.98	1.16	1.58	1.05	0.60	0.79	0.90	2.12	1.94	2.21	1.98
FeO	3.76	3.76	3.24	3.30	3.63	2.40	2.59	3.04	2.07	2.14	1.81	1.10	0.82	1.18	1.17	1.10	4.34	4.61	4.25	4.31
MnO	0.10	0.09	0.09	0.09	0.09	0.06	0.06	0.06	0.05	0.08	0.04	0.04	0.04	0.04	0.04	0.04	0.12	0.14	0.15	0.12
MgO	2.41	2.40	2.45	2.54	2.55	2.04	1.88	1.55	1.42	1.60	1.54	0.29	0.58	0.32	0.42	0.49	4.68	3.59	3.46	3.35
CaO	4.71	4.72	4.01	4.03	3.80	3.43	3.27	3.33	3.05	2.40	2.42	1.38	1.26	1.31	1.15	1.26	5.87	5.23	4.62	4.42
Na_2O	2.80	2.87	2.87	2.87	2.80	3.14	3.67	3.62	3.42	3.34	3.14	3.48	3.48	3.48	3.10	3.19	3.77	3.23	3.79	3.21
K_2O	3.65	3.44	3.41	3.32	3.46	3.45	2.37	2.60	2.79	2.73	2.99	4.62	4.76	4.57	4.55	4.49	2.32	2.63	2.42	2.55
P_2O_5	0.18	0.16	0.19	0.22	0.19	0.13	0.13	0.13	0.12	0.09	0.11	<0.04	0.06	0.05	0.05	0.05	0.20	0.24	0.25	0.23
CO_2	<0.20	<0.20	0.75	<0.20	0.26	0.22	0.26	<0.20	<0.20	0.26	0.35	0.44	<0.20	0.40	0.51	<0.20	1.54	1.69	1.35	1.36
S tot.	<0.10	<0.10	<0.10	<0.10	<0.10	<0.10	<0.10	<0.10	<0.10	<0.10	<0.10	<0.10	<0.10	<0.10	<0.10	<0.10	0.14	0.21	0.16	0.22
F	0.092	0.10	0.11	0.088	0.10	0.12	0.11	0.060	0.11	0.11	0.097	0.13	0.099	0.12	0.13	0.12	0.10	0.11	0.14	0.20
H_2O-	1.61	1.50	1.40	1.84	1.35	1.03	1.02	0.88	0.99	0.81	0.67	0.55	<0.10	0.43	0.63	0.39	1.56	1.71	1.41	1.32
H_2O+	0.20	0.18	0.21	0.28	0.20	0.20	0.25	0.21	0.16	0.10	0.28	0.21	0.65	0.18	0.15	0.36	0.26	0.46	0.41	0.53
Total	100.08	99.71	100.41	99.80	99.60	99.85	99.69	99.78	99.83	99.04	99.77	99.82	99.95	99.76	99.76	100.26	99.09	100.222	100.79	99.76
ppm																				
Ba	455	438	429	455	482	563	821	848	750	813	563	366	376	348	330	339	515	525	514	484
Sr	379	357	322	361	367	368	428	400	390	411	347	109	112	99	97	96	454	447	456	463
Co	6.7	7.8	7.6	8.1	10	6.7	8.0	8.4	7.9	6.9	7.7	3.1	2.4	2.4	2.4	2.3	19	17	26	22
Ni	20	<20	28	24	21	61	56	40	43	28	33	26	<20	23	21	<20	23	29	32	24
V	91	75	57	82	93	31	28	39	32	33	28	8.8	10	9.2	9.6	9.9	190	200	180	140
Li	33	38	35	31	38	43	35	34	35	39	38	31	29	33	26	42	34	34	36	34
Rb	118	118	118	127	127	127	109	109	91	118	118	155	155	164	136	255	91	101	96	101
Be	2.9	2.6	2.2	3.3	4.6	3.9	4.6	4.6	4.6	4.0	3.5	3.5	3.5	3.5	4.1	3.4	3.0	2.2	3.0	2.6
Zr	158	143	162	163	142	131	147	154	134	134	127	116	112	117	113	108	178	164	174	184
Nb	11	11	10	11	13	9	14	13	13	13	11	14	14	15	14	15	14	12	14	10
$\Sigma REE_2O_3+Y_2O_3$	140	150	150	150	140	150	140	140	120	140	130	160	160	160	180	170	160	140	200	140
Y	15	20	15	20	20	15	10	8	15	15	15	15	20	20	15	20	18	18	26	22
B	10	15	15	30	20	10	<10	20	20	10	10	30	10	10	<10	10	14	16	12	24
Sn	<5	<5	<5	6.1	7.1	<5	<5	5.5	7.7	6.6	6.8	<5	<5	<5	<5	<5	<5	<5	<5	<5
Mo	1.8	1.1	3.0	3.0	4.3	5.3	2.8	1.0	1.9	1.5	4.0	1.8	2.6	1.9	1.0	1.5	1.2	2.2	2.2	1.4
W	1.0	1.3	3.2	3.1	3.5	20.2	12.2	9.8	3.4	3.9	4.8	11.0	8.2	6.6	12.0	9.0	3.2	1.4	2.5	4.6
Cu	10	20	30	30	20	20	15	40	30	20	30	20	15	15	15	20	40	30	80	70
Zn	80	80	100	80	80	80	60	60	60	60	60	60	60	40	40	60	120	130	160	150
Pb	20	20	10	20	20	20	12	10	15	10	20	20	20	30	20	20	20	40	40	30
Kd	10.38	13.73	13.55	14.92	14.69	14.76	17.58	16.71	16.90	18.90	19.31	20.41	25.94	26.44	26.17	26.26	5.97	8.42	9.73	10.21

Kd – differentiation coefficient (index) (Larson index = $1/3SiO_2 + K_2O - (FeO+CaO+MgO)$).

Table 3. Rare and Rare Earth Element Contents in Selected Samples of the Igneous Rocks from the Central Stock (ppm)

Sample numbers	3	6	10	11	13
Rocks	Granodiorite		"Plagiogranite"		Monzogranite- to granite-porphyry
Sc	7.0	6.4	7.7	6.2	7.5
Ta	0.75	0.91	0.87	0.96	1.00
La	26.2	28.5	33.1	22.5	22.8
Ce	59.0	66.1	72.4	46.8	54.9
Nd	20.1	24.0	25.9	17.3	23.2
Sm	3.76	4.23	4.37	3.59	5.14
Eu	0.85	0.89	0.90	0.83	0.49
Tb	0.49	0.55	0.56	0.44	0.88
Yb	1.35	1.37	1.34	1.40	2.61
Lu	0.18	0.16	0.15	0.20	0.38
$(La/Yb)_N$	13	14	17	11	6

The sample numbers are the same to those in Table 2.

Table 4. Representative Microprobe Analyses of Pyroxene and Garnet from Prograde and Retrograde Skarns at the Vostok-2 Deposit, wt.%, mol.%

	1	2	3	4	5	6	7	8	9	10	11	12	13
SiO_2, wt.%	51.16	51.35	51.07	51.23	52.43	53.12	53,62	52.12	36.91	36.74	36.79	37.01	37.54
TiO_2, wt.%	0.32	0.26	0.40	0.12	0.12	0.10	0.10	0.12	0.32	0.26	0.12	0.12	0.13
Al_2O_3, wt.%	0.59	0.47	0.26	0.49	0.04	0.21	0.14	0.15	12.32	15.49	13.42	17.45	19.82
FeO, wt.%	20.56	21.23	21.32	21.37	22,64	22.45	22.59	23.12	15.47	12.32	13.71	12.55	13.62
MnO, wt.%	0.59	0.57	0.68	0.62	1.82	2.52	2.98	1.49	0.40	0.43	0.39	3.81	3.64
MgO, wt.%	5.67	5.22	4.68	4.03	0.86	0.50	0.45	0.60	0.23	0.33	0.35	0.28	0.20
CaO, wt.%	21.22	21.19	21.53	21.65	21.24	21.12	20.84	22.38	33.22	32.56	33.12	28.12	24.64
Total, wt.%	100.11	100.29	99.94	99.51	99.15	99.02	100.72	99.98	98.87	98.13	97.90	99.34	99.59
	Di 33	Di 32	Di 28	Di 25	Di 6	Di 4	Di 4	Di 4	Alm 2	Alm 3	Alm 2	Alm 9	Alm 21
	Hd 65	Hd 67	Hd 70	Hd 72	Hd 87	Hd 86	Hd 85	Hd 90	Adr 44	Adr 31	Adr 39	Adr 21	Adr 9
	Jo 2	Jo 2	Jo 2	Jo 2	Jo 7	Jo 10	Jo 11	Jo 6	Grs 52	Grs 63	Grs 57	Grs 60	Grs 61
									Prp 1	Prp 1	Prp 1	Prp 1	Prp 1
									Sps 1	Sps1	Sps 1	Sps 9	Sps 8

Hd=hedenbergite, Di=diopside, Jo=johannsenite, Alm=almandine, Adr=andradite, Grs=grossular, Prp=pyrope, Sps=spessartine

1-8 – pyroxene (1-4 – from prograde calcic skarn, 5-8 – from retrograde skarn), 9-13 – garnet (9-11 – from prograde calcic skarn, 12-13 – from retrograde skarn).

Table 5. Representative Microprobe Analyses of Amphibole, Biotite and Chlorite from Various Alteration Assemblages at the Vostok-2 Deposit, wt.%, mol.%

	1	2	3	4	5	6	7	8	9	10	11	12	13
SiO_2, wt.%	51.23	52.12	51.48	55.55	51.45	53.82	38.41	38.71	26.49	25.10	25.42	29.62	30.57
TiO_2, wt.%	0.41	0.38	0.43	0.20	0.36	0.56	1.28	1.93	0.02	0.04	0.00	0.00	0.04
Al_2O_3, wt.%	3.67	2.17	3.54	2.47	3.92	2.67	15.48	15.40	20.45	19.15	20.58	20.12	17.42
FeO, wt.%	19.32	20.67	19.69	13.11	15.95	3.48	15.49	17.53	19.86	23.24	27.17	13.40	13.21
MnO, wt.%	0.61	0.55	0.46	0.72	1.13	1.54	0.42	0.61	0.83	0.65	1.42	1.20	1.10
MgO, wt.%	9.14	8.91	8.41	13.13	11.55	22.11	14.23	13.21	19.83	19.40	13.65	21.04	24.03
CaO, wt.%	12.41	12.11	12.56	12.21	12.49	12.43	0.00	0.02	0.00	0.04	0.00	0.08	0.00
Na_2O, wt.%	0.32	0.42	0.21	0.34	0.42	0.43	0.18	0.14	0.02	0.00	0.04	0.00	0.00
K_2O, wt.%	0.43	0.25	0.26	0.21	0.27	0.31	9.38	9.21	0.00	0.00	0.12	0.00	0.00
H_2O, wt.%	2.01	2.01	2.02	2.09	2.04	2.17	4.08	4.13	11.66	11.40	11.27	12.49	12.04
Total, wt.%	99.55	99.59	99.06	100.03	99.58	99.52	98.95	100.89	99.16	99.02	99.67	98.20	99.36

1-6 – amphibole (1-3 – ferroactinolite from retrograde skarn, 4-5 – actinolite from hydrosilicate assemblage, 6 – tremolite from hydrosilicate assemblage), 7-8 – biotite (7 – biotite from zones of pervasive "biotititzation", 8 – biotite from hydrosilicate assemblages), 9-13 – chlorite (9-11 – ripidolite from hydrosilicate assemblages, 12-13 - picnochlorite from phyllic assemblages).

Table 6. Chemical compositions of some gold and bismuth minerals from the Vostok-2 deposit

Mineral	Au	Ag	Bi	Cu	Sb	Pb	Se	Te	S	Total	Empirical formula
Native Au	74.75	22.92	0.12	1.54	0.00	0.00	0.00	0.16	0.14	99.63	
Electrum	63.12	36.88	0.08	0.11	0.00	0.00	0.01	0.18	0.03	100.41	
Electrum	51.30	45.93	0.09	2.00	0.00	0.04	0.00	0.07	0.11	99.54	
Electrum	57.23	41.50	0.00	0.50	0.06	0.00	0.03	0.12	0.08	99.52	
Native Bi	0.04	0.13	99.01	0.19	0.10	0.00	0.03	0.00	0.00	99.50	
Native Bi	0.09	0.08	99.34	0.00	0.03	0.00	0.00	0.00	0.00	99.54	
Native Bi	0.00	0.00	99.52	0.42	0.19	0.00	0.03	0.00	0.03	100.19	
Bismuthinite	0.00	0.00	80.78	0.14	0.12	0.43	0.41	0.01	18.21	100.10	$Bi_{2.01}(S_{2.96}Se_{0.03})_{2.99}$
Bismuthinite	0.01	0.00	81.51	0.03	0.00	0.08	0.00	0.00	18.51	100.14	$Bi_{2.02}S_{2.98}$
Joseite-B	0.18	0.08	73.56	0.08	0.25	0.17	1.37	21.80	2.77	100.26	$(Bi_{3.91}Sb_{0.02}Pb_{0.01})_{3.94}Te_{1.90}(S_{0.96}Se_{0.20})_{1.16}$
Joseite-B	0.21	0.12	73.59	0.01	0.18	0.18	1.58	21.39	2.67	99.93	$(Bi_{3.94}Sb_{0.02}Pb_{0.01})_{3.97}Te_{1.88}(S_{0.93}Se_{0.22})_{1.15}$
Joseite-B	0.04	0.04	76.05	0.02	0.18	0.24	2.37	19.34	1.83	100.11	$(Bi_{4.21}Sb_{0.02}Pb_{0.01})_{4.24}Te_{1.75}(S_{0.66}Se_{0.35})_{1.01}$
Hedleyite	0.00	0.10	80.46	0.05	0.21	0.07	0.48	18.31	0.02	99.70	$(Bi_{7.18}Sb_{0.03})_{7.21}(Te_{2.68}Se_{0.11})_{2.79}$
Hedleyite	0.04	0.00	80.64	0.07	0.25	0.00	0.77	18.18	0.03	99.98	$(Bi_{7.14}Sb_{0.04})_{7.18}(Te_{2.64}Se_{0.18})_{2.82}$
Hedleyite	0.00	0.07	80.65	0.11	0.26	0.00	0.68	18.26	0.00	100.03	$(Bi_{7.15}Sb_{0.04})_{7.19}(Te_{2.65}Se_{0.16})_{2.81}$
Hedleyite	0.01	0.06	80.72	0.00	0.21	0.00	0.70	18.36	0.01	100.07	$(Bi_{7.15}Sb_{0.03})_{7.18}(Te_{2.66}Se_{0.16})_{2.82}$
Laitakarite	0.07	0.14	72.17	2.68	0.08	2.87	17.48	1.33	3.08	99.90	$(Bi_{3.31}Sb_{0.02}Cu_{0.40}Pb_{0.13})_{3.86}(Se_{2.12}S_{0.92}Te_{0.10})_{3.14}$
Sb-bursaite	0.00	0.46	22.43	0.88	9.83	50.24	0.07	0.07	16.32	100.30	$(Pb_{5,08}Cu_{0.29})_{5.37}(Bi_{2,25}Sb_{1,69})_{3.94}(S_{10,66}Se_{0.02}Te_{0.01})_{10.69}$
Sb-bursaite	0.00	0.47	22.68	0.93	9.61	49.93	0.08	0.14	16.41	100.25	$(Pb_{5,04}Cu_{0.31})_{5.35}(Bi_{2.27}Sb_{1,65})_{3.92}(S_{10,70}Se_{0.02}Te_{0.01})_{10.73}$
Sb-bursaite	0.04	0.59	23.14	0.92	9.65	49.31	0.08	0.06	16.02	99.81	$(Pb_{5,04}Cu_{0.31})_{5.35}(Bi_{2,35}Sb_{1,68})_{4.03}(S_{10,59}Se_{0.02}Te_{0.01})_{10.62}$

Table 7. Types of Fluid Inclusions (FI) in Minerals from Various Hydrothermal Assemblages of the Vostok-2 Deposit

Mineral (number of FI studied)	FI type	FI size	FI content	T_m eu., °C	T_m carb, °C	T_m ice, °C	T_h carb, °C	T_m clathrate, °C	Homogenization, T_h, °C	Estimated salinity, wt.% NaCl-equiv.	Estimated CO_2/CH_4 ratio***	Estimated pressure (T_h correction)
Retrograde skarn												
Quartz, pyroxene, scheelite (12)	1	5-25 µm	up to 4 solids, gas 10-20 vol.%			-3.7- -3.3			Gas to liquid: 360-340	5.4-6.0*		1.1.-1.2 kbar**** (~110°C)
Hydrosilicate (propylitic) alteration assemblage												
Quartz, scheelite (28)	2A	5-25 µm	gas ~ 40-50 vol.%	-29.5±0.5		-4.5- -3.5		+10.5-+16.5	Gas to liquid: 380-350	7.2-5.7	$CH_4>>CO_2$	
Quartz, scheelite (18)	2B	5-25 µm	gas ~ 25-40 vol.%	-31.5±0.5		-10.9- -6.3			Gas to liquid: 350-300	14.9-9.6*		
Phyllic alteration assemblages												
Early (quartz-arsenopyrite) assemblage												
Quartz (12)	3A	5-40 µm	gas >95 vol.%		-61.5		+5.9 - +6.1				3.5	0.9 kbar *****
Quartz (18)	3B	5-40 µm	gas ~ 40-60 vol.%		-59.7 - -59.3		+2.7 - +4.4	+9.0 - +11.7	Gas to liquid: 355-340	>1.5**	9.0	
Intermediate (quartz-scheelite±arsenopyrite) assemblage												
Quartz, scheelite (7)	3A	5-40 µm	gas >95 vol.%		-64.0 - -63.5		-12.0 - -7.6				1.5-2	0.9 kbar *****
Quartz, scheelite (16)	3B	5-40 µm	gas ~ 40-60 vol.%		-62.7 - -62.2		-3.3 - -1.5	+9.2 - +9.5	Gas to liquid: 335-330	>1.5**	2.5-3	
Late (quartz-scheelite-sulfide-Au-Bi) assemblage												
Quartz, carbonate, scheelite (36)	4	5-40 µm	gas ~ 15-30 vol.%	-24.5±1.0		-4.1- -8.3			Gas to liquid: 265-230	6.6-12.0*		

T_m eu. – eutectic temperature (first ice melting temperature), °C; T_m carb – final CO_2 melting temperature, °C; T_m ice - final ice melting temperature, °C; T_m clathrate - final clathrate melting temperature, °C; T_h carb – carbonic phase homogenization temperature, °C.

* Salinity estimated by final ice melting temperature (Bodnar and Vityk, 1995).

**Salinity estimated by clathrate melting temperature (Darling, 1991).

***The ratio estimated by final CO_2 melting temperature and carbonic phase homogenization temperature (Thiery et al., 1994).

****The trapping pressure estimated by combined fluid inclusion and isotopic method (see text) using the charts in Potter, 1977 and Roedder, 1984.

******The trapping pressure estimated by using the T_h of the high density type 3B inclusions (T_h correction is not required) and density of the low-density type 3A inclusions, determined by final CO_2 melting temperature and carbonic phase homogenization temperature (Thiery et al., 1994), and overall estimation using computation programs of Baker, 2003; T_h correction is not required.

Table 8. Combined Gas and Leachate Analyses of Fluid Inclusions in Quartz and Scheelite from the Vostok-2 Deposit (as Determined by Bulk Gas Chromatography and ICP-MS Analysis of Leachate)

Mineral assemblages	Retrograde skarn	Hydrosilicate alteration				Hydrosilicate alteration with phyllic overprint				Phyllic alteration						
										Quartz-arsenopyrite			Quartz-scheelite± arsenopyrite		Quartz-scheelite-sulfide-Au-Bi	
Minerals	quartz				scheelite	quartz			scheelite	quartz						
Samples	1	2	3	4	5	6	7	8	9	10	11	12	13	14	15	16
	V-4	V-16	V-9	V-18	V-18W	V-21	V-20	V-25	V-1W	V-19	V-7	V-2	V-10	V-11	V-8	V-17
H_2O, ppm	241.0	797.1	733.1	679.7	1473.2	477.5	639.4	1146.5	778.8	573.2	588.0	739.6	1401.8	618.0	611.5	1027.8
Major components, grams per kilogram H_2O																
CO_2	19.20	13.72	6.88	22.55	8.58	190.38	64.66	9.95	35.53	194.67	137.38	81.42	42.03	67.47	49.20	110.61
CH_4	0.11	5.40	3.03	8.09	7.51	6.36	9.14	2.13	5.69	6.19	5.12	2.12	7.49	18.32	2.95	5.58
Cl	10.21	2.73	<0.51	2.37	1.54	<0.79	<0.59	<0.33	3.16	<0.66	<0.64	1.15	<0.27	4.29	<0.61	4.23
SO_4	17.27	13.53	5.16	4.59	3.85	<1.98	<1.48	<0.82	6.92	<1.65	<1.60	<1.27	<0.67	<1.53	<1.54	2.85
HCO_3	21.19	35.07	3.39	29.08	30.50	28.28	33.55	15.28	4.12	21.74	43.29	29.83	31.20	46.01	18.06	27.46
B	5.05	1.69	2.92	0.49	0.14	0.36	0.22	0.18	0.33	0.47	0.58	0.95	0.20	0.64	0.78	0.38
F	<1.57	<0.47	<0.51	<0.56	<0.18	<0.79	<0.59	<0.33	<0.49	<0.66	<0.64	<0.51	<0.27	<0.61	<0.61	<0.37
Na	10.31	8.40	3.18	8.28	2.96	9.57	6.28	4.95	4.93	6.67	13.14	9.28	9.86	19.49	6.01	13.41
K	5.50	0.64	0.70	1.07	0.41	0.83	1.05	0.28	1.08	1.52	0.91	0.63	0.38	0.52	0.39	0.73
Ca	6.81	1.99	0.00	0.82	9.26	0.00	4.49	0.19	0.00	0.17	0.54	0.89	0.76	0.00	0.00	0.13
Mg	0.83	5.44	0.08	2.54	0.27	0.32	0.31	0.22	0.72	0.23	1.05	0.70	0.42	0.19	0.30	0.27
Fe	0.00	2.55	0.00	0.11	0.60	0.00	0.08	0.02	0.46	0.01	0.04	0.00	0.02	0.00	0.00	0.00
Mole fractions (major cations and anions), mol.%																
Na	0.56	0.55	0.87	0.70	0.34	0.92	0.64	0.91	0.79	0.85	0.88	0.86	0.90	0.98	0.92	0.95
K	0.18	0.02	0.11	0.05	0.03	0.05	0.06	0.03	0.10	0.11	0.04	0.03	0.02	0.02	0.04	0.03
Ca	0.21	0.08	0.00	0.04	0.61	0.00	0.26	0.02	0.00	0.01	0.02	0.05	0.04	0.00	0.00	0.01
Mg	0.04	0.34	0.02	0.21	0.03	0.03	0.03	0.04	0.11	0.03	0.07	0.06	0.04	0.01	0.04	9.02
Cl	0.36	0.10	0.12	0.11	0.08	0.05	0.03	0.04	0.39	0.05	0.03	0.06	0.01	0.14	0.06	0.20
SO_4	0.22	0.18	0.43	0.08	0.07	0.00	0.00	0.00	0.31	0.00	0.00	0.00	0.00	0.00	0.00	0.05
HCO_3	0.42	0.72	0.45	0.81	0.85	0.95	0.97	0.96	0.29	0.95	0.96	0.94	0.99	0.86	0.94	0.75
Mole ratios																
CO_2/CH_4	61.8	0.9	0.8	1.0	0.4	10.9	2.6	1.7	2.3	11.4	9.7	14.0	2.0	1.3	6.1	7.2
Na/K	3.2	22.3	7.7	13.1	12.3	19.5	10.1	29.9	7.7	7.4	24.4	25.1	44.1	63.1	26.3	31.1
Na+K/Ca+Mg	2.9	1.4	44.5	3.1	0.6	33.2	2.4	15.8	8.1	24.1	10.4	8.2	12.0	108.1	21.9	41.9
SO_4+HCO_3/Cl	1.8	9.2	7.2	7.8	12.3	21.4	33.4	27.5	1.5	19.8	39.5	15.3	67.2	6.3	17.7	4.0

Table 9. Oxygen and carbon isotope data for minerals and fluid species at the Vostok-2 deposit

Samples	Minerals studied	Measured values						Calculated values						T_{hom}, °C
		$\delta^{18}O_{mineral}$, ‰				$\delta^{13}C_{mineral}$, ‰	$\delta^{13}C_{fluid}$, ‰*	T_{calc}, °C		$\delta^{18}O_{H2O}$, ‰		$\delta^{13}C_{CO2}$, ‰	$\delta^{13}C_{fluid}$, ‰**	
		quartz	scheelite	pyroxene	calcite	calcite		quartz-scheelite	quartz-pyroxene	quartz*	quartz** calcite**			
Retrograde skarn														
V-4	Quartz, pyroxene	11.3		7.5			-		470	8.6				340-360
V-30	Quartz, pyroxene	11.4		7.5			-		460	8.5				
V-31	Quartz, pyroxene	11.5		7.6			-		460	8.6				
V-36	Quartz, pyroxene	11.7		7.8			-		460	8.8				
V-43	Quartz, pyroxene	11.6		7.6			-		450	8.5				
Hydrosilicate alteration														
V-9	Quartz, scheelite	13.0	5.9				-16.7	382		8.5	8.1±0.4			350-380
V-12	Quartz, scheelite	13.3	6.0				-20.1	368		8.5	8.4±0.4			
V-13	Quartz, scheelite	13.5	6.0				-18.4	355		8.3	8.6±0.4			
V-14	Quartz, scheelite	13.7	6.1				-14.9	349		8.4	8.8±0.4			
V-16	Quartz, scheelite	13.7	6.1				-15.5	349		8.4	7.6±0.8			300-350
V-18	Quartz, scheelite	14.5	6.5				-19.2	326		8.5	8.4±0.8			
V-34	Quartz, scheelite	15.0	6.7				-18.3	310		8.5	8.9±0.8			
V-35	Quartz, scheelite	15.4	7.0				-16.5	305		8.7	9.3±0.8			
Phyllic alteration														
Early assemblage (quartz-arsenopyrite)														
V-2	Quartz	14.1					-6.0				8.7±0.2			340-355
V-5	Quartz	14.0					-5.2				8.6±0.2			
V-7	Quartz	14.5					-6.9				9.1±0.2			
V-19	Quartz	14.6					-6.1				9.2±0.2			
Intermediate assemblage (quartz-scheelite±arsenopyrite)														
V-10	Quartz, scheelite	14.5	6.6				-15.0	331		8.7	8.8±0.2			330-335
V-11	Quartz, scheelite	14.5	6.7				-14.5	337		8.8	8.8±0.2			
V-54	Quartz, scheelite	14.8	6.8				-16.4	326		8.8	9.1±0.2			
V-55	Quartz, scheelite	14.9	7.0				-14.9	331		9.1	9.2±0.2			
Late assemblage (quartz-scheelite-sulfide-Au-Bi)														
V-8	Calcite				14.7	-12.8					7.3±0.7	-11.6±0.3	-15.5±0.7	230-265
V-15	Calcite				15.0	-12.5					7.6±0.7	-11.3±0.3	-15.2±0.7	
V-17	Calcite				14.6	-13.2					7.2±0.7	-12.0±0.3	-15.9±0.7	
V-20	Calcite				15.5	-12.0					8.1±0.7	-10.8±0.3	-14.7±0.7	
V-23	Calcite				14.9	-13.6					7.5±0.7	-12.4±0.3	-16.3±0.7	

T_{calc}, °C – calculated using the oxygen isotope distribution in the respective pairs of minerals (quartz-pyroxene, quartz-scheelite) (Faure, 1986; Wesolowski and Ohmoto, 1986),
$\delta^{13}C_{CO2}$, ‰ – calculated using T_{hom} and the carbon isotope distribution in the calcite-CO_2 system (Ohmoto, Rye, 1979),
*$\delta^{13}C_{fluid}$, ‰ = $\delta^{13}C_{CO2+CH4}$, ‰ – measured in extracted bulk fluid inclusion fluids in quartz and scheelite,
**$\delta^{13}C_{fluid}$, ‰ = $\delta^{13}C_{CO2+CH4}$, ‰ - calculated using the gas chromatography data for average ratio of CO_2/CH_4 = 6.5 (see Table 9), T_{hom}, $\delta^{13}C_{CO2}$, and the carbon isotope distribution in the CO_2-CH_4 system (Ohmoto, Rye, 1979),
$\delta^{18}O_{H2O}$, ‰, quartz* – calculated using T_{calc} and the oxygen isotope distribution in the quartz-H_2O system (Faure, 1986),
$\delta^{18}O_{H2O}$, ‰, quartz**, calcite** – calculated using T_{hom} and the oxygen isotope distribution in the quartz-H_2O and calcite-H_2O systems (Faure, 1986),

T_{hom}, ^{o}C – fluid inclusion homogenization temperatures in the respective fluid inclusion assemblages (see Table 8).

Table 10. Sulfur isotope compositions of sulfides from the Vostok-2 deposit

Samples	Description	Po	Po*	Ccp	Apy	Sph
		$\delta^{34}S$, ‰				
Hydrosilicate alteration						
V-1	Quartz and amphibole, minor pyrrhotite and chalcopyrite, trace scheelite			-6.6		
V-9	Quartz and amphibole, abundant pyrrhotite and chalcopyrite, minor scheelite	-6.6		-6.4		
V-11	Quartz and amphibole, abundant scheelite, minor pyrrhotite and chalcopyrite			-6.6		
V-12	Quartz and amphibole, abundant pyrrhotite, subordinated chalcopyrite and scheelite	-6.3		-6.2		
V-13	Quartz and amphibole, abundant pyrrhotite, subordinated chalcopyrite and scheelite	-6.5				
V-14	Quartz and amphibole, abundant pyrrhotite, minor chalcopyrite and scheelite	-6.4		-6.6		
V-18	Quartz and amphibole, abundant scheelite, minor pyrrhotite, chalcopyrite	-6.9				
Phyllic alteration						
Early assemblage (quartz-arsenopyrite)						
V-7	Quartz-sericite vein with minor coarse-grained arsenopyrite				-4.9	
V-19	Quartz-sericite vein with minor coarse-grained arsenopyrite				-6.0	
V-22	Quartz-sericite vein with abundant fine-grained arsenopyrite				-9.0	
V-5	Quartz-sericite vein with minor coarse-grained arsenopyrite and pyrite				-7.6	
Intermediate assemblage (quartz-scheelite±arsenopyrite)						
V-10	Quartz-sericite vein with arsenopyrite and scheelite				-6.5	
Late assemblage (quartz-scheelite-sulfide-Au-Bi)						
V-20	Quartz-sericite vein with abundant sulfides (chalcopyrite, pyrrhotite) and scheelite	-6.9	-4.5	-6.9		
V-6	Quartz-sericite vein with abundant pyrrhotite, subordinated chalcopyrite and scheelite	-5.6		-4.6		
V-23	Quartz-sericite vein with abundant sulfides (chalcopyrite, pyrrhotite) and minor scheelite		-6.8	-7.0		
V-15	Quartz-sericite vein with minor pyrrhotite and scheelite	-7.7				
V-8	Quartz-sericite vein with minor sulfides (chalcopyrite, pyrrhotite, sphalerite) and scheelite	-4.1				-5.4
V-17	Quartz-sericite vein with minor sulfides (chalcopyrite, pyrrhotite) and scheelite	-7.2				

Abbreviations: Po – monoclinal pyrrhotite, Po* – hexagonal pyrrhotite (non-magnetic); Ccp – chalcopyrite, Apy – arsenopyrite, Sph – sphalerite.

Highlights

The deposit incorporates reduced-type W skarn and Au mineralization related to ilmenite-series intrusion
Several stages of scheelite and sulfide±Au deposition distinguished paralleling magmatic differentiation
Cyclic releases of carbonic low-salinity to aqueous moderate-salinity fluids from cooling magma
The early carbonic fluids were dominated by CH_4, the late carbonic fluids – by CO_2
Complex magmatic (crustal to mantle-derived) and sedimentary sourcing of fluid species

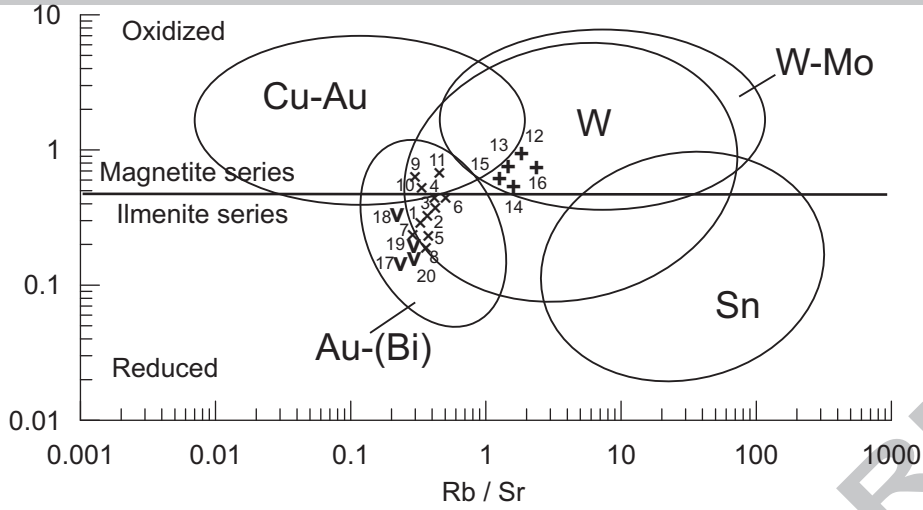
Fe2O3/FeO
10
1
0.1
0.01
Oxidized
Reduced
Magnetite series
Ilmenite series
Cu-Au
W
W-Mo
Sn
Au-(Bi)
0.001
0.01
0.1
1
10
100
1000
Rb / Sr

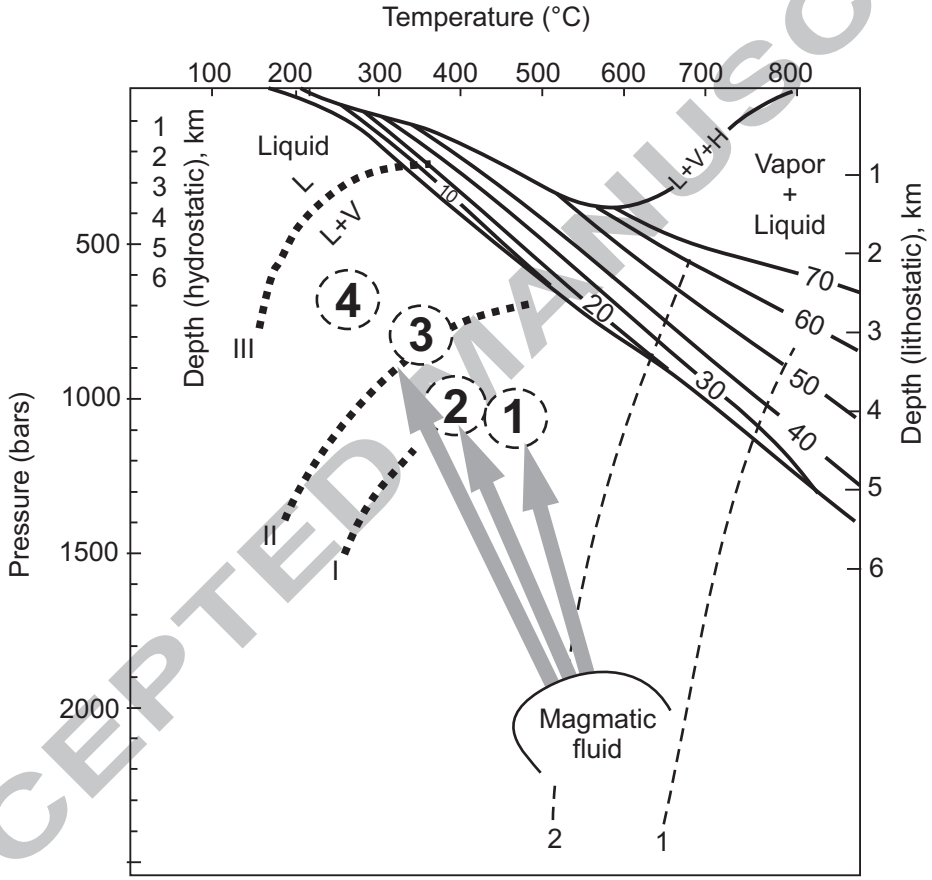
Temperature (°C)
100
200
300
400
500
600
700
800
Liquid
L
L+V
Vapor
+
Liquid
L+V+H
10
20
30
40
50
60
70
I
II
III
1
2
3
4
Magmatic
fluid
Depth (hydrostatic), km
Depth (lithostatic), km
Pressure (bars)
500
1000
1500
2000